universität
wien

DISSERTATION

Titel der Dissertation

"A Spin-Flip Cavity for Microwave Spectroscopy of Antihydrogen"

Verfasserin

Mag. rer. nat. Silke Federmann

angestrebter akademischer Grad

Doktorin der Naturwissenschaften (Dr. rer. nat.)

Wien, 2012

Abstract

The present thesis is a contribution to the ASACUSA (Atomic Spectroscopy And Collisions Using Slow Antiprotons) experiment. The aim of this experiment is to measure the ground-state hyperfine structure of antihydrogen. This is done using a Rabi-like spectrometer line consisting of an antihydrogen source, a microwave cavity, a sextupole magnet and a detector. The cavity induces spin-flip transitions in the ground-state hyperfine levels of antihydrogen whereas the sextupole magnet selects the antihydrogen atoms according to their spin state. Such a configuration allows the measurements of the hyperfine transition in antihydrogen with very high precision. A comparison with the corresponding transitions in hydrogen would thus provide a very sensitive test of the charge-parity-time (CPT) symmetry.

In the context of this thesis, the central piece of this spectrometer line, the spin flip cavity, was designed and implemented. The delicacy of this task was achieving the required field homogeneity: It needs to be better than 90% over a volume of $\approx 1000\,\mathrm{cm}^3$ (wavelength $21\,\mathrm{cm}$) to yield reasonable experimental resolution.

Furthermore, to avoid uncontrolled spin-flip transitions (Majorana spin-flips), a static magnetic field superimposed to the microwave field is necessary. This static field has to fulfill similar requirements on field homogeneity as the microwave field. A suitable static field including an efficient shielding solution was implemented in the context of this thesis as well.

The overall outline of the work is as follows: After a general introduction setting the global context of this thesis, the corresponding theoretical background is presented. Subsequently, the experimental setup is discussed including a more detailed overview of the single components of the spectrometer line. In the following, special emphasis is put on the design studies and the mechanical implementation of the spin-flip cavity as well as on the implementation of the static magnetic field including an efficient shielding. The thesis is concluded with a short summary and an outlook on future upgrades of the current setup.

Zusammenfassung

Die vorliegende Arbeit ist ein Beitrag zum ASACUSA (Atomic Spectroscopy And Collisions Using Slow Antiprotons) Experiment mit dem Ziel der Messung der Hyperfeinstruktur von Antiwasserstoff mittels eines Rabi Aufbaus. Dieser Aufbau besteht aus einer Antiwasserstoffquelle, einem Hohlraumresonator, einem Sextupol Magneten sowie einem Detektor. Der Hohlraumresonator hat die Funktion die einzelnen hyperfeinen Übergänge des Antiwasserstoffs im Grundzustand anzuregen, während der Sextupol Magnet dazu dient, die Antiwasserstoffatome entsprechend ihres Spins zu selektieren.

Solch ein Aufbau ermöglicht eine hochpräzise Messung der Hyperfein-Übergangsfrequenzen im Antiwasserstoffatom. Ein Vergleich dieser mit den entsprechenden Übergängen in Wasserstoff bietet die Möglichkeit, die CPT (charge-parity-time) Symmetrie mit sehr hoher Genauigkeit zu überprüfen.

Im Rahmen dieser Arbeit wurde das Herzstück dieses Aufbaus, der Hohlraumresonator entworfen und gebaut. Die Schwierigkeit des Designs eines geeigneten Resonators lag in den extremen Anforderungen an die Feldhomogenität: Um eine genügend große Auflösung der Übergangsfrequenz sicherzustellen, muss das oszilierende Feld im Inneren des Resonators über die gesamte Strahlapertur (ca. $1000\,cm^3$, Wellenlänge $21\,cm$) eine Feldhomogenität von über 90% aufweisen. Außerdem ist es erforderlich, dem Mikrowellenfeld ein statisches Magnetfeld zu überlagern, um unkontrollierte Übergänge (sog. Majorana spin-flips) zwischen den Hyperfeinniveaus zu vermeiden. Ebenso wie das oszillierende Feld unterliegt das statische Feld strikten Anforderungen an die Feldhomogenität.

Der Entwurf sowie die praktische Umsetzung eines statischen Feldes, das den obgenannten Bedingungen genügt, wurde ebenfalls im Rahmen dieser Arbeit durchgeführt. Des weiteren wurde eine effiziente magnetische Abschirmung zur Dämpfung externer Streufelder untersucht und implementiert. Zusammen mit einer allgemeinen Einleitung, den entsprechenden theoretischen Grundlagen und einer Beschreibung der Komponenten des Rabi Aufbaus, werden diese Ergebnisse im Kontext der vorliegenden Arbeit präsentiert.

Contents

Chapter 1

Introduction

Mankind's thirst for knowledge has led to many different fields of research and science. However, the most prominent urge common to several of these fields is the search for an answer to the fundamental questions 'Who are we?', 'Where do we come from?' and 'Where are we going?'. These questions have been accompanying men and women ever since the ability to reason has developed. The present thesis is dedicated to contribute to the investigation of one of them — the question of our origin.

According to our present understanding the universe as we know it started with a large burst of energy — the Big Bang. Within this approach however, matter and antimatter should have been produced in equal shares. Since both types do not agree very well with each other (or, depending on the view, agree too well) they would have annihilated immediately thus freeing again a huge amount of energy. Most of the matter and antimatter particles did exactly this and trace evidence of their destructive encounter is still measurable today: It is the cosmic microwave background radiation which was discovered in 1964 [1].

Nevertheless, matter has apparently won the battle leading to a universe full of it with so far no evidence on the existence of antimatter. As a consequence, many scientists are working on finding the missing antimatter or any other phenomena capable of explaining the observed asymmetry between matter and antimatter.

However, research does not have to restrict itself to the observation of astrophysical phenomena in order to investigate the case of the missing antimatter. The profound symmetry of matter and antimatter can be studied in the laboratory using e. g. particles and antiparticles. By measuring and comparing their properties, their similarity or difference can be revealed. If both species have the same properties (apart from the sign of their charge) — which is the current state of our knowledge — an explanation of the broken symmetry at the Big Bang could not be given within the present theory of

the standard model of particle physics[1]. Consequently, any difference found in the laboratory frame would lead us one step closer to understanding where we come from.

In studying the properties of the most simple antimatter atom, the antihydrogen, consisting of a positron and an antiproton, a comparison of unprecedented precision to its matter counterpart, the hydrogen atom, is possible. Hence the examination of antihydrogen is extremely well suited to investigate a possible difference between matter and antimatter.

But as for every exciting story one should start at the beginning. Therefore, this chapter continues with a short journey through history[2], starting with the rise of atomic theory in early 1900 and inevitably leading to quantum mechanics and the prediction of antimatter. Because of its relevance for the thesis topic the latter part will be treated in a little more detail. Subsequently the actual discovery of the first antimatter particle, the positron is discussed as well as the first observation of antiprotons. The chapter is concluded with the presentation of the initial synthesis of antihydrogen.

1.1   The Road to Antimatter — A Historical Approach

Our understanding of the world evolved from more than two thousand years of scientific research and achievements. When studying physics today we learn that matter is composed of atoms. These atoms consist of a small nucleus in the center made of protons and neutrons and of electrons in the shell. The amount of the protons and shell electrons determines the properties of each element. All elements can be summarized in the periodic system of elements where they are grouped after increasing mass and according to their properties. All this knowledge comes very natural to us. We are basically raised with it along with 'water is wet and fire is hot'.

However, a century ago this understanding was absolutely not common knowledge. In 1895 the concept of atoms was widely used in chemistry but many physicists did not believe in it since strong evidence of their existence was lacking. Subatomic particles such as the electron, the proton or the neutron were not known at all. In 1895 William Conrad Röntgen caused

---

[1] According to the Charge Parity Time (CPT) symmetry necessary for all local quantum field theories such as the standard model of particle physics, matter and antimatter should differ e.g. in the sign of their charge. A difference e.g. in their masses, would lead to a violation of this fundamental symmetry, clearing the path for other theories or extensions which are then better capable of explaining the universe observed today. For more details on CPT symmetry and implications of possible violations see Chapter 2.

[2] Since a PhD thesis is not the place to narrate the history of atomic and particle physics in full detail, the interested reader is kindly referred to the excellent book of Robert Cahn and Gerson Goldhaber [2] where a more elaborate treatment of the historical development is given.

a sensation when discovering penetrating radiation which he came to call X-rays [3]. This discovery set the stage for new branches of physics research such as investigation of radioactivity by the Curies or scattering experiments by Rutherford.

In 1897 Joseph John Thomson discovered the electron as the first subatomic particle through his experiments with cathode rays and their deflection in electric and magnetic fields [4]. This discovery replaced the theory of hydrogen being the fundamental particle as postulated by William Prout in 1815 [5, 6].

In 1911 Ernest Rutherford and colleagues conducted some experiments using the scattering of alpha particles on thin metal foils [7, 8]. Through this, they discovered the nucleus and hence determined the structure of the atom. Rutherford's atom had a theoretically predictable size which was first calculated by Niels Bohr in 1913 using Planck's constant, the electron mass and its charge [9]. Bohr also 'resolved' the problem of stability of the atomic model by postulating that the moving electrons do not radiate and hence do not loose energy — a very bold thing to do. Between 1924 and 1927 quantum mechanics developed rapidly, bringing forth major achievements such as Heisenberg's uncertainty relation and Schrödinger's famous equation.

1.2 Dirac's Equation

Schrödinger's equation[3] was a major discovery and is the most fundamental equation of non-relativistic quantum mechanics:

$$\mathrm{i}\hbar\frac{\partial}{\partial t}\psi(\vec{x},t) = \left\{\frac{-\hbar^2}{2\mathrm{m}}\triangle\vec{x} + \mathrm{V}(\vec{x})\right\}\psi(\vec{x},t) \tag{1.1}$$

It is derived from the classical definition of energy

$$E = \frac{p^2}{2\mathrm{m}} + \mathrm{V}(\vec{x}) \tag{1.2}$$

by replacing the classical variables with differential operators

$$E = \mathrm{i}\hbar\frac{\partial}{\partial t} \qquad p = -\mathrm{i}\hbar\nabla\vec{x} \tag{1.3}$$

acting on a wave function [10]. Solving Schrödinger's equation for the hydrogen atom, basic understanding of spectroscopically observed lines can be obtained. However, no explanation of the substructures found in its spectrum is given. To account for these experimental findings, correction terms have to be added to the equation describing e. g. the spins of proton

---

[3]All equations stated in this section are normalized to the speed of light c. Hence c is omitted in the notation.

and electron as well as their interactions (for more details see Section 2.2). These effects cannot be derived from Schrödinger's non-relativistic theory in a strictly formal way.

To cope with this problem, one can replace the classical expression for the energy with the relativistic term

$$E^2 - p^2 - \mathrm{m}^2 = 0 \tag{1.4}$$

and proceed in the same way as for Schrödinger's equation (for reasons of simplicity only the case of a free particle is treated). This leads to the Klein–Gordon equation:

$$\frac{\partial^2}{\partial t^2}\psi(\vec{x}, t) = \left\{ \triangle \vec{x} - \frac{\mathrm{m}^2}{\hbar^2} \right\} \psi(\vec{x}, t) \tag{1.5}$$

However, this concept causes difficulties in the interpretation of the wave function ψ and the nonlinearity of the time derivative conflicts with transformation theory [10].

It was Paul Dirac who proposed a fully relativistic equation [10, 11] based on the linearization of the relativistic term for the kinetic energy in 1928:

$$E^2 - p^2 - \mathrm{m}^2 = (\gamma_0 E + \gamma^\mu p_\mu - \mathrm{m})(\gamma_0 E + \gamma^\mu p_\mu + \mathrm{m}) = 0 \tag{1.6}$$

This equation is satisfied if one of the terms equals zero. Hence using only the first term and substituting again the variables for differential operators leads to Dirac's famous equation:

$$\gamma_0 \frac{\partial}{\partial t} - \gamma^\mu \partial x_\mu - \mathbb{1}\frac{\mathrm{m}}{\mathrm{i}\hbar} = \mathbb{0} \tag{1.7}$$

with the 4×4 gamma matrices,

$$\gamma_0 = \begin{pmatrix} 0 & \mathbb{1} \\ \mathbb{1} & 0 \end{pmatrix} \qquad \gamma_1 = \begin{pmatrix} 0 & \sigma_{\mathrm{x}_1} \\ -\sigma_{\mathrm{x}_1} & 0 \end{pmatrix}$$

$$\gamma_2 = \begin{pmatrix} 0 & \sigma_{\mathrm{x}_2} \\ -\sigma_{\mathrm{x}_2} & 0 \end{pmatrix} \quad \gamma_3 = \begin{pmatrix} 0 & \sigma_{\mathrm{x}_3} \\ -\sigma_{\mathrm{x}_3} & 0 \end{pmatrix} \tag{1.8}$$

the 4×4 unity matrix $\mathbb{1}$ as well as the 4×4 null matrix $\mathbb{0}$. The spin is contained inherently in this equation which can be nicely seen since the Dirac matrices contain the Pauli matrices $\sigma_{\mathrm{x}_i}, (i = 1, 2, 3)$ which are used to describe the spin in the non-relativistic case. In spite of its beauty, Dirac's equation only holds true for particles with spin $\mathrm{n}\cdot\frac{\hbar}{2}$ but not for particles with integer spin such as e. g. pions.

The solution for Dirac's equation are vectors with four components, the so called spinors. These spinors contain two separate type of particles with equal mass but opposite charge. Antimatter was born.

1.3 Antimatter Discovered

In 1932 Carl D. Anderson studied cosmic rays in the lab using a cloud chamber inside a magnetic field for visualizing particle tracks [12]. With his setup he discovered an interesting track signature that seemed to be caused by one positively charged particle much lighter than the proton. After careful considerations Anderson came to call it positron (for more details see Appendix A.1).

At that time however, it was not clear if even the proton was fully described by Dirac's equation in the same way as the electron, since this would imply the existence of an antiproton which was not observed yet. This question was solved in 1955, when the antiproton was discovered at the Berkeley National Laboratory in an experiment conducted by Owen Chamberlain and Emilio Segrè (for details see Appendix A.2). The first antiprotons were produced by extracting a proton beam of 6.2 GeV out of the Bevatron accelerator onto a copper target giving experimental proof of the validity of Dirac's equation for the proton as well [13]. For this achievement Segrè and Chamberlain were awarded the Nobel prize in 1959.

In 1995, precisely 40 years after the discovery of the antiproton, the first antihydrogen atoms were produced at the low energy antimatter ring (LEAR) at CERN [14] causing a sensation not only within the scientific community but also with the broad public (a more detailed description is given in Appendix A.3). However, the LEAR experiment was not suitable to produce large amounts of slow antihydrogen (in total 9 antihydrogen atoms were detected within 15 hours) which are necessary for detailed studies. In order to increase the antihydrogen production, a new technique for its formation was required. This technique is based on confining positrons and antiprotons together inside the same trap. Since the antiprotons delivered by LEAR were way too fast for any trap to accept, a new ring, the antiproton decelerator AD (see Appendix B.1), was constructed.

It was finally in 2002 that two groups [15, 16, 17] succeeded in producing antihydrogen in larger quantities by implementing the concept of mixing antiproton and positron plasmas in a nested trap. These experiments set the stage for the research on slow and trapped antihydrogen. With the first trapping of the produced antihydrogen achieved in 2010 [18] and the first formation of antihydrogen in a cusp trap [19], we are really on the brink of the beginning of the next chapter in antimatter physics: the spectroscopy of antihydrogen.

Chapter 2

Theoretical Background

Within the framework of the standard model of particle physics — a model capable of explaining many phenomena observed in previous and existing particle physics experiments — equal amounts of matter and antimatter should have been produced at the Big Bang. Possible explanations for an asymmetry at the beginning of our universe, responsible for an excess of matter, hence include extensions to the standard model. Some of them require violations of its inherent charge-parity-time (CPT) symmetry, others do not. In this chapter, the CPT theorem as well as theoretical extensions of the standard model of particle physics will be discussed in more detail. Since the comparison of very well known transitions within the hydrogen atom to the yet unknown corresponding properties of the antihydrogen atom poses a good candidate to test possible CPT violations, the structure of the hydrogen atom is summarized in the following as well, focusing on the hyperfine splitting transitions which are very well suitable for spectroscopic precision experiments.

2.1 The CPT Symmetry

For each local and Lorentz invariant quantum field theory, the conservation of the three fundamental symmetries, charge (C), parity (P) and time (T), is a necessary condition [20]. This symmetry implies that the laws of physics hold true for any system where the charges of the known particles change to opposite sign, the spatial directions are mirrored and the time flow is inverted. So antimatter moving in a mirror universe where time goes backwards should behave in exactly the same way as matter in our universe. For a long time it was believed that not only the combination of the three transformations was preserved, but also each single one on its own. However, in 1956 Tsung-Dao Lee and Chen Ning Yang published a paper on the weak interaction including a possible violation of parity and charge-parity symmetry [21]. The experimental proof for P non-conservation was found a

year later by Chien-Shiung Wu [22] when investigating the beta decay of the Cobalt isotope ^{60}Co — a result which was totally unexpected. Nevertheless, it was believed that even though parity was not conserved, the combination of charge conjugation and parity transformation still was. This was shattered in 1964 when James Cronin and Val Fitch presented experimental proof for CP symmetry breaking in neutral kaon systems [23]. For their discovery and its large impact on physics they were awarded the Nobel prize in 1980 [24, 25].

The fact of CP violation together with possible baryonic instability and fluctuation in the thermal equilibrium of space in the early universe (Sakharov criteria) [26] gave rise to possible theoretical explanations of the observed asymmetry of matter and antimatter see e. g. [27, 28]. However, all of these theories are not conclusive yet since strong experimental proof for their ingredients, such as supersymmetric particles, the Higgs boson[1] or heavy antimatter nuclei is still lacking. Also the CP violation measured in the lab is too small to quantitatively explain the observed baryon asymmetry but at an energy scale right after the Big Bang, a different type of CP violation might have been present.

Another approach to describe the observed matter-antimatter asymmetry includes CPT violation [29, 30] and is often found in string theory[2]. These theories only need non-conservation of baryonic number and CPT breaking as ingredients to account for the observed excess of matter.

A possible consistent expansion of the standard model incorporating microscopic CPT and Lorentz violating effects was given by Don Colladay and Alan Kostelecký [31]. It leads to additional terms in the Lagrangian of the standard model and hence to a modified Dirac equation[3]:

$$(\mathrm{i}\gamma^\mu D_\mu - m_\mathrm{e} - a_\mu^\mathrm{e}\gamma^\mu - b_\mu^\mathrm{e}\gamma_5\gamma^\mu - \frac{1}{2}H_{\mu\nu}^\mathrm{e}\sigma^{\mu\nu} +$$
$$+ \mathrm{i}c_{\mu\nu}^\mathrm{e}\gamma^\mu D^\nu + \mathrm{i}d_{\mu\nu}^\mathrm{e}\gamma_5\gamma^\mu D^\nu)\Psi = 0 \quad (2.1)$$

where γ are the Dirac matrices, m_e is the electron mass and $\mathrm{i}\,D = \mathrm{i}\,\partial_\mu - qA_\mu$ with charge q and Coulomb potential A_μ. The coefficients $a_\mu^\mathrm{e}, b_\mu^\mathrm{e}, c_{\mu\nu}^\mathrm{e}, d_{\mu\nu}^\mathrm{e}, H_{\mu\nu}^\mathrm{e}$ violate Lorentz symmetry and $a^\mathrm{e}, b^\mathrm{e}$ additionally violate CPT. This equation holds true for the free proton as well — only the coefficients are changed: $a^\mathrm{e} \to a^\mathrm{p}$, $b^\mathrm{e} \to b^\mathrm{p}$, $c^\mathrm{e} \to c^\mathrm{p}$ and $d^\mathrm{e} \to d^\mathrm{p}$

This leads to an energy shift of the $1s$ and $2s$ hyperfine levels of atoms with the basis state $|m_J, m_I\rangle$ where m_J is the projection on the z-axis of the electron angular momentum and m_I the projection on the z-axis of the

---

[1]Strong evidence of the existence of a 125 - 126 GeV standard model Higgs boson has been found recently.

[2]CPT violation is especially interesting for string theories, since they deal with extended objects and not point-like particles.

[3]This equation describes a free electron. For all the equations in this section $\hbar = \mathrm{c} = 1$.

proton angular momentum respectively. In case of hydrogen, the obtained energy shift is:

$$\Delta E^{\mathrm{H}}(m_J, m_I) \approx (a_0^{\mathrm{e}} + a_0^{\mathrm{p}} - c_{00}^{\mathrm{e}} m_{\mathrm{e}} - c_{00}^{\mathrm{p}} m_p)$$
$$+ (-b_3^{\mathrm{e}} + d_{30}^{\mathrm{e}} m_{\mathrm{e}} + H_{12}^{\mathrm{e}}) m_J / |m_J|$$
$$+ (-b_3^{\mathrm{p}} + d_{30}^{\mathrm{p}} m_{\mathrm{p}} + H_{12}^{\mathrm{p}}) m_I / |m_I| \qquad (2.2)$$

where m_{e} is the electron or positron mass and m_{p} the proton or antiproton mass. For antihydrogen, some coefficients ($a_\mu^{\mathrm{e,p}}$, $d_{\mu\nu}^{\mathrm{e,p}}$, $H_{\mu\nu}^{\mathrm{e,p}}$) in Eq. 2.2 change sign and hence the energy shifts can be different for hydrogen and antihydrogen.

In order to study CPT symmetric behavior or its absence within this theoretical framework, it is desirable to compare the best known properties of matter, namely the best known transitions in hydrogen, with their analogon in antimatter as suggested by Robert Bluhm and Alan Kostelecký [32, 33]. For this, one of the most promising candidates is the hyperfine splitting transition frequency in antihydrogen since leading order effects of CPT violation are predicted to occur within it [32].

This transition frequency for matter is known to a precision of 10^{-12} [34, 35] and thus studying its antimatter counterpart with similar precision would challenge the current most sensitive limit for CPT violation which was found in the neutral kaon system [36, 37]. Another important point is that the coefficients occurring in the Lagrangian of the standard model extension are not dimensionless but have the dimension of energy. Hence it is necessary to compare absolute values of the transition frequencies instead of relative ones as it is the case in the neutral kaon system. Therefore the measurement of the ground-state hyperfine transition of antihydrogen with a precision of 10^{-4} would already lead to a CPT test comparable to the current most sensitive limit (Fig. 2.1) [38].

Since this thesis contributes to this measurements the hyperfine structure of hydrogen will be discussed in more detail in the following section.

2.2 Hyperfine Structure in Hydrogen

Hydrogen is one of the best known substances in the world. It is one of the few systems for which the Schrödinger equation can be solved analytically making it valuable for theoretical investigations. Also an experimental value with particularly high precision ($1s$ – $2s$ transition, relative precision: $4.2 \cdot 10^{-15}$) can be found within the hydrogen atom [40].

The spectral lines in hydrogen have been first described by empirical formulas. Later on, it was Niels Bohr who could derive these formulas from certain theoretical postulates he formulated. Though a successful theory, it was quantum mechanically not fully correct. The non-relativistic treatment of electronic transitions inside the hydrogen atom within the framework of
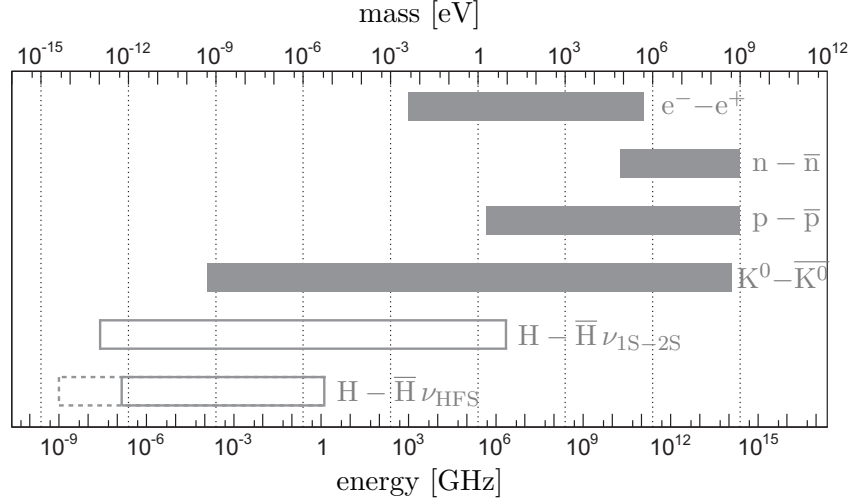
Figure 2.1: *Comparison of the accuracy of different CPT tests. As can be seen, the relative precision (length of the bar) of the currently most sensitive CPT limit is 10^{-18}. However, this corresponds to an absolute precision (left edge of the bar) of only $100\,kHz$. Thus, a relative precision of 10^{-4} of the ground-state hyperfine splitting transition frequency at $1.42\,GHz$ would already be competitive. (Picture adapted from [39])*

quantum mechanics was done using Schrödinger's famous equation. With a Coulomb potential in the Hamiltonian of the Schrödinger equation, the solution for the energy levels has the form:

$$E_n = -\frac{m_{\mathrm{r}} \cdot \mathrm{e}^4}{8 \cdot \epsilon_0^2 \mathrm{h}^2} \cdot \frac{1}{n^2} = -\mathrm{Ry} \cdot \frac{1}{n^2} = -(13.6\,\mathrm{eV}) \cdot \frac{1}{n^2} \qquad (2.3)$$

where e is the elementary charge, n the principle quantum number, Ry the Rydberg unit of energy and m_{r} the reduced mass

$$m_{\mathrm{r}} = \frac{m_{\mathrm{e}} + m_{\mathrm{p}}}{m_{\mathrm{e}} \cdot m_{\mathrm{p}}}.$$

This formula accounts for the experimentally observed spectral lines of hydrogen.

The problem arises when the spectroscopical resolution is increased, as each spectral line is found to have a substructure. This phenomenon is called the fine structure. Its occurrence is due to the alignment of the electron spin $\vec{s_{\mathrm{e}}}$ with respect to the angular momentum $\vec{l_{\mathrm{e}}}$ [4] as well as relativistic corrections for the electron energy. In this case, both, the angular momentum as well as the spin, are no longer conserved whereas their sum, the total angular momentum $\vec{j} = \vec{s_{\mathrm{e}}} + \vec{l_{\mathrm{e}}}$ is conserved. The energy levels including the

---

[4]Depending on whether both vectors are parallel or antiparallel, the energy is either higher of lower.

fine structure corrections now have the form:

$$E_{n,j} = E_n \left\{ 1 + \frac{(Z\alpha)^2}{n} \left(\frac{1}{j + \frac{1}{2}} - \frac{3}{4n} \right) \right\} \tag{2.4}$$

where Z is the proton number and α is the fine structure constant.

Looking even closer, the fine structure lines again have a substructure which is due to the coupling of the total angular momentum of the electron and the total angular momentum of the proton $\vec{I}$ to the total angular momentum of the atom[5] $\vec{F} = \vec{j} + \vec{I} = (\vec{s_e} + \vec{l_e}) + (\vec{s_p} + \vec{l_p})$.

Summarizing the effects presented above, the corrected (radial) Schrödinger equation for the hydrogen atom including the fine structure and the hyperfine structure corrections is:

$$\frac{\mathrm{d}^2 u(r)}{\mathrm{d}r^2} + \frac{2m_r}{\hbar^2} \left[E - V(r) - \frac{l(l+1)\hbar^2}{2m_r r^2} - \right.$$
$$\left. - \frac{Z\alpha\hbar}{2m_e^2 c r^3}(\vec{s}\vec{l}) + \frac{\mu_p \mu_K}{s_p j \hbar^2}(\vec{s_p}\vec{j}) \right] u(r) = 0 \quad (2.5)$$

where $u(r)$ is the spatial wave function, l is the angular momentum quantum number, c the speed of light, $\vec{s}$ the spin vector of the electron, $\vec{l}$ the angular momentum vector of the electron, μ_p the magnetic moment of the proton, μ_K the magnetic moment of the nucleus, s_p the spin quantum number of the proton and $\vec{s_p}$ the spin vector of the proton.

For the hydrogen (antihydrogen) ground-state hyperfine splitting, the coupling of the electron and proton (positron and antiproton) spins results in two F states[6]: $F = 0$, a singlet state with $M = 0$ (M being the projection onto the axis of a magnetic field) and $F = 1$, a triplet state with $M = -1, 0, 1$. This is illustrated in Fig. 2.2. These states have different energies depending on the orientation of the electron and proton spin with respect to each other. If no external magnetic field is present, the triplet states are degenerate according to classical quantum theory[7].

When applying an additional external magnetic field, the degeneracy is lifted (Fig. 2.2). Depending on the strength of the field, the energies of all four states — singlet and triplet — are shifted by different amounts (Fig. 2.3). For weak fields, the shift is not very big (Zeemann effect, left side of Fig. 2.3) and the coupling of the proton and electron spin still holds. At higher magnetic field, the shift is larger than the coupling of the spins and hence breaks it off (Paschen-Back effect, right side of Fig. 2.3).

---

[5]In case of the ground-state hyperfine structure of (anti)hydrogen, the angular momentum for proton and electron is 0 and hence the electron and proton spins couple to the total angular momentum $\vec{F} = \vec{s_e} + \vec{s_p}$.

[6]In this case F denotes the quantum number corresponding to the total spin vector $\vec{F}$.

[7]However, in the standard model extension presented above, the triplet states differ in energy even at zero external field.

Hyperfine splitting

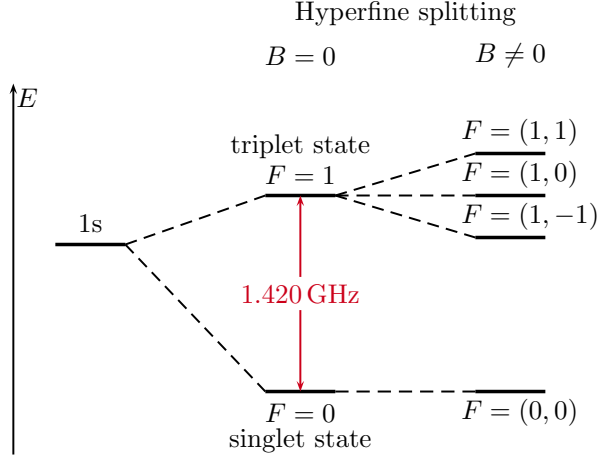$B = 0$ $B \neq 0$

Figure 2.2: *(Color) Illustration of the hyperfine splitting effect in the energy levels of the ground state of hydrogen. The electron and proton spins couple to the total spin $\vec{F}$, resulting in a singlet and a triplet state, depending on the orientation of the spins with respect to each other. With no external magnetic field present, the triplet state is degenerate with a transition frequency between both states of 1.420 GHz. Only with an external magnetic field, this degeneration is lifted, causing an energy shift of each state. For antihydrogen, the order of these levels is different, since the magnetic moments of antiprotons and positrons are opposite in sign.*

The four states can be grouped into two pairs according to their behavior in an inhomogeneous magnetic field. The $(F, M) = (1, -1)$ and $(F, M) = (1, 0)$ states will be deflected into regions with lower fields and hence are called low field seeker states (LFS). The other two, namely the $(F, M) = (1, 1)$ and $(F, M) = (0, 0)$, will be deflected into regions with higher fields and are consequently named high field seeker states (HFS).

With no external magnetic field present, the transition between the hyperfine states $F = 0$ and $F = 1$ has the characteristic frequency of 1.42 GHz (famous 21 cm line of hydrogen) (Fig. 2.2). This frequency is proportional to the proton (antiproton) magnetic moment via:

$$\nu_{\mathrm{HFS}} = \frac{16}{3} \left(\frac{m_{\mathrm{p}}}{m_{\mathrm{p}} + m_{\mathrm{e}}} \right)^3 \frac{m_{\mathrm{e}}}{m_{\mathrm{p}}} \frac{\mu_{\mathrm{p}}}{\mu_{\mathrm{N}}} \alpha^2 \mathrm{c} \, R_\infty (1 + \Delta) \tag{2.6}$$

where m_{p}, m_{e} are the masses of the proton (antiproton) and electron (positron), μ_{p} the magnetic moment of the proton (antiproton), μ_{N} the nuclear magneton, α the fine structure constant, c the speed of light, R_∞ the Rydberg constant and Δ a correction term due to higher-order quantum electrodynamic (QED) and quantum chromodynamic (QCD) effects. Measuring this frequency thus allows very accurate determination of the magnetic moment of the proton or the antiproton, providing insight into the fundamental properties of both.
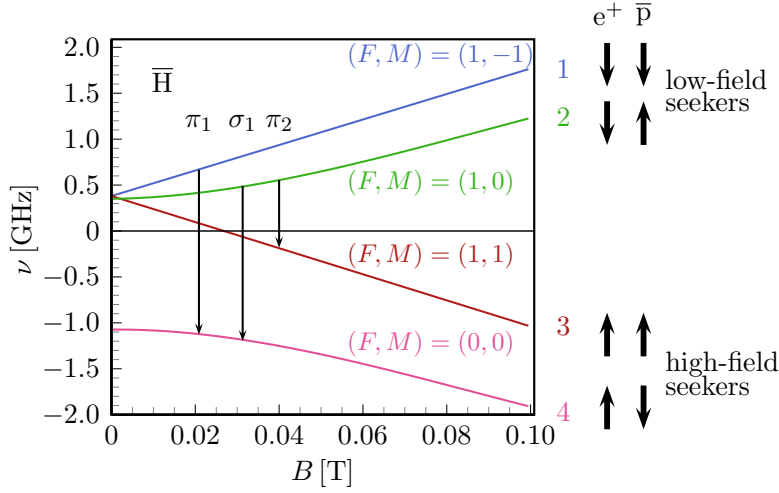
Figure 2.3: *(Color) Breit-Rabi diagram of the evolution of the four hyperfine states of the ground-state antihydrogen atom as a function of the magnetic field strength. According to the direction of electron spin and proton spin with respect to each other and the strength of the external magnetic field, the states have different energies. These four states can be divided into two groups depending on their behavior in an inhomogeneous magnetic field. The singlet and the lowest triplet states are deflected into regions with higher magnetic field. Consequently, they are called high field seeker states (HFS). The other two triplet states are deflected into regions with lower magnetic field. They are therefore called low field seeker states (LFS). (Picture adapted from [41])*

However, when an external magnetic field is present, not only one transition, but several can be measured — three of them involving an electron spin-flip (Fig. 2.3). The energy shift between these levels is given by the Rabi equation:

$$E_M = \frac{\Delta E_0}{2(2I+1)} + \mu_B g_I H M \pm \frac{\Delta E_0}{2}\left(1 + \frac{4M}{2I+1}x + x^2\right)^{\frac{1}{2}} \qquad (2.7)$$

$$\text{with} \quad x = \frac{(g_J - g_I)\mu_B H}{\Delta E_0}$$

where ΔE_0 is the transition energy without external field, μ_B the Bohr magneton, g_J, g_I the electronic and nuclear g-values and H the strength of the external magnetic field. For antihydrogen, the sign of both terms is inverted due to the opposite sign of the nuclear moment. Thus the lines shown in Fig. 2.2 change the order for antihydrogen.

An experimental setup dedicated to measure the magnetic moments of nucleons by measuring e. g. ground-state hyperfine structure transition in hydrogen or other splittings in hydrogen-like atoms and its adaption to measurements with antihydrogen is presented in the next chapter.

Chapter 3

Experimental Setup

The comparison of atomic transitions within the hydrogen atom with the corresponding ones in antihydrogen provides an excellent means to test the CPT symmetry. In case of hydrogen, several transitions have been measured with a very high precision using either optical or microwave spectroscopy. Especially the method of Isidor Rabi using a spectrometer line for determination of the magnetic moments of nuclei can be adapted for the case of antihydrogen. Hence, the chapter opens with an overview of the experimental setup used for the ground-state hyperfine structure transition measurements of hydrogen with special emphasis on the measurement principle. Subsequently, the implementation of this concept for measurements of antihydrogen is presented, followed by a detailed description of the individual components of the spectrometer line along with the production channels of antihydrogen used in the experiment.

3.1 The Rabi Experiment

It was in 1938 when Isidor Isaac Rabi proposed an experiment [42, 43] based on the previous conducted measurements done by Otto Stern and Walther Gerlach [44] to measure nuclear magnetic moments with unprecedented precision.

The setup (Fig 3.1) consists of a source providing an atomic or molecular beam, an inhomogeneous magnetic field region, one homogeneous magnetic field superimposed with an oscillating magnetic field, a second inhomogeneous magnetic field region and a detector.

The atoms or molecules provided by the source are selected according to their spin states in the first inhomogeneous magnetic field region. They pass the homogeneous magnetic field and are deflected in the second inhomogeneous field region to hit the detector[1]. However, if the rotating field that

---

[1] The inhomogeneous fields that act as spin selectors are the Stern-Gerlach parts of the experiment.
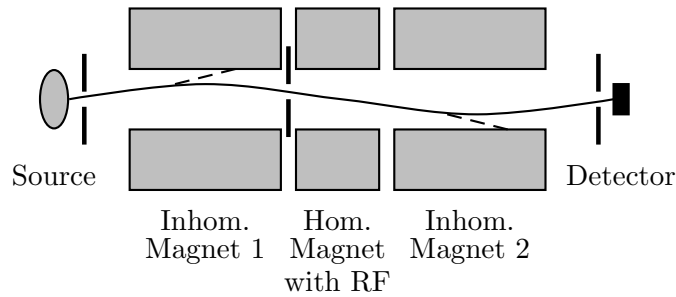
Figure 3.1: *Schematic drawing of the experimental setup proposed by I. I. Rabi to measure the magnetic moments of nuclei. The beam emitted by the source and collimated by the first slit passes a region with an inhomogeneous magnetic field. In this region, one spin state is selected as originally demonstrated by O. Stern and W. Gerlach. The beam passes then a region with a homogeneous field with a superimposed radio frequency (RF) field. Depending on the frequency, the beam is then either focused by the second inhomogeneous field region, or if a spin-flip was induced by the radio frequency field, deflected. Thus the observable change in count rate at the detector is a very precise means to determine the transition frequency between two different spin states.*

is superimposed on the homogeneous field is set to resonance with a transition, a spin-flip is induced, causing a deflection in the second inhomogeneous field. Hence the beam does not hit the detector anymore. This allows the measurements of the transition frequencies with very high precision.

In such a setup, there are two possibilities to induce the resonance in the passing beam. One can either adjust the field strength of the homogeneous field and keep the rotating field constant (molecular beam magnetic resonance technique) or, as was done later by Rabi, one can keep the homogeneous field constant and vary the rotating field. This technique provided the basis for microwave spectroscopy and enabled the development of magnetic resonance imaging widely used in medicine.

Also the principle of atomic clocks is based on Rabis experiment and the refinement of his technique by Norman Foster Ramsey [45].

Rabis principle can also be adopted for measurements of the ground-state hyperfine splitting transitions in antihydrogen[2]. The experimental implementation of this is presented in the next section.

---

[2]Even though the most precise measurements on the hydrogen ground-state hyperfine transition are achieved with a hydrogen maser [35], this is not easily adoptable for antihydrogen. The hydrogen maser uses a Teflon coated bulb to store the atomic hydrogen. Since the stored atoms collide with the Teflon wall, this would cause annihilation in case of the antihydrogen making it impossible to store it for a large amount of time. However, this would be a necessary condition for maser emissions.

3.2 Spectroscopy of Antihydrogen

The ASACUSA (Atomic Spectroscopy And Collisions Using Slow Antiprotons) collaboration is aiming for spectroscopy of the hyperfine transition in antihydrogen using a Rabi-like spectrometer line. A schematic drawing of the experimental setup is given in Fig. 3.2 and an isomeric overview in Fig. 3.3.
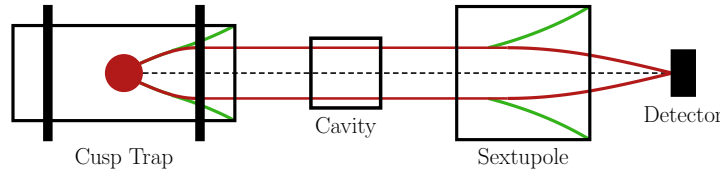

Figure 3.2: *(Color) Schematic drawing of the ASACUSA spectrometer line used for the measurement of the hyperfine transition in antihydrogen. Inside the cusp trap, positrons and antiprotons combine to antihydrogen which is extracted as a partially polarized beam containing predominantly low field seeker atoms. These atoms are then projected onto a radio frequency cavity (this work), where, depending on the frequency of the oscillating field, a spin-flip is induced, possibly converting the low field seeker to high field seeker states. In the subsequent sextupole magnet only the low field seeker atoms are focused onto a detector while the atoms that were flipped to the high field seeker states are deflected. This causes a change of the count rate at the detector and hence a dependence on the frequency of the oscillating magnetic field of the cavity.*

The first stage is the creation of the antihydrogen itself. This is done by capturing the antiprotons provided by the CERN antiproton decelerator (AD, see Appendix B.1). The antiprotons coming form the AD are further decelerated by a radio frequency quadrupole (RFQ, see Appendix B.4) and subsequently caught in a Penning trap. Together with accumulated positrons, they are injected in a cusp trap (see Section 3.2.1) where ground-state antihydrogen is formed when both species mix. This has been successfully demonstrated in 2010 [19]. The magnetic field of the trap is shaped such, that it allows the extraction of a partially polarized antihydrogen beam containing more low field seeker (LFS) than high field seeker (HFS) atoms. This beam is then projected onto a microwave cavity which was developed in the context of this thesis, and from the cavity to a superconducting sextupole magnet with a maximum field of 3 T, focusing the beam onto a multi channel plate (MCP) detector.

Depending on the radio frequency (RF) field of the cavity — the resonance frequency of interest is 1 420 405 751.7667 ± 0.0009 Hz for hydrogen [35] — a spin-flip is induced in the passing atoms converting them from the LFS to the HFS state. This causes a deflection instead of a focusing in the subsequent sextupole magnet and hence a change in the count rate of the detector is observed (Fig. 3.4). The expected double dip shape is due to a superposition of several effects. These are the natural line shape, the field
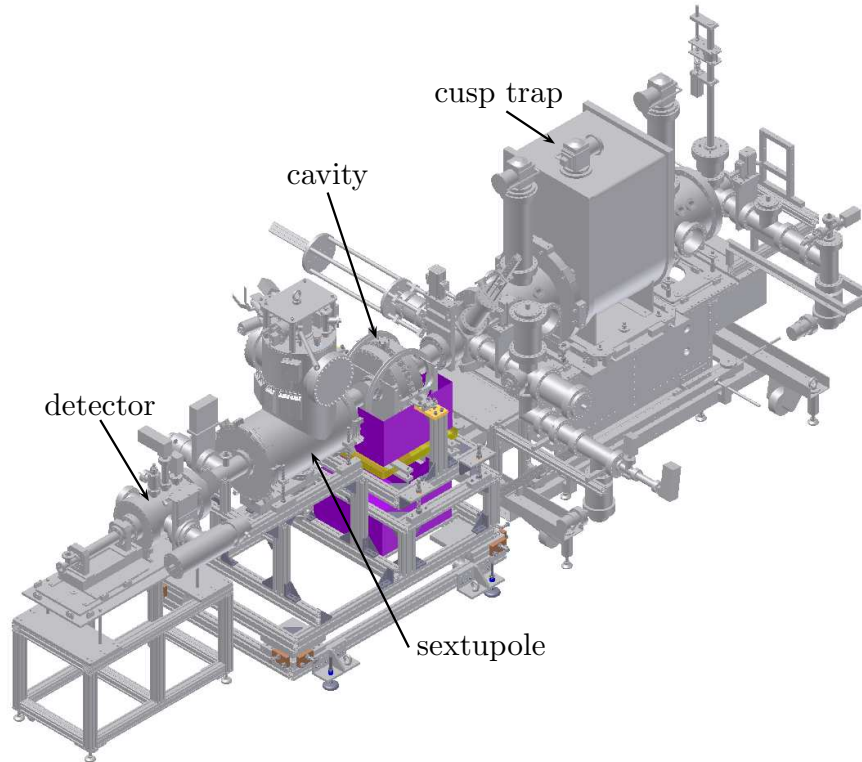
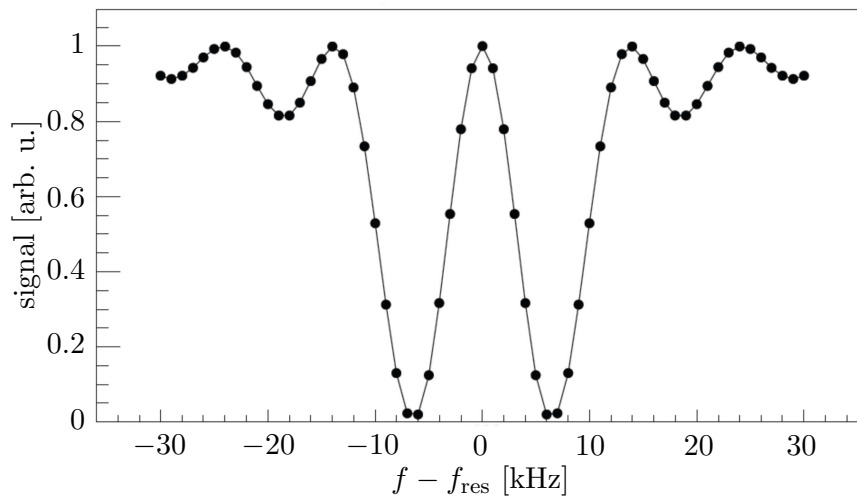**Figure 3.3:** *(Color) Isometric view of the experimentally implemented setup.*

Figure 3.4: *Expected response of the antihydrogen detector. The line shape is due to a combination of several effects: the natural line shape, the field geometry of the oscillating field and the velocity of the atoms. (Picture adapted from [39])*

geometry of the oscillating field and the velocity of the atoms [46] (see also Section 4.2).

In the following, a more detailed description of the single elements of the spectrometer line will be given. The spin-flip cavity, being the central piece of this thesis, is treated in greater detail in Chapter 4.

3.2.1 The Traps

In total, three traps are used to produce antihydrogen in the ground state. Two traps are used to accumulate antiprotons and positrons, respectively, whereas the third is dedicated to the formation of antihydrogen. An isometric overview of the three traps is given in Fig. 3.5
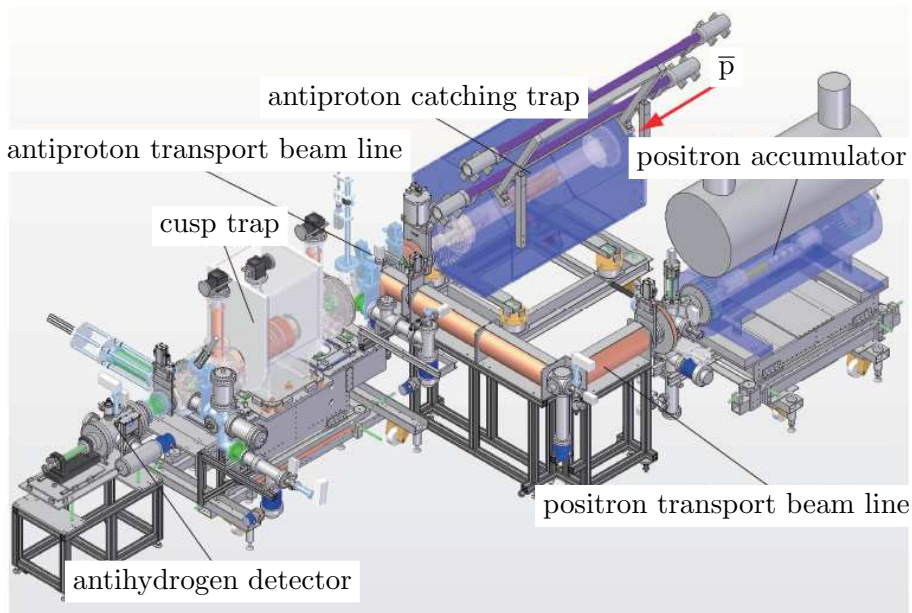
Figure 3.5: *(Color) Isometric view of the three trap system implemented at ASACUSA to produce ground-state antihydrogen. The antiproton catching trap (left) confines the antiprotons ($\bar{\mathrm{p}}$) coming from the RFQ. The positron trap (right) accumulates and confines positrons from a radioactive sodium source ($^{22}_{11}Na$). The particles from both traps are delivered to the cusp trap (front left) where positrons and antiprotons recombine to form antihydrogen. (Picture adapted from [47])*

The Trapping Principle

All three traps share more or less the same configuration: They are variants of a Penning trap consisting of multi ring electrodes (Mre) to produce a potential for longitudinal confinement and a surrounding magnet to capture

the particles radially. Losses inside the traps are minimized by maintaining an excellent vacuum of better than 10^{-12} mbar. A brief overview over the specific trap layouts will be given in the following. For a more detailed description, the reader is referred to [19, 47] as well as references therein.

Confinement of Antiprotons

The first trap [48, 49] is dedicated to confine the antiprotons which are delivered by the AD and further decelerated in the RFQ to an energy of 110 keV.

When entering the trap, the beam passes through two thin polyethylene terephtalate (PET) foils[3] equipped with thin silver strips. They are acting as a beam profile monitor, using the signal induced by the passing antiprotons to center the beam into the trap. In addition, they are used to protect the vacuum inside the trap.

After the foils, 14 gold-plated copper ring electrodes (the MRE) are placed, providing a potential geometry for longitudinal confinement of the antiprotons (Fig. 3.6). Cooling of the particles is achieved by electrons already stored in the trap, since the antiprotons transfer their momentum to the electrons and are thus cooled down. The excited electrons cooled down due to synchrotron radiation inside the strong magnetic field (5 T) of the surrounding solenoid.

After this first cooling step, the antiprotons are compressed by a rotating electric field created by a segmented electrode using a radio frequency signal [49]. Finally, extractor electrodes eject and focus the compressed antiproton cloud as an ultra slow beam (100 – 250 eV) containing roughly 10^6 antiprotons. These electrodes compensate for the diverging field lines occurring outside of the superconducting solenoid[4].

Positron Trap

Parallel to the antiproton catching trap, a positron trap [50, 51] is used to accumulate positrons emitted by a sodium source[5]. The source as well as the trap itself are housed in a 5 T superconducting magnet, providing a field with $\geq 95\%$ homogeneity in the center to convey the isotropically emitted positrons along the field lines towards the trap. The magnet is ramped down with a speed of 1 T per second after ejection of the positrons, so that no perturbations affect the antiproton beam in the adjacent beam line (Fig. 3.5).

The source itself has a tungsten and stainless steel shielding, including a shutter that is opened only when positrons are accumulated. In order to

---

[3]The foils have a thickness of 90 μg/cm^2.

[4]In the trapping region, this solenoid provides a field with 99% homogeneity.

[5]The source uses the decay channel of $^{22}_{11}$Na to $^{22}_{10}$Ne via β^+ decay. The sodium isotope has a half-life of 2.6 years.
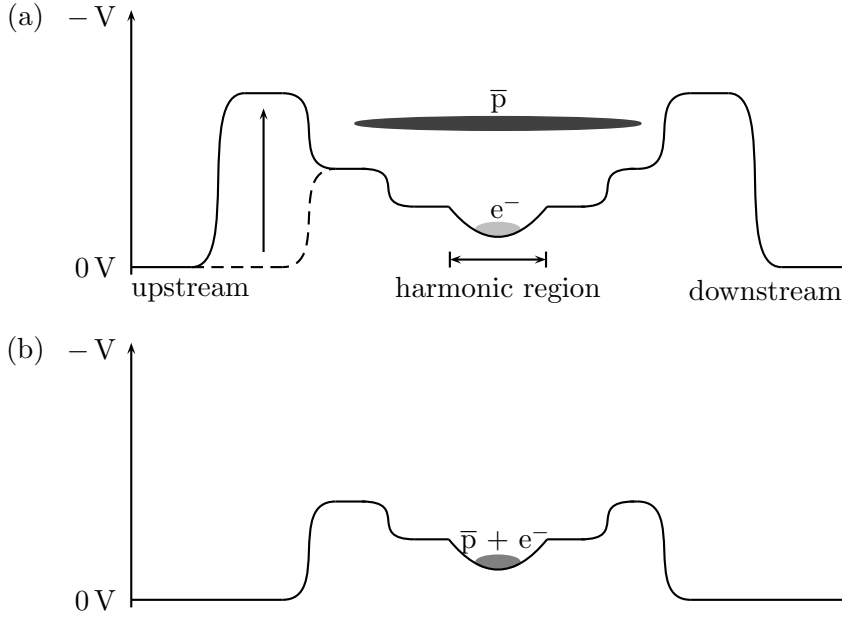
Figure 3.6: *Potential distribution at injection (a) and after 40 s of cooling (b). For injection of the antiprotons into the trap, the potential is lowered on the left side (dashed line). Once all the antiprotons are inside the trap, the potential is increased to confine them. The electrons already stored inside the trap allow cooling of the injected antiprotons. (Picture adapted from [47])*

be captured, the emitted positrons pass through a moderator — a polycrystalline tungsten layer of $4\,\mu$m thickness — and a subsequent gas chamber, consisting of 6 aluminum alloy electrodes filled with nitrogen gas (Fig. 3.7). Positrons with low energy are then captured inside the potential well created by 22 gold-plated aluminum alloy multi-ring electrodes located after the gas chamber. The ones with higher energy, however, cannot be captured yet. Nevertheless, they loose energy when passing through the gas chamber and finally hit a second moderator at the end of the MRE. This moderator — a tungsten crystal as well but with $25\,\mu$m thickness — slows down the positrons and reflects them backwards through the trap where they can finally be captured inside the potential as well.

Alltough the dense gas in the cell enables efficient cooling of the positrons at first, the collisions would cause a blow up of the positron cloud once it is cooled. So to ensure an efficient trapping, as little as possible rest gas from the gas chamber should be present inside the trap. A highly efficient differential pumping system is in use to satisfy this constraint.

With the current setup, shots containing $2 \cdot 10^6$ positrons can be extracted towards the cusp trap.
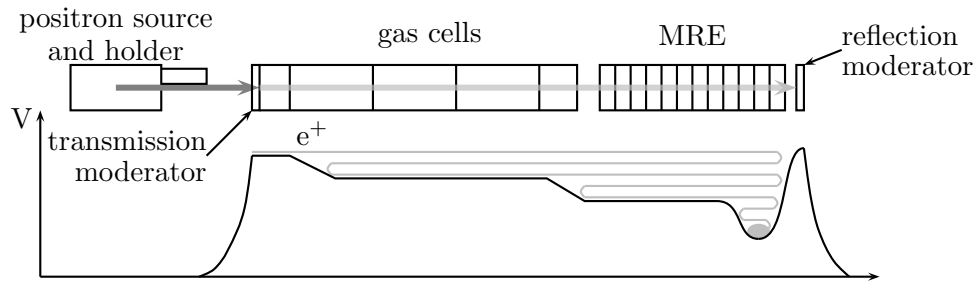
Figure 3.7: *Illustration of the positron accumulation from source to trapping. The positrons emitted from the source are slowed down by passing a moderator and a gas cell. Some of them are slow enough to be confined already, the others hit the reflection moderator at the end of the MRE. They are reflected backwards passing the gas cell again and are finally captured inside the potential as well. (Picture adapted from [47])*

Cusp Trap

Inside the cusp trap [19, 52], the actual antihydrogen formation (see 3.2.2) is initiated. The main difference to the other two traps is that the surrounding solenoid is replaced by five independent coils providing a maximum field of 3.4 T. They can create several different field geometries which is necessary for the extraction of the neutral antihydrogen atom. For this, an inhomogeneous field gradient is mandatory in order to couple to the small magnetic moment of the atom and thus steer the neutral atomic beam. Especially, the coils can be powered to create a cusp field[6] (Fig. 3.8), guiding the isotropically produced antihydrogen atoms according to their polarization (LFS selective) out along the field lines. This technique provides a slow and polarized antihydrogen beam containing predominantly LFS antihydrogen atoms in the ground state [53].

The MRE of the cusp trap consists of 17 gold plated aluminum alloy electrodes — two of them segmented for compression of the injected particles. The inner diameter of the MRE is with 80 mm considerably larger than the other two traps (40 mm for the antiproton and 42 mm for the positron trap), making room for the produced antihydrogen atoms since they are harder to confine than charged particles.

To reduce the thermal flow from the end caps of the trap, which are at ambient temperature, to the cryogenic MRE environment at 15 K[7], two thermal shields — one upstream and one downstream of the MRE — are installed. In addition they minimize the potential flow of residual gas into the trap.

---

[6]A cusp field is generated by a pair of coils, supplied with currents running in opposite direction. This configuration is also known as anti-Helmholtz coils.

[7]A cryogenic environment is necessary to ensure the excellent vacuum inside the trap.
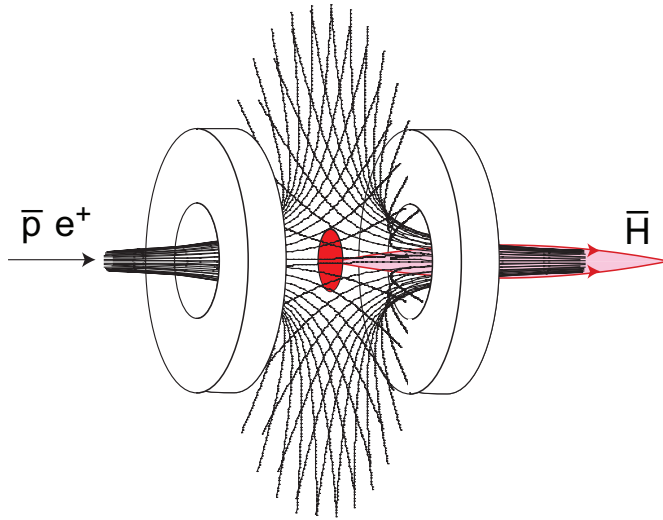
Figure 3.8: *(Color) Schematic view of the cusp field lines generated by a pair of anti-Helmholtz coils. This configuration allows the extraction of a partially polarized antihydrogen beam. (Picture courtesy B. Juhasz)*

3.2.2 Antihydrogen Production

The production processes for antihydrogen suitable for this experiment is either radiative recombination or a three-body recombination where a third particle carries off the resulting binding energy [54]. The radiative process

$$\overline{p} + e^+ \rightarrow \overline{H} + \hbar\nu \tag{3.1}$$
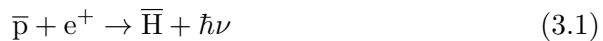
where the liberated binding energy is radiated via a photon is, however, more than one order of magnitude less efficient in the experimental setup under consideration than the three-body recombination. Thus, the three-body process

$$\overline{p} + e^+ + e^+ \rightarrow \overline{H} + e^+ \tag{3.2}$$

where the second positron absorbs the binding energy is the dominant production channel for antihydrogen. For a more detailed treatment of the different production processes, the reader is referred to [14, 55].

The experimental implementation of antihydrogen synthesis is described in more detail in [19]. Here only a brief overview will be given.

With an initial energy of $100\,\mathrm{eV}$, the positrons are injected into the cusp trap[8] and captured in a special potential geometry (Φ_2 in Fig. 3.9). They are cooled to $150\,\mathrm{K}$ and compressed to a density of roughly 10^8 particles per square centimeter. The potential is slowly changed (Φ_1 in Fig. 3.9),

---

[8]Note that the cusp trap is not located in the center of the cusp field. There the magnetic field is zero and hence no cooling is possible. In fact it is located at the left spindle region (far left side of Fig. 3.8) where a nearly homogeneous field is present.

Figure 3.9: *Potentials used to capture positrons and antiprotons for antihydrogen formation inside the cusp trap. The injected positrons are captured by potential Φ_2. They are compressed and cooled and the potent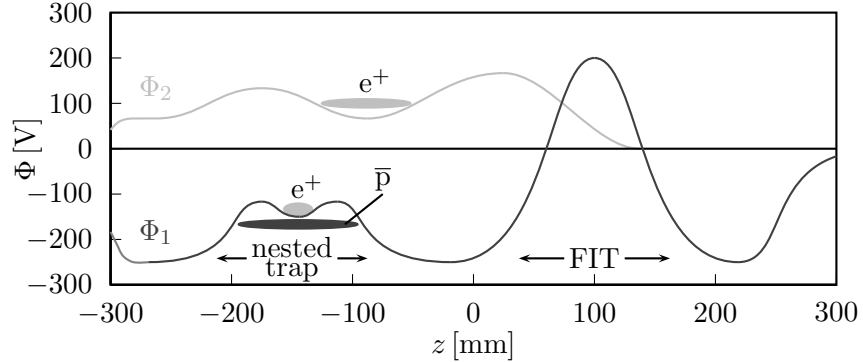ial is slowly changed to Φ_1. Once they are well confined inside their well, the antiprotons are injected on the other side of Φ_1 and the mixing process starts. (Picture adapted from [47])*

making the potential well for the positrons shallower and shallower. Once they are well confined at the final position of the well, the antiprotons are injected with an energy of $100 - 250\,\text{eV}$. They are caught on the opposite side of the positron potential, causing the positrons to heat up[9]. Once they start cooling again, the mixing process starts. Since the efficiency[10] of the mixing process depends on the positron density and temperature [56], it proved to be favorable to have an order of magnitude more positrons than antiprotons inside the trap (a few 10^6 positrons compared to several 10^5 antiprotons). The produced neutral antihydrogen atoms are not confined inside the trap and drift outwards isotropically. A part of them is collected in the field ionization trap (FIT) region (Fig. 3.9) and, depending on the state of the atoms, re-ionized. The FIT is in principle an electrical field of adjustable strength that can be passed only by atoms in a specific state ($n < 40$) — all others are ionized. The field strength of the FIT thus determines the principle quantum number of the produced antihydrogen atoms. Hence, by adjusting the FIT to the corresponding value, only antihydrogen atoms in lower states can pass without being stripped of their positron. This, together with the high field gradient, ensures that predominantly low field seeker states of ground-state antihydrogen leave the trap.

---

[9]Since the positrons can be re-cooled more easily by synchrotron radiation, their initial injection is preferable.

[10]The best efficiency of antihydrogen production achieved so far with the presented method was 7% in 2011.

3.2.3 The Detector

As a detector, a multi channel plate (MCP) [57] is currently in use. The plate is surrounded by a scintillation detector covering the full azimuthal angle. When an antihydrogen atom hits the MCP, the decay signature of its antiproton consisting mainly of pions (Fig. 3.10) is detected and the decay vertex can be reconstructed.
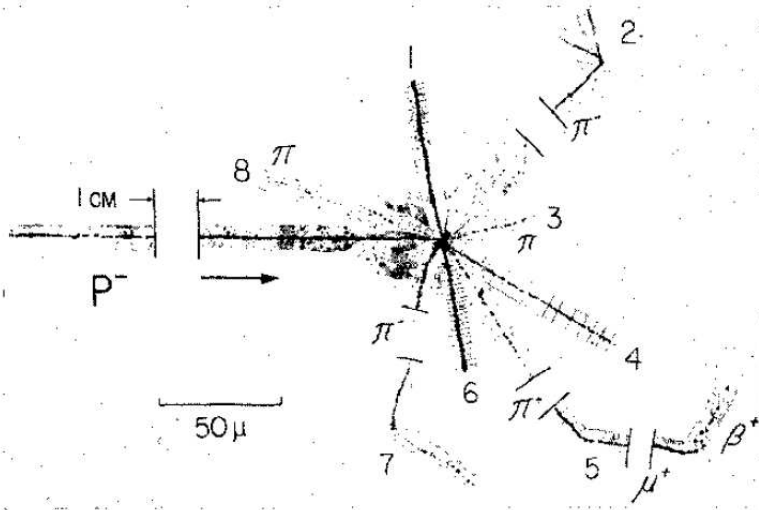
FIG. 7. An annihilation star (36) showing the particles as numbered.

No.	1	2	3	4	5	6	7	8
Identity	p?	π^-	π?	p	π^+	H^a(?)	π^-	π
T (Mev)	10	43	175	70	30	82	34	125

Total visible energy 1300 Mev. Total energy release >1400 Mev.

Figure 3.10: *Example for an anihilation signature of an antiproton. The main secondary particles created are pions. (Picture taken from [58])*

However, the usage of the position sensitive MCP proved to be not ideal. Its sensitivity for low energy particles and electrons leads to a dependence of the background rate on the position of the thermal shield at the cusp trap exit. Furthermore, the dimension of the detector is quite large, since it has not only to detect LFS atoms near the center, but also the HFS atoms further outside. As a consequence, the surrounding scintillation detectors have to be large in diameter thus reducing the covered solid angle. In addition, the best vacuum achieved inside the detector module was only a few 10^{-9} mbar. Therefore, other solutions for detection of the antihydrogen beam are currently investigated.

Chapter 4

The Spin-Flip Cavity

Spin-flip transitions between the hyperfine structure levels of antihydrogen can be induced by a microwave field oscillating at the corresponding frequency. This field is generated by a dedicated cavity, providing not only the desired frequency at resonance but also the possibility to tune it over a bandwidth of 6 MHz. The design and implementation of this cavity is the central topic of this thesis.

The resonating cavity will be described in detail in the following starting with the design requirements and an overview of the considered geometries. Subsequently the final design and the technical implementation including mechanical and vacuum aspects as well as RF aspects, are presented. Furthermore, the design and implementation of the circuits used during operation as well as for testing of the structure will be discussed. Measurement results of the electromagnetic properties of the cavity as well as their comparison with simulation results conclude this chapter.

4.1 Design Requirements

Due to its dependency on magnetic fields (see Section 2.2), the detected resonance width is sensitive to inhomogeneities of the applied magnetic fields. Hence, it is crucial to have an excellent homogeneity (inhomogeneity less than 10% as determined by simulations [59]) of the radio frequency field over the whole beam aperture which is 100 mm in diameter in the present case. In addition, the resonance width is also influenced by the field geometry. Thus, a field without any components in beam direction is favorable, since a broadening due to Doppler shifts can be avoided this way [46].

The resonance frequency of the cavity should be at 1.42 GHz (see Section 2.2) and it should be designed such that it is capable of providing a tuning range of 6 MHz to enable a frequency scanning[1]. This sets the upper limit

---

[1] The frequency bandwidth is with 6 MHz dimensioned such as to allow the measurement of two hyperfine transitions: the σ_1 and the π_1 transition (Fig. 2.3). The latter is

of the quality factor Q^2 of the cavity to ≈ 240.

The maximum amplitude of the microwave field should be $0.01\,\text{G}^3$ to avoid large shifts of the resonance frequency [60]. All these design requirements are summarized in Table 4.1.

Table 4.1: *Summary of the necessary design requirements for the spin-flip cavity.*

field inhomogeneity $\mathcal{I}$	$\leq 10\%$
resonance frequency f_{res}	$1.42\,\text{GHz}$
tuning range Δf	$6\,\text{MHz}$
quality factor Q	≤ 240
maximum field amplitude	$0.01\,\text{G}$

To fulfill these requirements, different cavity geometries have been considered. They are presented in the following Section.

4.2   Considered Geometries

As a first step, it has to be determined whether the implementation of a standing or a traveling wave structure[4] is preferable. For the present geometry where the size of the beam aperture is in the range of the wavelength, fringe field effects become important for traveling wave structures. This makes them impractical for the intended purpose. Hence, the implementation of a standing wave structure has been chosen as a basis for the cavity design.

According to simulations [59], such a standing wave structure leads to a double dip (Fig. 3.4) in the resonance curve for a structure with one field maximum along the beam axis. Each additional field maximum inside the cavity would lead to an extra dip in the resonance[5], making it more difficult to resolve. Therefore only $\lambda/2$ structures have been considered in the following[6].

---

shifted by nearly $6\,\text{MHz}$ if an external field of $1\,\text{G}$ is present.

[2]The quality factor of the cavity is the ratio of the resonance frequency and its $3\,\text{dB}$ bandwidth $Q = \frac{f_{\text{res}}}{\Delta f_{\text{3dB}}}$.

[3]This value can be calculated using formulas given in [46] and assuming a Maxwell-Boltzmann distribution for the particle velocity with a temperature of $50\,\text{K}$. This corresponds to an average particle velocity of $1000\,\text{m/s}$.

[4]To avoid Doppler shifts, the direction of the traveling wave should be perpendicular to the beam.

[5]This is due to the sinusoidal field geometry in beam direction of the standing wave structure where a spin-flip in the first half of a maximum and another spin-flip in its second half is induced. A frequency deviation from the resonance frequency causes an asymmetry of these spin-flips and hence a change in the count rate.

[6]All simulations conducted in the context of this thesis were done using CST Studio Suite 2009 – 2012. For the simulations in this chapter the sub-package Microwave Studio

4.2.1 Rectangular and Pillbox Cavities

As shown in [61], simple rectangular or cylindrical (Pillbox) cavities only provide the necessary field condition in their center. They do not deliver a purely transverse field over the whole aperture and hence are not suitable for the present application.

4.2.2 Magnetic Walls

The concept of magnetic walls has been investigated, which, theoretically, would pose an ideal solution since they provide a purely transverse and homogeneous field throughout the cavity. However, the implementation of this concept is not straight forward. In addition to the printed circuit approach stated in [61], the implementation of corrugated surfaces [62] and photonic band-gap structures [63] as cavity walls have been investigated in the context of this thesis. It was found that the functionality of this approach is dependent on the correct angle of the incident wave onto the surface. Since this could not be implemented in the investigated case, the concept is not suitable for the present application.

4.2.3 Crab Cavities

As an upgrade for the large hadron collider (Lhc), cavities that deflect the beam transversely at the collision point to increase the collision rate, are currently under investigation at Cern — these structures are referred to as crab cavities. Inspired by the designs studied in this context, two such structures have been investigated concerning their suitability in the context of this thesis. They will be presented in the following.

Double Ridge Cavity

In this design [64], a double ridge waveguide of a given length is converted into a resonator (Fig. 4.1). Such a configuration provides a purely transverse field but delivers a field inhomogeneity larger than 10% in the volume of interest. It is thus not suitable for the desired application.

Parallel Bar Design

This structure essentially consists of a resonator housing two parallel resonant rods (Fig. 4.2) of opposite phase [65]. However, it was found that this configuration does not provide a purely transverse field over the whole aperture and hence is not suitable for the present application.

---

has been used.

(a)   (b)
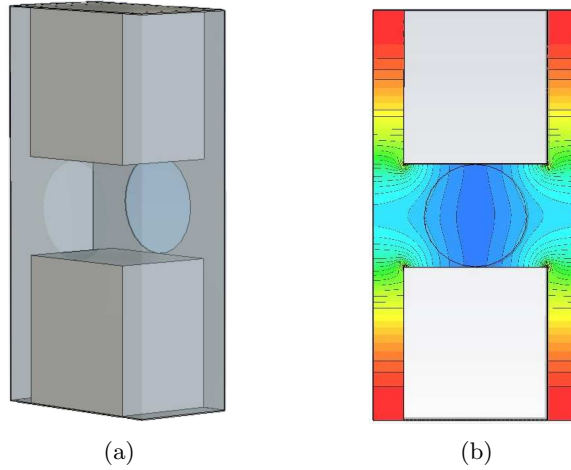
Figure 4.1: *(Color) (a) The double ridge structure as used in simulation studies. It does provide a purely transverse field but the field homogeneity is too low for the present application. (b) The magnetic field distribution for the double ridge geometry. The colors are a qualitative illustration of the field homogeneity. The highest field strength is indicated in red, the lowest field strength in blue. The circle in the center corresponds to the beam aperture which is 100 mm in diameter.*

(a)   (b)
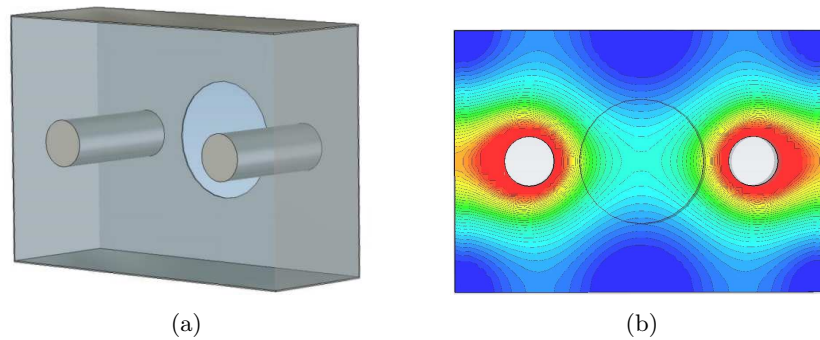
Figure 4.2: *(Color) (a) The parallel bar design as used for simulations. Since it does not provide a purely transverse field, it is unsuitable for the desired purpose. (b) Distribution of the magnetic field for the parallel bar structure. The colors are a qualitative illustration of the field homogeneity. The highest field strength is indicated in red, the lowest field strength in blue. The circle in the center corresponds to the beam aperture which is 100 mm in diameter.*

4.2.4 Strip-Line Resonator

A simple strip-line resonator as already suggested in [61] (Fig. 4.3) proved
to be the best solution for the present application. It is capable of providing

(a)   (b)
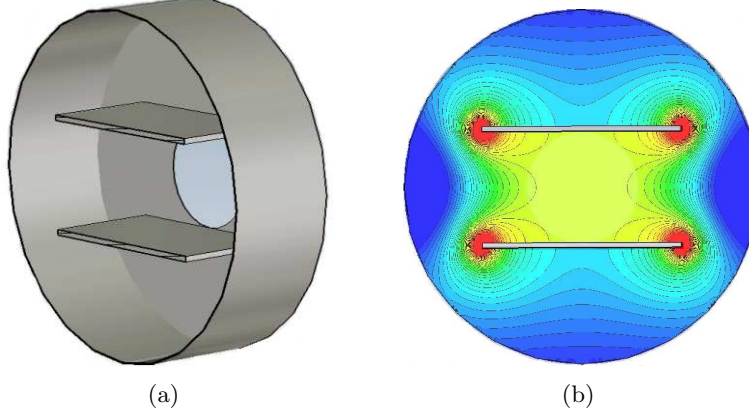
Figure 4.3: *(Color) (a) Schematic picture of the strip-line resonator that
proved to provide all the necessary requirements and thus was chosen as final
design. (b) Magnetic field configuration of the strip-line cavity. The colors are
a qualitative illustration of the field homogeneity. The highest field strength is
indicated in red, the lowest field strength in blue. The circle in the center corre-
sponds to the beam aperture which is 100 mm in diameter.*

a field with an inhomogeneity of 3% (Fig. 4.4 (a)) which is well below spec-
ifications. The field is purely transverse[7] to the beam and has a sinosoidal
gradient in beam direction (Fig. 4.4 (b)). The drawback is that in this

(a)   (b)
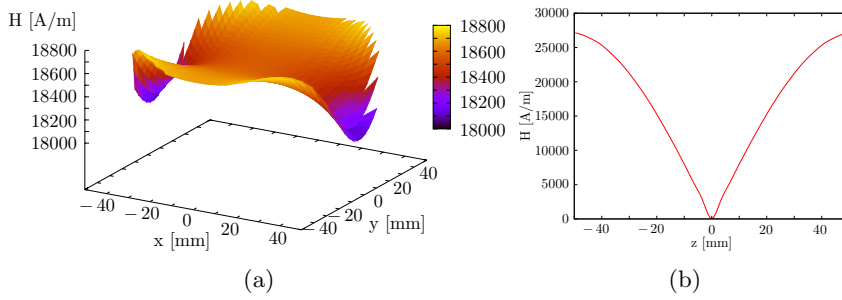
Figure 4.4: *(Color) (a) Field homogeneity over the beam aperture as deter-
mined by simulations. (b) The slope of the magnetic field (absolute value) in
beam direction. For both cases, the amplitude of the oscillating field is plotted.*

geometry, two different modes, an even and an odd mode (Fig. 4.5) exist os-
cillating at nearly the same frequency. The unwanted mode can be detuned
by using small metal plates in between the strip-lines, so called wings (Fig.

---

[7]Since the magnetic field lines inside the cavity close around the strip-lines, no field
components in beam direction are present.

(a)   (b)
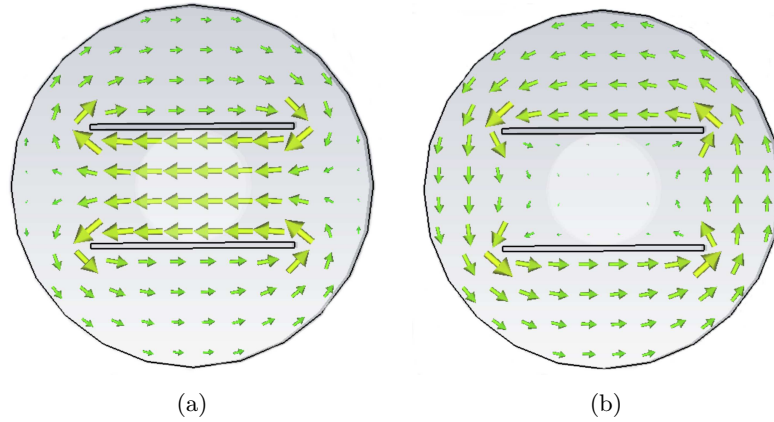
Figure 4.5: *(Color) The magnetic field distribution of the desired odd (a) and the undesired even mode (b). The circle in the center corresponds to the beam aperture which is 100 mm in diameter.*

4.13). These effect the even mode only [61] leading to a frequency shift of 60 MHz and thus rendering the structure the suitable choice for the present application.

All dimensions of the final design as determined from simulations are summarized in Table 4.2. The mechanical implementation of the structure will be presented in the following.

Table 4.2: *Summary of the dimensions of the strip-line cavity as implemented. Short of the material thickness, all values have been chosen as suggested in [61].*

diameter of the cavity tank	320.0 mm
cavity length	105.5 mm
strip-line width	180.0 mm
strip-line length	105.5 mm
strip-line thickness	4.0 mm
wing length	53.0 mm
wing width	36.0 mm
wing thickness	4.0 mm

4.3   Technical Implementation

4.3.1   Determination of Tolerances

For the implementation of the final cavity design it is important to know how deviations from the ideal configuration will influence the field geometry and homogeneity inside the region of interest since the manufacturing of the pieces cannot be done with unlimited precision. For the final configuration,

the position of the strip-lines as well as the cavity length are of great impor-
tance since the former has a considerable influence on the field homogeneity
and the latter is relevant for the resonance frequency. The dimensions of
the wings are not critical, since they only have a significant effect on the
unwanted mode.

For the position of the strip-lines, four different cases have been investi-
gated via simulation:

- variation of the strip-line distance (Fig. 4.6(a))

- lateral displacement of the strip-lines with respect to each other (Fig.
  4.6(b))

- tilt of the strip-lines perpendicular to the beam axis (Fig. 4.6(c))

- tilt of the strip-lines along the beam axis (Fig. 4.6(d))

    (a)   (b)   (c)   (d)
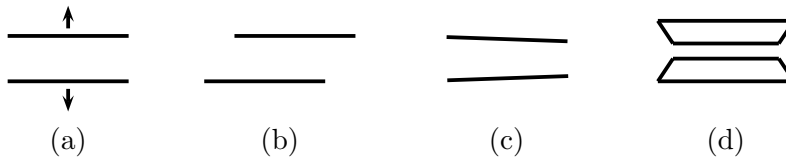
Figure 4.6: *Graphical illustration of the investigated deviations from the ideal
strip-line position. These are comprising a variation of the strip-line distance
(a), their lateral displacement (b), and a tilt perpendicular (c) and parallel to
the beam axis (d). For each case the beam axis is perpendicular to the paper
plane.*

These studies showed, that the field geometry and homogeneity is not very
sensitive to these deviations The variation of the distance between the strip-
lines revealed, that an increase of $10\,\text{mm}$ caused a field inhomogeneity of
only 5.5% (Fig. 4.7 (a)). Since a tolerance in the order of centimeters is also
well above practical limits for manufacturing precision, this deviation is not
critical. Moving the plates with respect to each other for $10\,\text{mm}$ proved to be
uncritical as well since it resulted in an inhomogeneity of 5% which is again
well within specifications (Fig. 4.7 (b)). Tilting the strip-lines either along
or perpendicular to the beam showed that only from a tilt of 4° onwards
it leads to the inhomogeneity limit of 10% (Fig. 4.7 (c),4.7 (d)). Therefore
it was concluded that the standard medium tolerances of $\pm\,100\,\mu\text{m}$ were
applicable for manufacturing.

However, the length of the cavity is more sensitive to deviations since it
directly determines the resonance frequency. Thus, a deviation of the cavity
length by $1\,\text{mm}$ already leads to a frequency shift of $13\,\text{MHz}$. This exceeds
the tuning range by more than a factor two and cannot be compensated
easily. Therefore, this parameter was specified with an accuracy of $\pm\,50\,\mu\text{m}$.
A deviation of this range leads to a frequency shift of $\pm\,1\,\text{MHz}$ which is well
within the tuning bandwidth and hence can be compensated.
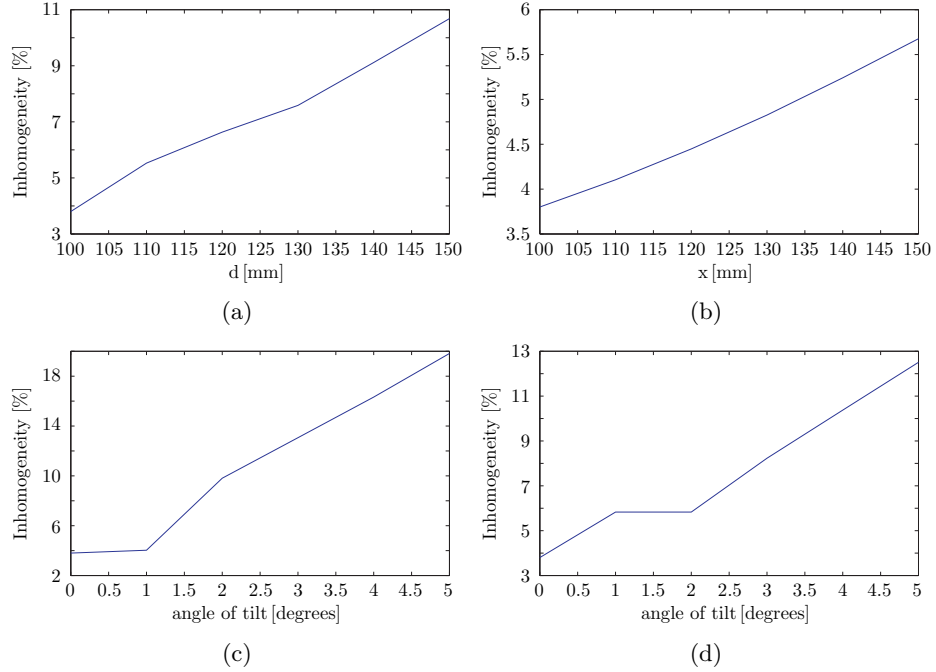
Figure 4.7: *(Color) (a) The field homogeneity as a function of the strip-line distance d. (b) The development of the field homogeneity as a function of the lateral displacement of the strip-line electrodes. (c) Effect on the field homogeneity of a misalignment of the strip-line electrodes perpendicular to the beam. (d) Development of the field homogeneity with strip-line electrodes tilted along the beam axis.*

4.3.2   Mechanical Aspects

In order to not disturb the present magnetic field and thus increasing its inhomogeneity, the whole cavity is made of non-magnetic material. All main components such as the cavity body, the strip-lines the wings and tubes connecting flanges were made of 316L/316LN stainless steel. Also all necessary screws and bolts were specified as non-magnetic[8].

A main objective of the mechanical implementation was to design the whole cavity to be completely dismountable. Thus, if necessary every part can be exchanged without affecting the whole cavity structure. Furthermore, it was chosen to use commercially available vacuum components as far as possible to facilitate the purchase of spare parts and accessories such as copper gaskets. Consequently, for the cavity, four 16 1/2" OD CF flanges —

---

[8]However, it turned out in the course of this work that several screws showed slight remanecent magneticity. Therefore, these screws were tested to determine their exact magnetic properties. The screws were inserted into a very homogeneous magnetic field (center of a large dipole field) and their effect on the field was measured. It was found that they disturb the magnetic field only by roughly 0.005% [66] which is acceptable.

two blind flanges and two adapter flanges (zero length reducers, Fig. 4.8 (a))
providing the transition from the cavity to the vacuum chamber of the beam
line (100 mm diameter - CF 100 flange) — were used to form the tank (Fig.
4.9). Into the blind flanges, holes of the cavity diameter were drilled and

(a)   (b)
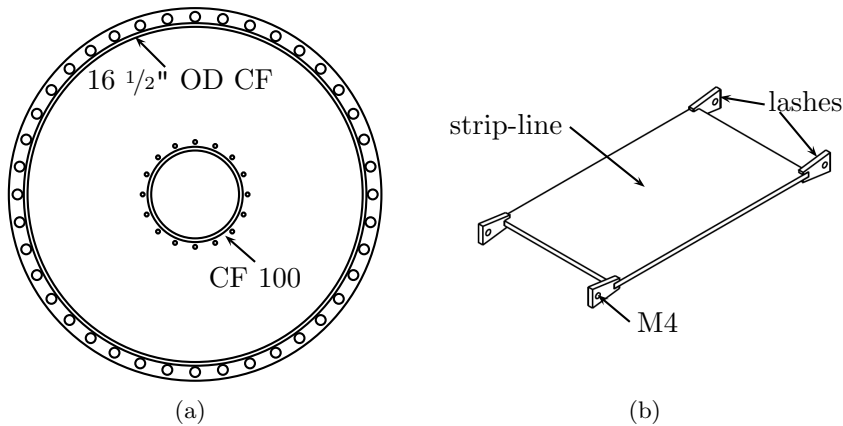
Figure 4.8: *(a) Schematic drawing of a zero length reducer from 16 ¹/₂" OD
CF (outermost edge) to CF 100 (inner circle). Two such pieces were used to
close the cavity. (b) Schematic drawing of the strip lines including the lashes
for fixation.*

a stainless steel sheet was welded onto them forming the cavity body. The
zero length reducers are used to cover the entrance and exit of the cavity as
well as to hold the strip-lines in position.

The strip-line electrodes were extended with four lashes equipped with
holes to accommodate size M4 screws or bolts (Fig. 4.8 (b)). To ensure
good electrical contact, contact-spring strips (supplier: Feuerherdt [67]) were
placed between the cavity wall and the strip-line electrodes (Fig. 4.10). For
these Rf contacts, a copper beryllium alloy, CuBe2 was used. This material
was chosen for its elasticity and good conductivity. This way good electri-
cal contacts are provided that were even further improved by gold plating.
However, after baking for three times, it was observed, that the material
starts to loose its elasticity, leading to a slight worsening of the contact.
Therefore, the implementation of new contacts for each experimental run is
recommended. As an alternative, CuBe10 could be used which has a higher
thermal stability [68]. However, manufacturing of the required spring con-
tacts is much more involved and costly, therefore the use of the commercially
available CuBe2 contacts is favorable.

The wings were fixed at three points to the cavity body via point welding.
Thus, good contact is ensured while providing easy removal using only light
force.

To ensure comfortable assembly of the cavity, the strip-lines are screwed
onto the bottom zero length reducer only. On the top zero length reducer
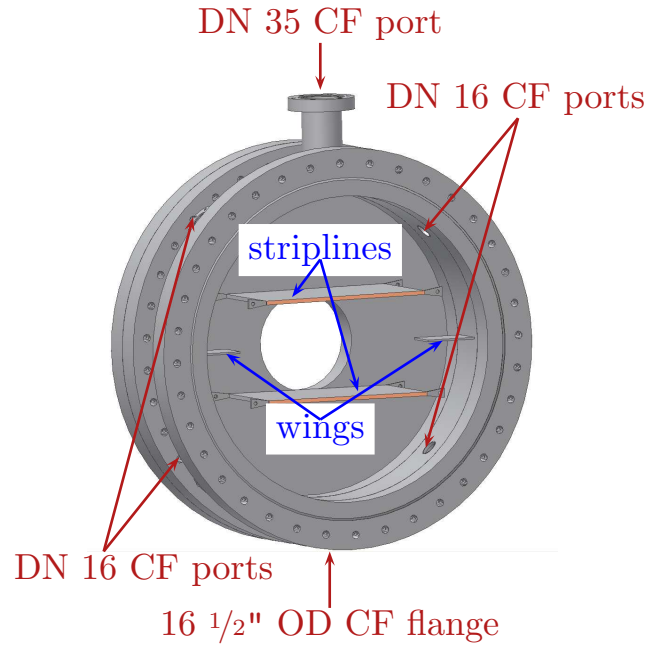
Figure 4.9: *(Color) The final cavity design as done with Autodesk Inventor to obtain a technical drawing. As far as possible, standard vacuum components have been used to implement the strip-line resonator. This ensures the availability of spare parts and accessories such as copper vacuum seals.*

(a)

(b)
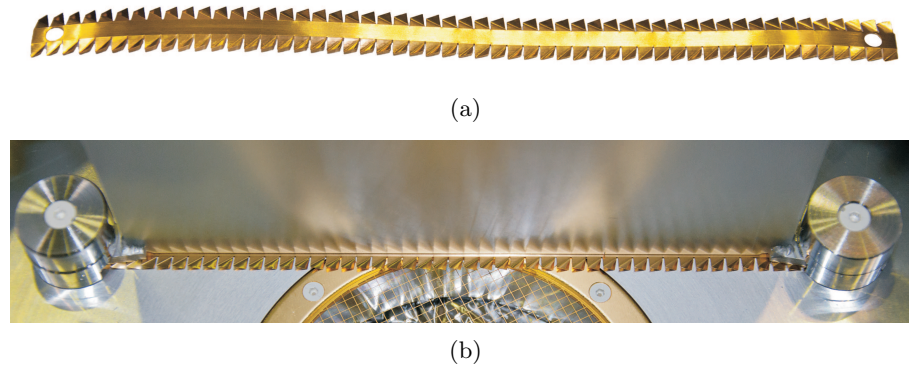
Figure 4.10: *(Color) (a) The special gold plated copper beryllium (CuBe2) contact-spring strips that are used to ensure a good electrical contact between the strip-lines and the cavity wall. (b) They are mounted together with the strip-lines and fixed with the same screw.*

specially manufactured bolts with a conical tip are mounted. These slide into the remaining holes on the other side of the strip lines when closing the cavity.

4.3.3 Vacuum Aspects

Experiments with antimatter, especially with precious antihydrogen, require an excellent vacuum ($\leq 10^{-9}$ mbar) to minimize annihilation. This can only be achieved if the whole structure is bakeable up to at least $150\,°C$ to efficiently reduce the amount of water vapor. In addition, only components with a low out-gassing rate were used inside the cavity. To reduce the amount of out-gassing hydrogen, the zero length reducers, the cavity body (including the wings) and the strip-lines were vacuum fired at $950\,°C$ for several hours. This procedure released the hydrogen that was enclosed inside the metal during the production process.

Also all screws and bolts inside the cavity are either drilled through or scored allowing to evacuate the small volume behind them when they are fixed. Furthermore, all screws were silver plated, to avoid cold welding which can occur under pressure.

4.3.4 Radio Frequency Aspects

Since the beam aperture is quite large, a suitable cover at the cavity entrance and exit has to be implemented in order to prevent the microwave from leaking out of the resonator volume which would distort the mode geometry. This can be done using meshes (supplier: CERN TE-MPE-EM group) to cover the entrance and exit of the cavity (Fig. 4.11) [69]. These are dimensioned such[9] as to have a transparency of 96% for the antihydrogen atoms while ensuring a perfectly closed resonator for the microwave. Included in the center of the meshes is a solid area (40 mm diameter), providing a beam stop for atoms arriving at the center. This is essential, since the atoms passing in this region are not or only little deflected in the sextupole magnet due to its field geometry (no field present on axis) and thus indistinguishable from the ones focused on the detector. The meshes are fixed using specially modified CF 100 copper gaskets. These gaskets were drilled with 20 holes to accomodate M3 screws. Each mesh is put in between two gaskets and screwed onto the zero length reducers at the top and bottom of the cavity.

In order to couple the microwave into the cavity, special feedthroughs that are mechanically stable and suitable for UHV are needed. The commercial available feedthrough solution from PMB [70] proved to be the best

---

[9]The meshes are manufactured from a $100\,\mu$m thick sheet of stainless steel into which the desired structure is edged chemically. The diameter of a wire inside the mesh structure is $100\,\mu$m. This is the minimum diameter that still ensures mechanical stability of the mesh structure. The gap between the wires was chosen to be $5\,$mm. The mesh is gold plated to improve its conductivity.

1 cm
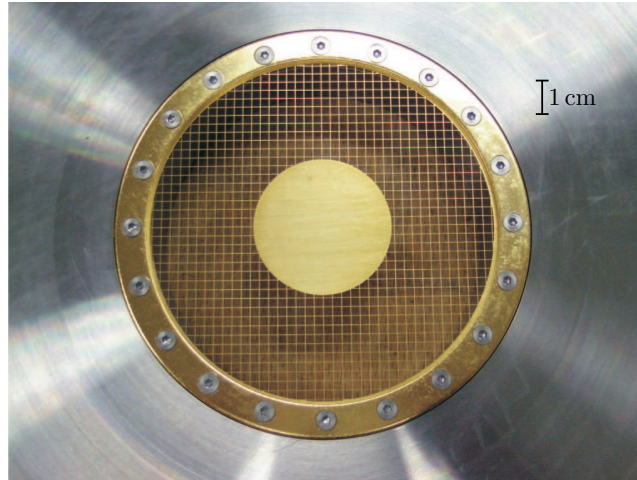
Figure 4.11: *(Color) The mesh used to cover the entrance and exit of the cavity. It is nearly transparent for the impinging antihydrogen atoms (96% transparency) but closes the resonator almost perfectly for the microwave. The beam stopper implanted in the middle is clearly visible. It blocks the antihydrogen atoms in the center, since due to the field geometry of the sextupole, these would either be not deflected at all or the deflection would be too small to distinguish them from the undeflected atoms. Each mesh is planted between two custom made gold plated copper gaskets and fixed with 20 M3 screws.*

suited. The feedthroughs were equipped with stainless steel antennas to efficiently couple the microwave into the cavity (Fig. 4.12).

In total, four feedthroughs were used — two to couple in the microwave in order to excite the desired odd mode selectively and two to pick up the microwave for on-line diagnostic (see Section 4.4).

4.3.5   The Spin-Flip Cavity

The assembled design is depicted in Fig. 4.13. In addition to the four large 16 $1/2$" OD CF flanges it consists four CF 16 flanges equipped with feedthroughs and antennas and one CF 35 flange that can be equipped with additional vacuum pumps if needed. As can be seen from Fig. 4.13 a consequence of using standard flanges is the unavoidable gap that is formed by the vacuum seal of the 16 $1/2$" OD CF end flanges, on the outer rim of the structure, and the edge of the cavity body. The propagation of the microwave into this gap would cause a mode distortion[10] and hence it is necessary to close it. This was done using custom made spring contact rings (Fig. 4.13). As the other contact springs used inside the cavity, these were made of gold coated CuBe2.

---

[10]Since the gap has a width of about 5 cm it would act as a $\lambda/4$ transformer, causing a considerable distortion of the propagating modes.

1 cm

Figure 4.12: *(Color) Example of a feedthrough equipped with an antenna. Four such devices are used around the cavity: Two to couple the RF power into the cavity and two to pick up the signal. This allows selective excitement of the wanted mode as well as monitoring the mode pattern inside the cavity.*

DN 35 CF port

DN 16 CF ports

DN 16 CF ports

gap

strip-lines

wings

contact
spring ring
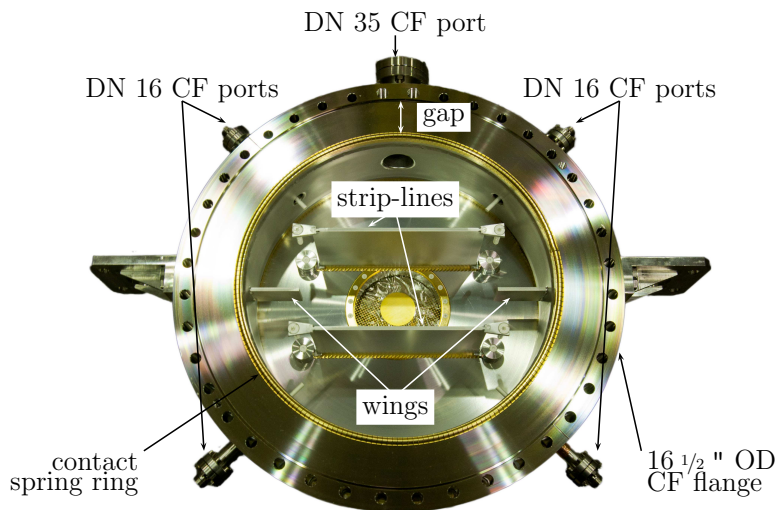
16 $^1/_2$ " OD
CF flange

Figure 4.13: *(Color) The final cavity design as mechanically implemented. The cavity consists of a bottom and a top part (not shown here) which is a zero length reducer from a 16 $^1/_2$ " OD CF flange to a CF 100. The tank is welded onto two custom made 16 $^1/_2$ " OD CF flanges. It has four CF 16 flanges to equip the feedthroughs and one CF 35 flange that can be equipped with additional vacuum pumps if needed. The striplines, meshes and wings are clearly visible as well as the spring contact ring to close the cavity RF wise to the right size.*

4.4   Circuit Design and Implementation

To facilitate the excitation of the wanted mode, two antennas on opposite
sides are used to couple the microwave into the cavity. The other two are
used as a signal pick up. For the powering of the cavity as well as the moni-
toring of the excited mode and power inside during the experimental run, a
circuit as depicted in Fig. 4.14 (a) is used. After amplification[11] (amplifier:
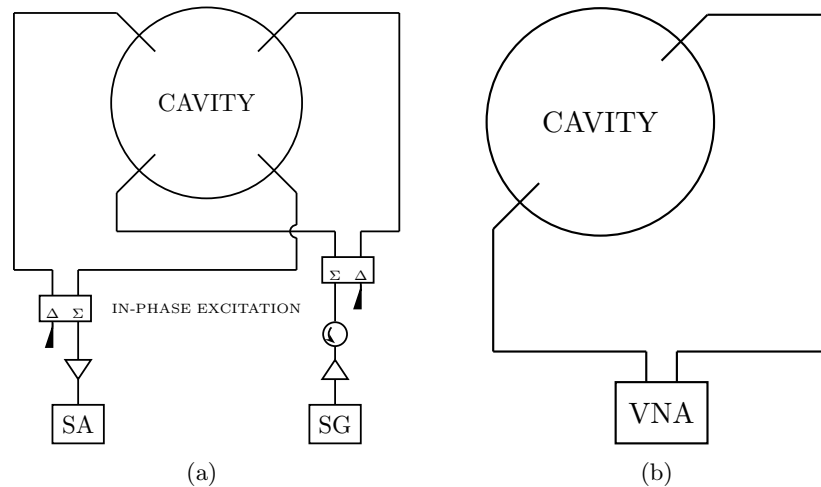
Figure 4.14: *(a) The circuit as implemented for experimental operation. The
signal from the signal generator (SG) is amplified, split by a 180° hybrid and
used for an in-phase excitation. For monitoring, a similar configuration is used
to guide the signal to a spectrum analyzer (SA), where the power and frequency
inside the cavity are displayed. (b) The circuit as used for RF testing. A vector
network analyzer (VNA) was used to investigate the transmission properties of
the cavity.*

Mini-Circuits ZHL-10W-2G(+)) of the signal from the frequency generator
(Rohde & Schwarz Signal Generator SML 02), a 180° hybrid (Pulsar Mi-
crowave Corporation [71]) is used to split the signal and feed it in phase to
both antennas. The necessary input power for different field amplitudes can
be found in Section 4.5.2.

For monitoring, the signal from the cavity is recombined by an identical
hybrid and after amplification fed to a spectrum analyzer (Agilent Technolo-
gies EXA Signal Analyzer N9010A). Since the visible peak is proportional
to the power in the setup, this can be monitored as well along with the
operating frequency. Alternatively, the two antennas for monitoring can be

---

[11]To be able to work off resonance the available input power into the cavity was deter-
mined to be 10 W. This includes a large safety margin since the operation at resonance is
in the order of several mW (see Section 4.5.2).
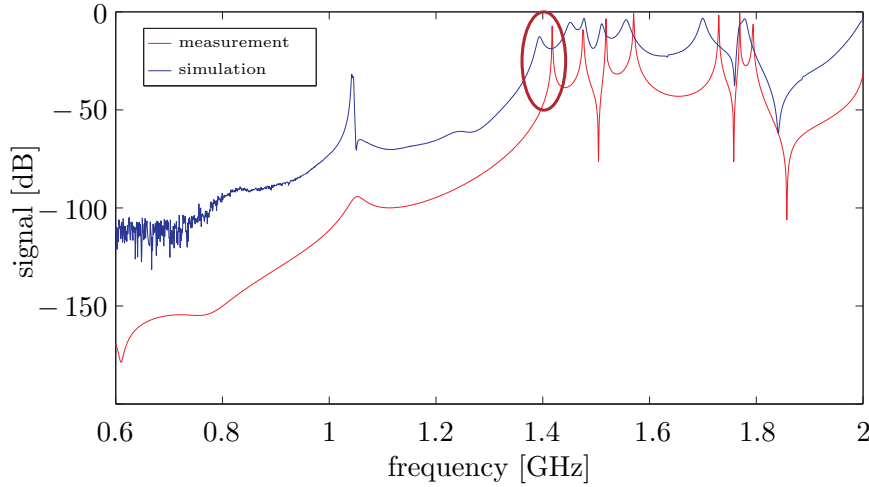
Figure 4.15: *(Color) Comparison of the simulated and measured transmission pattern for the implemented cavity. A good agreement can be seen. However, the frequency of the wanted mode is detuned by 26 MHz which made fine-tuning of the structure necessary.*

connected to a vector network analyzer, enabling the control of the whole mode spectrum inside the cavity.

To test the electromagnetic properties of the cavity, it is sufficient to use a vector network analyzer (VNA) which allows excitation and monitoring at the same time (Fig. 4.14 (b)). Measurement results obtained with this setup are given below.

4.5 Measurements

In this section the results of the RF tests of the implemented structure as well as the necessary tuning are presented and compared to simulation results. In addition, results of the first vacuum tests are presented as well.

4.5.1 Radio Frequency Tests

Tests without the circular spring contact rings showed a distortion of the propagating modes as expected. Insertion of the rings lead to a good agreement between the simulated and measured RF pattern (Fig. 4.15). Nevertheless, the resonance frequency of the structure was found to be off by 26 MHz, which made a suitable tuning necessary

In a first step, the RF antenna length was optimized to achieve the most efficient coupling of the microwave into the cavity. Several antenna lengths were tried and a considerable effect of the antenna length not only on the coupling but also on the resonance frequency was observed. The results of this study are summarized in Table 4.3. The optimal antenna length

Table 4.3: *Reflection coefficient (S_{11}), which the ratio between the reflected and incident signal at the cavity input(see Appendix C), and resonance frequency (F_{res}) of the desired working mode for different antenna lengths (L_a).*

L_a [mm]	S_{11} [dB]	F_{res} [GHz]
11	−2.2	1.404
11.5	−5.3	1.403
12	−26.5	1.402
12.5	−5.9	1.401
13	−2.4	1.394

was determined to be 12 mm, causing an increase in resonance frequency of 8 MHz.

The remaining shift of 18 MHz was compensated using small stainless steel discs (Fig. 4.16). These were put at each strip-line end and fixed together with them. According to simulations, the discs have no influence on the field geometry in the region of interest. Eight tuning discs of 10 mm
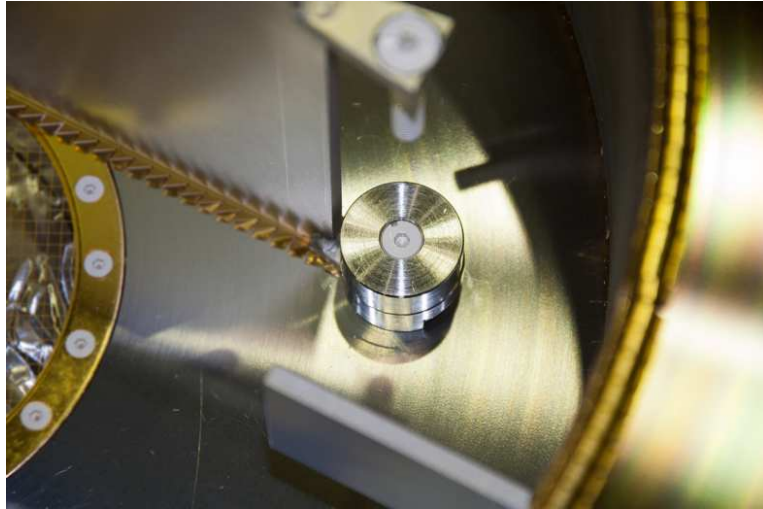
Figure 4.16: *(Color) Small metal discs used to tune the cavity to the desired frequency. In total eight such discs have been used.*

length and 25 mm diameter were sufficient to obtain a resonance frequency of 1.420 GHz as required (Fig. 4.17).

The measured Q value of the cavity was roughly 300, allowing for a frequency tuning range within the 3 dB bandwidth of about 5 MHz. Since an amplifier with a gain of 40 dB is used, the desired tuning range of 6 MHz can be provided easily.
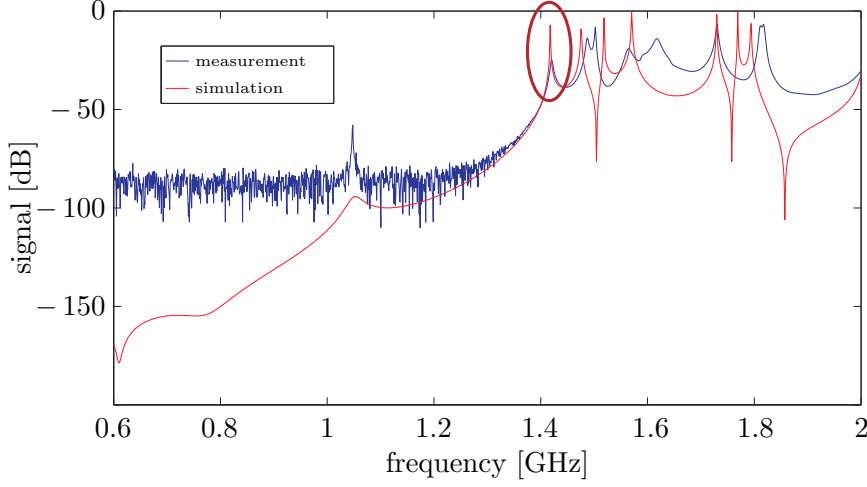
Figure 4.17: *(color) Comparison between the simulated and measured transmission versus frequency for the tuned spin-flip cavity. The good agreement between both as well as the achievement of the required resonance frequency is clearly visible.*

4.5.2 Field Amplitude versus Input Power

For the operation of the spin-flip cavity it is of interest to determine the relation between the input power and the field amplitude inside the cavity. To calculate the necessary input power for the different amplitudes, the stored energy inside the cavity for one field amplitude was determined by simulations. It was found that for 1 Joule of stored energy the amplitude of the magnetic field was 340 G.

The input power is related to the energy stored in the cavity via:

$$P = \frac{\omega_{\text{res}} \cdot W}{Q} \tag{4.1}$$

where P corresponds to the input power provided by the external feed, ω_{res} to the resonance frequency of the desired mode inside the cavity, W to the stored power inside the cavity and Q to the quality factor of the cavity. Required input powers for different field amplitudes and different Q values are given in Tables 4.4 – 4.6. In total, three different Q values are considered. A Q of 5000 which was determined by simulations assuming a perfectly closed resonator and perfect electric contacts everywhere. Furthermore, a Q of 300 is considered, which corresponds to the measured Q value with good electrical contacts. Finally, a Q of 140 is used which is in agreement with the measured value for less elastic RF contacts which is the case after four to five baking cycles. A graphical representations of these tables is given in Fig. 4.18.

Table 4.4: *Required input power for different field amplitudes B for a quality factor Q = 5000. This was the quality factor according to simulations assuming perfect electrical contacts throughout the cavity. The middle column corresponds to the calculations of the unperturbed cavity (P_{C}), the last column to the cavity including the disk tuning on one side (P_{TC}).*

B [mG]	P_{C} [mW]	P_{TC} [mW]
1	0.02	0.01
2	0.06	0.06
3	0.14	0.1
4	0.3	0.2
5	0.4	0.35
6	0.6	0.5
7	0.8	0.7
8	1	0.9
9	1.3	1.1
10	1.6	1.4

Table 4.5: *Required input power for different field amplitudes B for a quality factor Q = 300. This is the quality factor as determined by RF tests of the cavity. The middle column corresponds to the calculations of the unperturbed cavity (P_{C}), the last column to the cavity including the disk tuning on one side (P_{TC}).*

B [mG]	P_{C} [mW]	P_{TC} [mW]
1	0.3	0.2
2	1	0.9
3	2.4	2.1
4	4.3	3.7
5	6.7	5.8
6	9.6	8.4
7	13.1	11.4
8	17.1	14.9
9	21.7	18.9
10	26.8	23.3

Table 4.6: *Required input power for different field amplitudes B for a quality factor Q = 140. This quality factor corresponds to a cavity with less elastic RF contacts as is the case after four or five baking cycles. The middle column corresponds to the calculations of the unperturbed cavity (P_{C}), the last column to the cavity including the disk tuning on one side (P_{TC}).*

B [mG]	P_{C} [mW]	P_{TC} [mW]
1	0.57	0.5
2	2.3	2
3	5	4.5
4	9.2	8
5	14.3	12.5
6	20.7	18
7	28.1	24.5
8	36.7	32
9	46.5	40.5
10	57.4	50
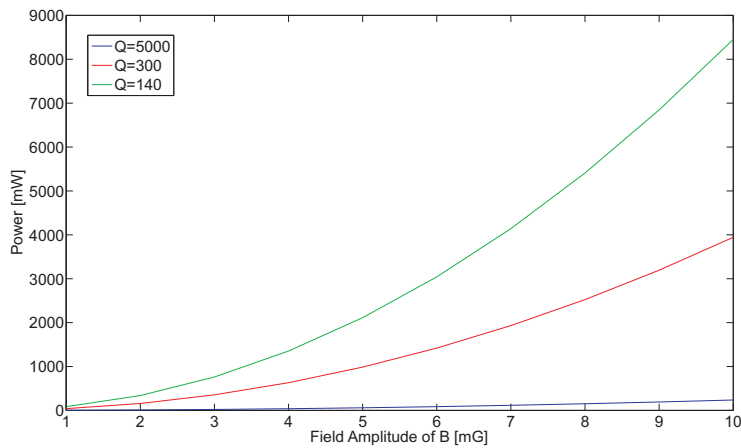
Figure 4.18: *(Color) The amplitude of the magnetic field as a function of input power for three different quality factors.*

4.5.3 Vacuum

To determine the vacuum properties of the cavity, it was pumped through the CF 35 flange. With this configuration it proved to be leak-tight up to $8 \cdot 10^{-10}\,\mathrm{mbar\,l\,s^{-1}}$ (helium standard) and a vacuum of $2 \cdot 10^{-9}\,\mathrm{mbar}$ could be achieved using a TMU 261 P (Pfeiffer) turbo pump. After testing the cavity alone, it was mounted on a support frame together with the sextupole magnet (Fig. 4.19). Both elements were connected and evacuated
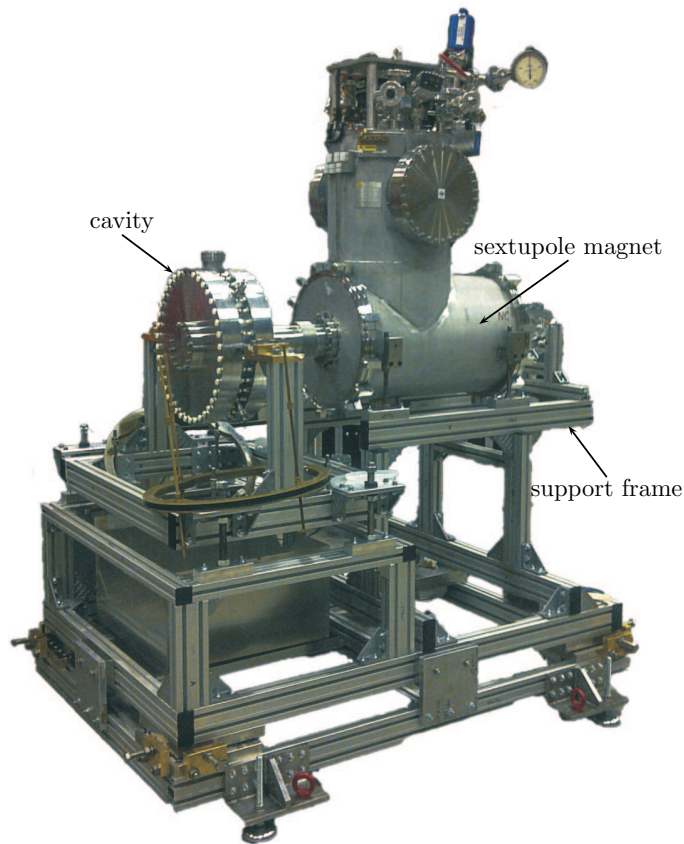
Figure 4.19: *(Color) The spin-flip cavity and the sextupole magnet as prepared for insertion into the spectrometer line.*

with one turbo molecular pump (TMP) which was mounted on the end of the sextupole. Both elements were installed into the setup and baked (cavity up to 170° C). After this treatment, a vacuum of $2 \cdot 10^{-9}\,\mathrm{mbar}$ was achieved which improved to $< 10^{-11}\,\mathrm{mbar}$ with the sextupole magnet cooled down to its operating temperature of $4\,\mathrm{K}$.

It can be concluded that the cavity fulfills the necessary requirements on ultra-high vacuum. Connected to the sextupole magnet, a distinct vacuum pumping system is not needed and hence, the CF 35 flange can be kept blind-flanged during operation.

4.6 First Implementation into the Spectrometer Line

Since the cavity proved to fulfill all necessary requirements in terms of field geometry, resonance frequency and vacuum, it was integrated into the spectrometer line for the first time in 2011. However, due to difficulties in the antihydrogen synthesis inside the cusp trap, no antihydrogen beam for testing of the spin-flip properties of the cavity could be provided.

Chapter 5

Static Magnetic Field

When an antihydrogen atom encounters a transition from a magnetic field into a field free region along its path through the spectrometer, spontaneous spin-flips, so called Majorana spin-flips, can occur [72]. To avoid such field free regions, a static magnetic field is superimposed to the microwave field of the cavity. However, this field influences the transitions inside the antihydrogen atom, resulting in a dependence of the resonance frequencies on the field strength (see Fig. 2.3). In addition, the transitions are (more or less — depending on the transition under investigation) sensitive to inhomogeneities in the magnetic field (see Section 5.1). Hence an excellent shielding is crucial to block perturbations from stray fields caused by the cusp trap on one side of the cavity, the sextupole magnet on the other as well as the AD ring, the crane inside the AD hall, other experiments and the earth magnetic field.

The following chapter will present the implementation of the static field using either one or two pairs of Helmholtz coils. It is opened with considerations on its necessary properties and the required shielding efficiency. Subsequently, simulation studies[1] to determine the best coil geometry including different shielding solutions are discussed. The chapter is concluded with the presentation and evaluation of measurements for the implemented configuration.

5.1   Requirements

5.1.1   Field

As mentioned above, the superposition of a static field onto the oscillating cavity field is required to avoid uncontrolled spin-flips of the antihydrogen atoms. Since only the ground-state hyperfine splitting transition frequency

---

[1]In this chapter the sub-package CST EM Studio has been used for all conducted simulations.

with no external magnetic field present is of interest, two possible approaches
can be considered for the present experimental setup:

- measurement of both, the σ_1 and the π_1 transition (see Section 2.2)

- measurement of the σ_1 transition only

Measuring both transitions would allow determination of the frequency
at zero field by calculating the magnetic field from the $\pi_1((1,-1) \leftrightarrow (0,0))$
transition frequency. This can be done since it has a linear dependence on
the external magnetic field which can be seen easily, when expanding Eq.
2.7 to the second order:

$$\nu[(F,M_1) \leftrightarrow (F,M_2)] = (M_1 - M_2)\frac{g_I\mu_{\mathrm{B}}H}{h} +$$
$$+ \frac{\Delta E_0}{h}\left[1 + \frac{(M_1 + M_2)}{2I+1}x + \left\{\frac{1}{2} - \frac{(M_1^2 + M_2^2)}{(2I+1)}\right\}x^2\right] \quad (5.1)$$

Simulation results show that the measurement of both transitions would
lead to a considerably higher precision — improvement of a factor $5-6$ —
compared with measuring the σ_1 transition only [61]. However, the difficulty
is the sensitivity of the π_1 transition to inhomogeneities[2] of the applied
magnetic fields due to its first order dependence on the field. As can be
seen from Fig. 5.1, an inhomogeneity of more than 0.2% already leads to
a broadening of the resonance curve making it impossible to resolve the
corresponding transition frequency.

The measurement of the $\sigma_1((1,0) \leftrightarrow (0,0))$ transition can be done at
several field strengths ($0.1-3\,\mathrm{G}$ to stay in the far left region of Fig. 2.3
where the dependence of the σ_1 transition is still fairly linear) allowing
extrapolation of the measured resonance frequencies back to zero field. Since
the σ_1 transition has a weaker second order dependence on the external field
(Eq. 5.1), it is less sensitive to inhomogeneities in the magnetic field. As can
be seen from Fig. 5.1, an inhomogeneity between 5 and 10% still allows a
reasonable determination of the resonance. However, for this case an acurate
magnetic sensor, e. g. a Hall probe or flux gate, to measure the field strength
is necessary since the uncertainty of the measurement device enters directly
into the precision of the transition via uncertainty propagation.

So depending on the method chosen, the static field has to fulfill dif-
ferent requirements in terms of field homogeneity. But also its direction
with respect to the microwave field inside the cavity is of importance for the
different transitions. For the σ_1 transition a field parallel to the oscillating

---

[2]The inhomogeneity of the static field leads to a broadening of the resonance curve.
This is the same for the inhomogeneities of the oscillating field inside the cavity. However,
since the field amplitude of the microwave field is two orders of magnitude smaller, this
effect is much smaller [46]. Hence, an inhomogeneity of 10% of the oscillating field is still
sufficient to resolve a resonance for both transitions.

σ_1 transition, $\Delta B/B = 1\%$ π_1 transition, $\Delta B/B = 0.2\%$

σ_1 transition, $\Delta B/B = 2\%$ π_1 transition, $\Delta B/B = 0.5\%$

σ_1 transition, $\Delta B/B = 5\%$ π_1 transition, $\Delta B/B = 1\%$

σ_1 transition, $\Delta B/B = 10\%$ π_1 transition, $\Delta B/B = 2\%$
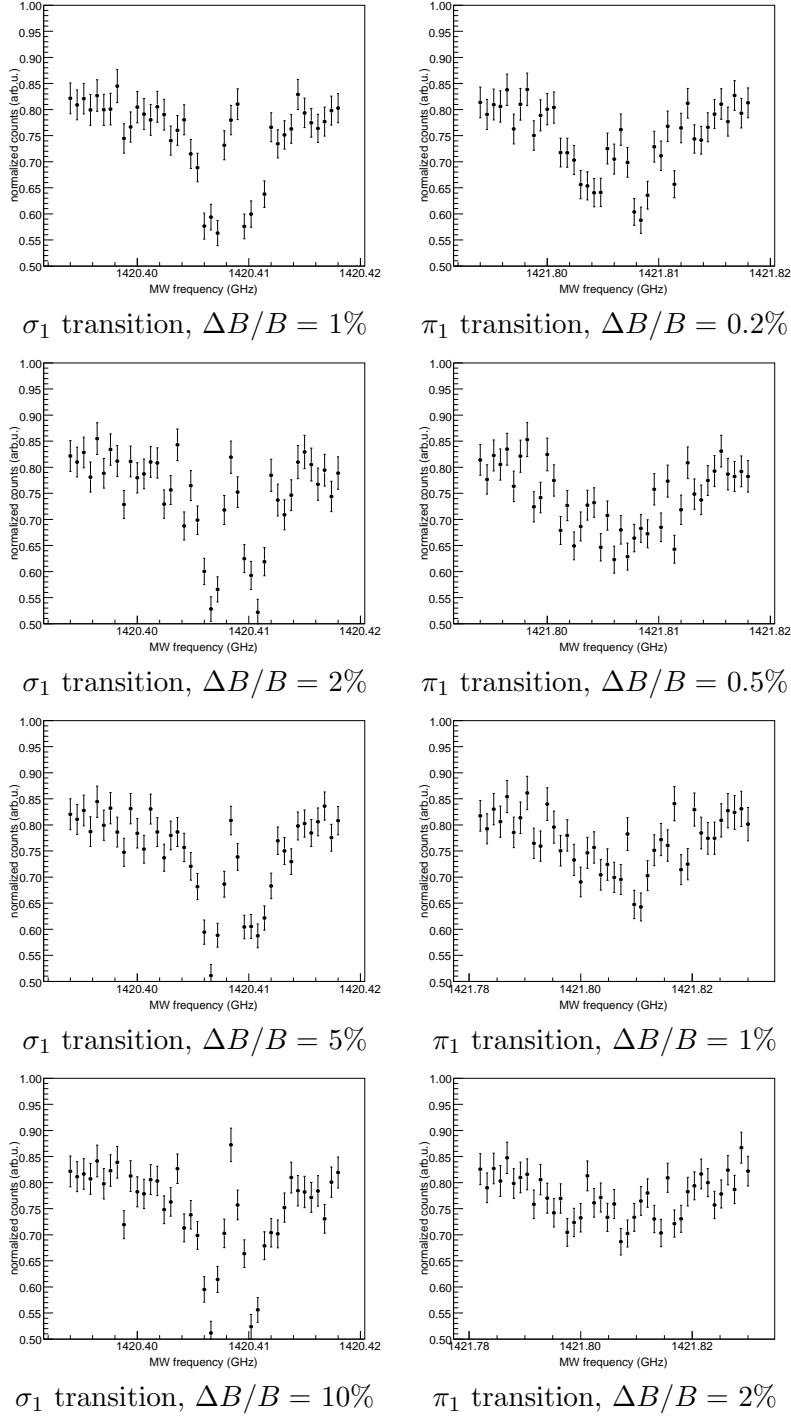
Figure 5.1: *Simulated resonance profiles of the σ_1 (left column) and the π_1 (right column) transitions at an external magnetic field of 1 G but at different magnetic field inhomogeneities $\Delta B/B$. Figures taken from [73].*

field is needed, whereas for the π_1 transition the field has to be perpendicular to the radio frequency field [74]. Hence if both transitions are to be measured with the same spectrometer configuration, a superposition of both cases is needed resulting in a field of 45° with respect to the cavity field. This is desirable, since in this case the magnetic field is the same for both transitions.

The goal of the spectroscopic measurements of antihydrogen is the highest possible precision in order to challenge the currently most sensitive CPT limit. Consequently, the measurement of both transitions is the method of choice. However, the implementation of the measurement setup for the σ_1 transition is much more comfortable and less critical. Thus it is well suited for a first measurement of the yet unknown hyperfine transition in antihydrogen. Furthermore, it would allow a first commissioning of the whole spectrometer line, providing valuable experience with the setup. Therefore it was decided to split the hyperfine transition measurements in two phases. First, a setup suitable for the σ_1 transition measurement is pursued. This is designed such, that it can be upgraded to the measurements of both transitions which will be conducted in the second phase.

5.1.2   Shielding

Independent of the method chosen to determine the ground-state hyperfine transition frequency, an efficient shielding of external fields is unavoidable due to the fact that the spin-flip cavity is positioned between the cusp trap on the one side and the sextupole magnet on the other side. Both devices are sources of considerable stray fields at the location of the cavity. From the cusp side, this stray field is in the order of 30 G whereas roughly 10 G are expected from the sextupole end (Fig. 5.2). In addition, the earth magnetic field of 0.5 G has to be shielded as well. This is necessary since the static field inside the cavity will be varied between 0.1 and 3 G and thus the inhomogeneity induced by the earth magnetic field exceeds the required limits.

Consequently, two different types of shielding have been designed in the framework of this thesis. The first one is positioned in front of the cusp trap at the end close to the cavity to reduce its considerably stronger stray field whereas the other is put around the cavity itself to block all the remaining perturbations.

Since every shielding influences the field lines in its vicinity, the main difficulty for the cusp shielding design was to provide a reasonable shielding effect at the position of the cavity while minimizing its effect on the field in the center of the cusp trap. It was determined via simulations, that a circular shielding made of soft iron was the best choice (see Appendix D.1). The magnetic permeability μ of soft iron is with values between two and three considerably smaller than the one of mu-metal ($\mu \geq 50000$) which is
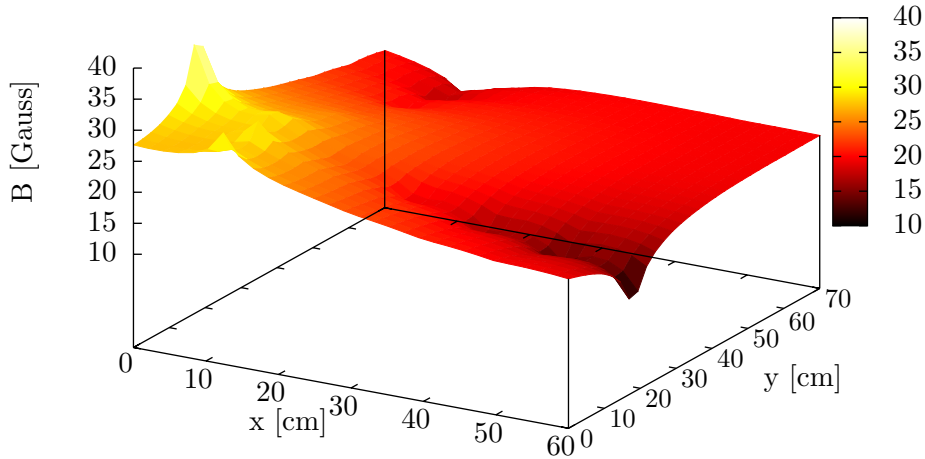
Figure 5.2: *(Color) Stray fields as measured with a hall probe sensor. The left end is the cusp trap side whereas the right end is the sextupole side. The cavity center corresponds to the midpoint of the graph. The measurements were conducted along the beam axis (y = 20) and in two lines perpendicular to it — one close to the cusp trap (x = 10) and the other close to the sextupole (x = 60). The other values shown were determined via interpolation.*

usually chosen as shielding material. Due to this, its effect on the cusp field in the center region is very small (Fig. 5.3) and according to simulations acceptable to avoid severe perturbations that would distort the mixing of positrons and antiprotons. However, it provides reasonable shielding at the exit of the trap and hence the stray field on the cavity side is reduced by 26%. Due to the limited space available and the considerable weight of the shielding that has to be mounted on the existing support frame, only one shielding layer was chosen.

For the cavity, a multiple shielding layer concept — the 'box in the box' principle — was applied to ensure a most effective shielding [69]. Several forms (cubic, cuboid — see below) with different numbers of layers have been considered. These shapes were investigated with two pairs of Helmholtz coils that are necessary to generate a static field fulfilling all the requirements for the measurements of both, the σ_1 and the π_1 transition. The results are summarized in the following.
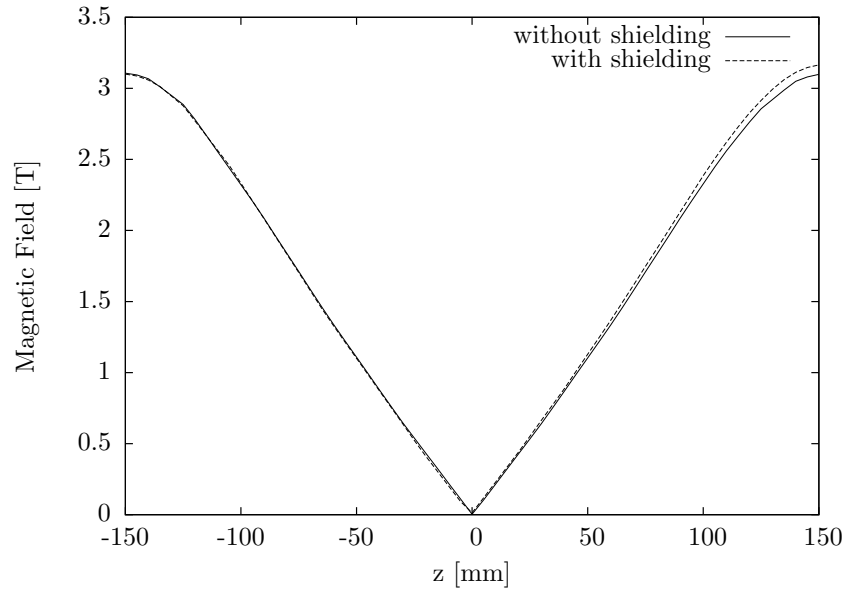
Figure 5.3: *Comparison of the field pattern (absolute value) along the beam direction in the the cusp trap with and without shielding present at the exit as determined by simulations. It can clearly be seen that the shielding affects the field at the cusp exit but not very much in the center. Therefore perturbations that could distort the mixing of the positrons and antiprotons in the center of the trap are not expected while a reduction of the stray field at the trap exit is achieved. Note that an increase of the field in the presence of the shielding is due to the distortion of the field lines caused by the shielding material. The bigger the distortion, the more the field lines are bent and hence the more effective is the shielding.*

5.2   Simulation Studies and Implementation

5.2.1   Double Coil Pair Geometries

The implementation of a very homogeneous field at an angle of 45° with respect to the oscillating field can be done using two pairs of Helmholtz coils[3].

In the following two different types of coil geometries are presented - rectangular coils and round ones to investigate which configuration provides a better field homogeneity. Subsequently, studies of different shielding geometries are presented.

Several simulations varying the distance of two pairs of Helmholtz coils — one in beam direction (Y-coils), the other perpendicular to the beam direction (Z-coils) (Fig. 5.4) — were conducted. For all simulations, a fixed

---

[3]These can be equipped with two additional coil pairs dimensioned such as to fit inside a sphere. This configuration is called Garret coils [75] and is capable of providing fields with an excellent homogeneity.

Table 5.1: *Summary of the used parameters shared by all conducted simulations. The coil dimensions are a consequence of the restricted space between the innermost shielding layer on one side and the cavity on the other. For the rectangular coils, the given radius corresponds to the side length.*

Parameter	Value
Radius of the Y-coils (R_Y)	235 mm
Radius of the Z-coils (R_Z)	180 mm
Current through the coils	5 A
Number of windings	80

radius (or side length for the rectangular ones) for both coils, determined by the available space between the innermost shielding layer[4] and the cavity, and constant current and number of turns were used, ensuring the same magnetic field strength of $\approx 30\,\mathrm{G}$[5] for all simulations. The coil distances (d_Y, d_Z) were varied between 200 mm and 245 mm for the Y-coils and from 90 mm to 200 mm for the Z-coils to determine the optimum distance. These limits again are set by the cavity on one side and the shielding on the other. The parameters common to all simulations are summarized in Table 5.1.

The inhomogeneity $\mathcal{I}$ is calculated using the difference of the maximum ($B_{\max}$) and the minimum ($B_{\min}$) magnetic field value inside the region of interest divided by the mean value (B_{mean}) of said region:

$$\mathcal{I} = \frac{B_{\max} - B_{\min}}{B_{\mathrm{mean}}} \cdot 100 \qquad (5.2)$$

A summary of the results for the different coil geometries is given in the following. A detailed overview of all simulation results presented in this chapter is given in Appendix D.2.

Comparison of round and rectangular coils

The comparison of the different geometries of Helmholtz coils concerning their inhomogeneity in the field region of interest, which is a cylinder with 10 mm diameter and a length of 105.5 mm, showed that the rectangular coils (Fig. 5.4 (b)) provide a slightly better homogeneity than the round ones (Fig. 5.4 (a)). Nevertheless, the latter ones are used for the simulations investigating the different shielding options, since the effect of the coil geometry on the homogeneity is small and in addition, they were considerably faster to calculate due to their symmetry.

---

[4]The dimensions of the innermost layer were assumed to be the smallest possible that could still accommodate the cavity.

[5]This is an arbitrarily chosen field strength. This is justified since the caused relative inhomogeneity is expected to be independent of the field amplitude.

(a)   (b)
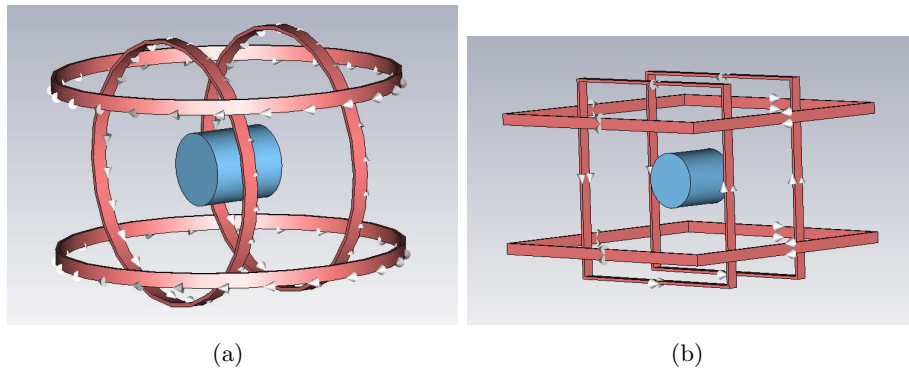
Figure 5.4: *(Color) Example of the round (a) and rectangular coils (b) used for simulations. The light blue cylinder is the area of interest for the field homogeneity inside the cavity.*

Shielding

For considerations of the shielding, two effects have to be taken into account. First the distortion of the magnetic field lines by the shielding, causing a change in the field homogeneity and secondly, the inhomogeneity caused by a superposition of the magnetic field generated by the coils with the external stray fields. For an efficient shielding of the latter, at least three layers of mu-metal are necessary [76]. Unfortunately, the exact number cannot be determined by simulation studies easily, since modeling the large fields (several Tesla) of the cusp trap and the sextupole on the one side and investigating an inhomogeneity in the milli Gauss range inside the cavity on the other would require a code capable of handling seven orders of magnitude in field difference which was not available. Hence, a different strategy is needed to determine how many shielding layers are necessary. It will simply be done experimentally by measuring the field inside the cavity when positioned between the trap and the sextupole magnet with the shielding layers in place. However, if it is found necessary to increase the number of shields, the question is whether this affects the field geometry and thus the homogeneity of the Helmholtz coils much. This however, is a question that can be answered by simulations:

Intuitively, the innermost shielding layer is likely to affect the field lines of the static field most, so comparing simulations with one and three layers of mu-metal shielding in terms of homogeneity, as done in the following, provide the possibility to determine whether the effect of the outer layers on the homogeneity is indeed small. If so, additional layers of shielding material can be added as needed. Otherwise, the field homogeneity has to be determined experimentally for every change of the shielding configuration.

But not only the number of shielding layers is subject to investigation. Also the most suitable geometry has to be determined. Due to space con-

straints around the cavity, a cubic or rectangular geometry is preferable over
e. g. a cylindrical one. Therefore, four different sizes of the shielding were
studied, each with either one or three layers of mu-metal[6]. Each layer had
a thickness of 1 mm and a magnetic permeability of $\mu = 50000$ which is
a typical value for mu-metal. Essentially, three cubic shapes with 550, 630
and 660 mm side length and one cuboid with dimensions $550 \times 550 \times 630$ mm
were investigated. All presented shielding configurations are centered sym-
metrically around the beam axis, since studies done in the framework of
this thesis with asymmetric shielding[7] showed a major increase of the field
inhomogeneity by a factor of 5 to 25.

One Layer Pictures of one cubic type shield as well as one rectangular of
the cuboid type are given in Fig. 5.5. The results for the inhomogeneity of
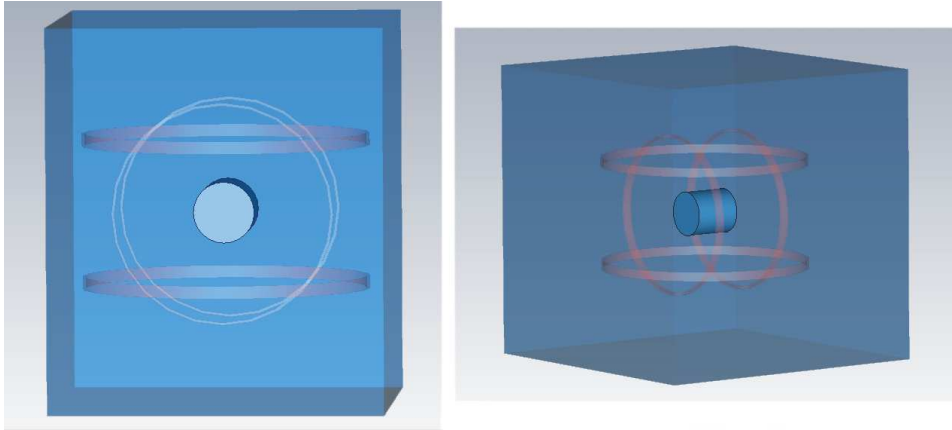
Figure 5.5: *(Color) Schematic drawing of the different shielding box geometries including the Helmholtz coils as implemented for simulations. The rectangular shielding box (left) has the dimensions $550 \times 550 \times 630$ mm and the cubic shielding box (right) has a side length of 550 mm.*

the coils with one layer only are summarized in Table 5.2. For each geometry
the minimal value of the inhomogeneity is given.

Three Layers The distance between the layers was kept constant to
13 mm which was the maximum distance so that all three layers could still
be accommodated comfortably in the experimental setup. For three layers
the results are summarized in Table 5.3.

---

[6]All shielding solutions considered assume a perfectly closed shielding. However, in
reality this is not the case, since several outlets for the beam pipe and the cavity support
are needed. Simulations including these holes have, however, shown that they actually
cause a slight increase in the field homogeneity.

[7]Since there is more room above the cavity, an elongation of the shielding at the top
was investigated as well.

Table 5.2: *Summary of the smallest inhomogeneities achieved for the considered shielding geometries using one layer of mu-metal shielding along with the necessary coil distances.*

Geometry	$\mathcal{I}$ [%]	$(d_\mathrm{Y}/d_\mathrm{Z})$
550 mm cube	0.08	170/230
$550 \times 550 \times 630$ mm	0.07	170/240
630 mm cube	0.87	180/235
660 mm cube	1.11	180/230

Table 5.3: *Summary of the smallest inhomogeneities achieved for the considered shielding geometries using three layers of mu-metal shielding along with the necessary coil distances.*

Geometry	$\mathcal{I}$ [%]	$(d_\mathrm{Y}/d_\mathrm{Z})$
550 mm cube	0.08	170/215
$550 \times 550 \times 630$ mm	0.07	170/225
630 mm cube	0.85	180/225
660 mm cube	1.02	180/230

Conclusions

As can be seen from the simulation results presented above, the number of layers does indeed not influence the field homogeneity much. Therefore, the approach to start with three shielding layers and add additional ones if needed is feasible.

It can also be seen that a rectangular shield provides the best overall field homogeneity. Thus, a shielding of this geometry was implemented for the first phase of the static field setup, the measurement of the σ_1 transition, and is presented in the following.

5.2.2   Shielding Implementation

For the experimental implementation of the shielding, two layers[8] of rectangular shaped mu-metal boxes — the form which determined to provide the best homogeneity for the two coil pairs — were chosen. The technical design of the inner layer as well as its manufacturing was done by Magnetic Shields Ltd [77]. It consists essentially of a bottom and a top part with the upper part supported by the lower one via a guiding rail. Its dimensions are $531 \times 531 \times 606$ mm. The outer layer was designed within the framework of this thesis (Fig. 5.6). It consists of four corner pieces screwed together in their overlap as well as a top and a bottom plate. Its dimensions are $561 \times 561 \times 636$ mm. The manufacturing was done by Ohtama Co., Ltd [78].

---

[8]Two layers of shielding are enough for measuring the σ_1 transition, since it is less sensitive to inhomogeneities in the magnetic field.
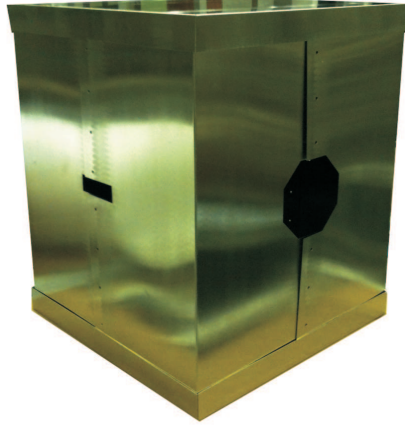
Figure 5.6: *(Color) The outermost shielding layer made of four corner pieces held together with screws and a top and bottom plate.*

5.2.3 Single Coil Pair Geometries

The measurement of the σ_1 transition requires a field parallel to the beam direction which can be implemented by a single pair of Helmholtz coils.

For the simulation studies of this case, the coil radius is kept with 235 mm the same as for the Y-coils in the double coil setup presented in the previous section. This allows an easy upgrade to the two coil configuration needed in phase two. Only the number of windings has been increased to 90 since this facilitates mechanical implementation. The distance of the coils is again varied between 200 mm and 245 mm to determine the value for optimum homogeneity.

All simulations were conducted using two layers of shielding with the final dimensions and properties as mentioned above. As a supply current, 0.2 A as well as 0.5 A have been used. Since the inhomogeneities for both currents is nearly the same, only the simulation results of the 0.2 A case are summarized in Table 5.4. A graphical representation is given in Fig. 5.7. According to the simulation results, a distance of 215 mm between the Helmholtz coils provides the best field homogeneity in the region of interest and should be applied for the measurements of the σ_1 transition.

Table 5.4: *Simulation results of the field inhomogeneity depending on the coil distance. A supply current of 0.2 A has been used for the simulation generating a field of roughly 1 G.*

Distance [mm]	Inhomogeneity [%]
200	0.77
205	0.54
210	0.39
215	0.33
220	0.5
225	0.65
230	0.82
235	1.01
240	1.22
245	1.45
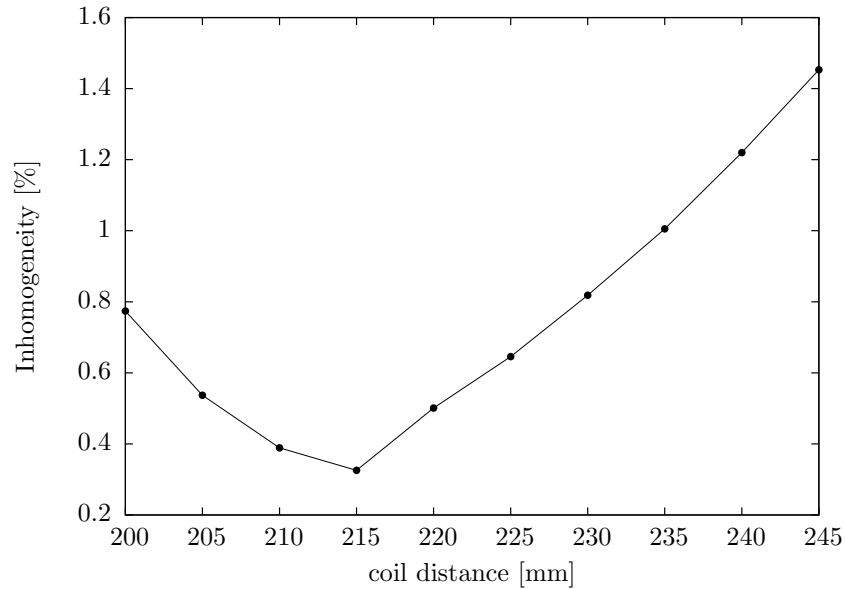
Figure 5.7: *Dependency of the field inhomogeneity in the volume of interest with respect to the coil distance. The plotted values are simulation results for a current of 0.2 A, resulting in a field of roughly 0.9 G. The line in the graph is provided to guide the eye.*

5.2.4 Final Coil Design

As a final design, Helmholtz coils with a radius of 235 mm (at center of wiring — innermost radius is 220 mm) and 90 windings (10 rows, 9 windings per row) were chosen. They were wound using a copper wire of 1.6 mm copper (outside diameter 1.67 mm including insulation) onto a basic support made of fiberglass loaded with epoxy (Fig. 5.8 (a)).

The coils are mounted on aluminum profiles fixed on the side of the cavity using threaded brass rods (Fig. 5.8 (a)). These rods together with aluminum cylinders are used for accurate spacing of the coils. Simulation results show, that the necessary accuracy for centering the coils around the volume of interest is ± 5 mm[9]. Offsets within this range are not affecting the field homogeneity too much.

5.3 Magnetic Field Measurements

Several measurements of the field provided by the Helmholtz coils were conducted. They were done using a Hall probe sensor (Metrolab THM1176-LF) mounted on a table movable in three dimensions (Fig. 5.8 (a)). Four planes were chosen for measurement in order to provide a good representation of the whole volume (Fig. 5.8 (b)).

Several measurements for different field strengths and coil distances have been conducted. A summary of the measurement parameters is given in Table 5.5. For the distance of 223 mm only one plane (yz) was measured. The latter measurement was repeated, to check the resolution of the hall probe sensor.

Table 5.5: *Summary of the different parameters of the magnetic field measurements of the Helmholtz coils.*

Current [A]	Magnetic field [G]	Coil distance [mm]
0.2	0.9	208
0.5	2.3	208
1.1	5.0	208
0.5	2.3	211
0.5	2.3	223

5.3.1 Evaluation of Measurements

In the following, a short overview of the measurement uncertainties is given followed by the determination of the homogeneity through the conducted

---

[9]This accuracy is true for the distance of the coils only. The coil planes have to be aligned perfectly parallel with respect to each other.

(a)   (b)
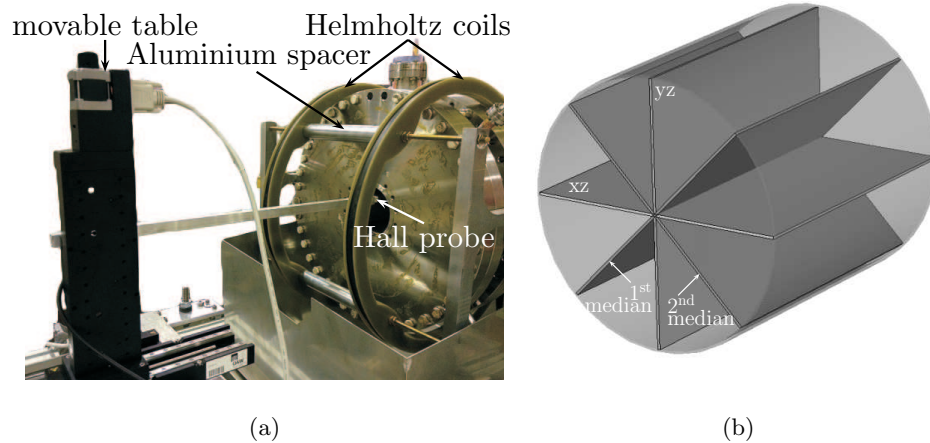
Figure 5.8: *(Color) (a) Measurement setup for field mapping of the Helmholtz coils over the whole cavity aperture. The top part of the shielding box is not mounted yet, providing a better visibility of the setup. (b) Illustration of the measured planes inside the volume of interest. A good representation of the volume is achieved.*

measurements. These results are subsequently compared with corresponding results from simulations.

Measurement Uncertainties

As a first step, the data for each field strength and distance were checked for points common to two or more planes. It was found, that the first median plane and xz as well as the second median and xz plane share one common line of measurement points. These lines, together with the yz plane measured twice at 223 mm distance, were used to check the precision[10] of the probe and whether it is in the same order of magnitude as specified by the manufacturer.

According to the data sheet of the probe, its precision is ± 20 mG without averaging and increasing by $1/\sqrt{N}$ where N is the number of averaged values. So in order to minimize the resolution error of the probe, each measurement point was averaged for 7 s (≈ 10000 measurement values) leading to a resolution ≈ 0.2 mG. This can be compared to the standard deviation determined by points measured several times, which is in the order of 9 mG maximum. Thus, the specified resolution value seems at first underesti-

---

[10]The precision is a measure for the deviation of the measured data points from the mean value.

mated. However, in the fluctuations of the common measurement points, the uncertainty of the power supply is included. Since this is specified to be quite large by the manufacturer (see below), no conclusion on the real precision of the probe can be drawn.

One further source of uncertainty is the accuracy[11] of the Hall probe, specified with $\pm 0.2\,\mathrm{G}$ by the manufacturer. However, this value is a constant offset common to all data of one field strength and can hence be neglected in the uncertainty calculation of the inhomogeneity. However, it is of importance, when comparing absolute field values, e. g. in case of the comparison of the measured field strength with simulation results (see Section 5.3.1).

Another source is the instability of the magnetic field due to a ripple in the supply current. For the used power supply (TTI TSX 3510P) this ripple is specified to be $3\,\mathrm{mA}$. Depending on the field strengths, this leads to an uncertainty between 0.3% and 1.5%.

Determination of Homogeneity

To calculate the inhomogeneity $\mathcal{I}$ of the field, Eq. 5.2 is used. This approach is very conservative, giving the maximum possible uncertainty. Another way would be to use the standard deviation of the data distribution as a measure of homogeneity. This would, however, assume a Gaussian distribution of the measured points, which is not true for this case since the data points are not statistically distributed but follow a specific field geometry given by the coils (Fig. 5.9). Therefore the more conservative approach presented above
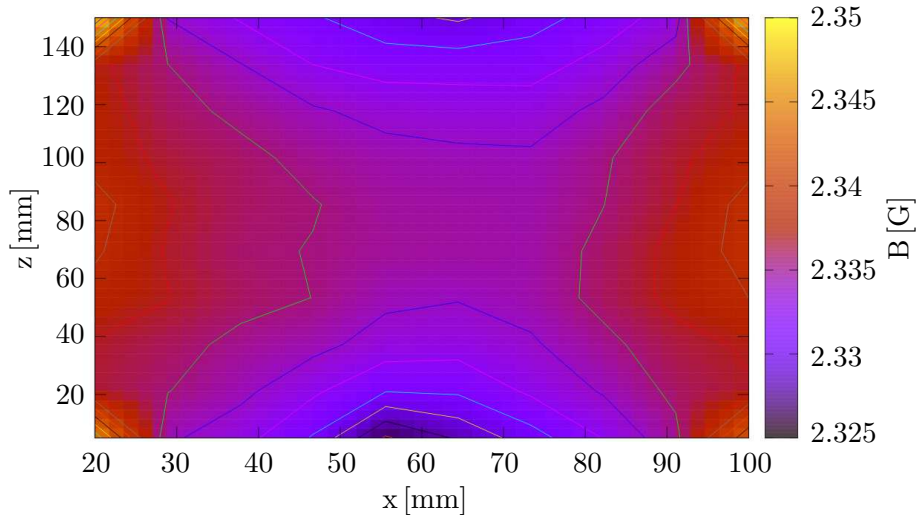

Figure 5.9: *(Color) The field distribution in the xz-plane for a field of 2.3 G. The field increases on the top and bottom of the graph since it gets closer to the coil edges.*

---

[11]The accuracy specifies the deviation of the mean value of a set of data points from the true value.

is taken for the evaluation of the measurement as well as simulation data.

The determination of the inhomogeneity uncertainty is done using standard formulas for uncertainty propagation which can be found in any statistics book, e. g. [79].

Since the magnetic field B in the coils is proportional to the supply current I, the relative error is the same for both cases:

$$\frac{\sigma_I}{I} = \frac{\sigma_B}{B} \tag{5.3}$$

This uncertainty is the dominant one and hence the only one considered in the following.

The uncertainty of the mean value of the magnetic field (B_{mean}) is the standard deviation σ divided by the square root of the total number of measurement points N:

$$\sigma_{B_{\mathrm{mean}}} = \frac{\sigma}{\sqrt{N}}$$

Using the propagation of uncertainties for Eq. 5.2, this leads to the uncertainty of the inhomogeneity:

$$\sigma_{\mathcal{I}} = \sqrt{\frac{\sigma_{B_{\max}}^2}{B_{\mathrm{mean}}^2} + \frac{\sigma_{B_{\min}}^2}{B_{\mathrm{mean}}^2} + \left(\frac{B_{\max} - B_{\min}}{B_{\mathrm{mean}}^2}\right)^2 \cdot \sigma_{B_{\mathrm{mean}}}^2} \cdot 100 \tag{5.4}$$

All the results are summarized in Table 5.6. The simulations were conducted using the same coil geometry, the same currents, distances and shielding boxes as for the measurement.

Table 5.6: *Summary of the field homogeneity of the conducted measurements and simulations. For the former, all four planes have been taken into the account for the different field strength values B. For the different distances d, only the yz-plane was used since it was the only plane measured at the largest distance. The simulation results always take into account the total volume of interest.*

Fixed distance: 208 mm

	Measurement		Simulation	
I [A]	B_{meas} [G]	$\mathcal{I}_{\mathrm{meas}}$ [%]	B_{sim} [G]	$\mathcal{I}_{\mathrm{sim}}$ [%]
0.2	1.0	4.4 ± 2.1	0.9	0.44
0.5	2.3	3.2 ± 0.8	2.3	0.44
1.1	5.1	2.2 ± 0.4	5.1	0.44

Fixed field strength: 2.3 G

d [mm]	$\mathcal{I}_{\mathrm{meas}}$ [%]	$\mathcal{I}_{\mathrm{sim}}$ [%]
208	2.4 ± 0.8	0.44
211	2.3 ± 0.8	0.39
223	4.0 ± 1.1	0.57

5.3.2 Discussion of the Results

It can be seen that the measured field values for the given currents are in good agreement with the simulation results (Fig. 5.10). However, as can
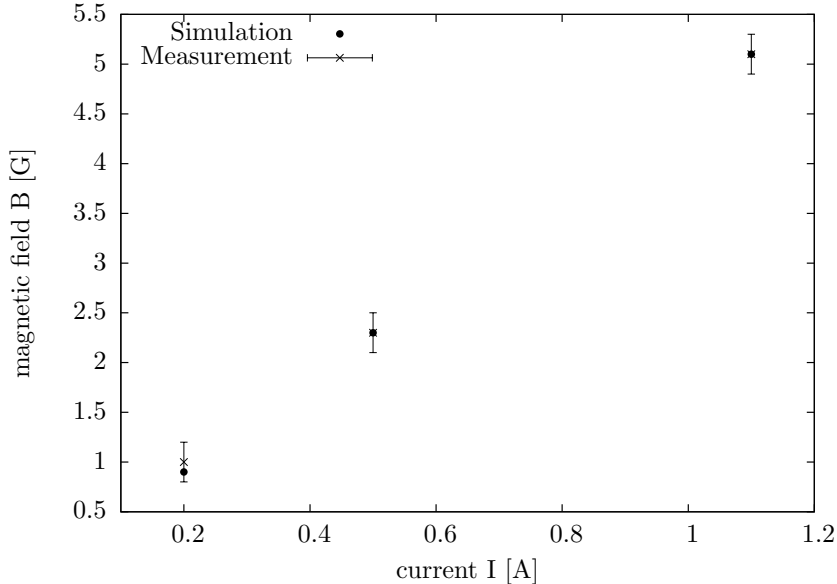
Figure 5.10: *The inhomogeneity of the magnetic field for different field strengths as determined out of the conducted magnetic field measurements.*

be seen from Fig. 5.11, all evaluated values are consistent with each other within a two sigma (different field strength) or even one sigma (different distances) interval. This makes a comparison to simulation difficult and also the determination of the best distance cannot be confirmed by the measured values. However, it can be seen that the measured inhomogeneity is roughly a factor ten higher than the simulation results. A possible explanation is the summary of several effects. First, a perfectly stable supply current for the coils is assumed in the simulations. This is not the case for the measurements — in fact the uncertainty of the used power supply as specified by the manufacturer was the dominant error in the evaluation of the field homogeneity. Another effect is the magnetic permeability of the simulated shielding layers which was set to the maximum value specified by the manufacturers. Since the shielding has considerable influence on the field homogeneity, a lower μ value can contribute to the discrepancy between simulations and experiment. Furthermore, the implementation of the coils in the simulation program is done specifying current path with have an infinitely small wire thickness. A lateral expansion of the coils might increase the inhomogeneity of the field. Finally, the presence of external stray fields, which were not considered in the simulations (see Section 5.2.1) can be an additional reason for a higher inhomogeneity.
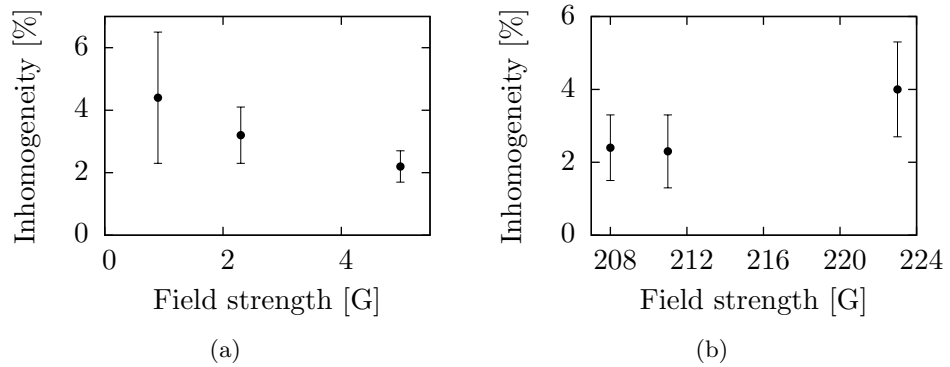
Figure 5.11: *The inhomogeneity of the magnetic field for different field strengths (a) and different coil distances (b) as determined from the conducted magnetic field measurements.*

Independent of the uncertainties, it can be concluded, that the inhomogeneity is better than 6.5% for a distance of 208 mm, better than 3.1% for 211 mm and better than 5.1% for 223 mm. Even these upper limits of the determined inhomogeneity values are well within the limitations for the σ_1 transition measurement. Thus the presented setup comprising a single coil pair as suggested by the simulations as well as two layers of mu-metal boxes fullfils all the necessary requirements. Hence it can be concluded that the implementation of the static field for phase one has been successfully completed.

Chapter 6

Summary and Outlook

The design and the successful mechanical implementation of a spin-flip cavity used for hyperfine transition measurements in antihydrogen have been presented. It was shown that a cavity implementing a strip-line resonator design is capable of providing a purely transverse field with an inhomogeneity of 3% and a resonance frequency of 1.42 GHz and thus fulfills all required specifications. Furthermore, it proved to be suitable for ultra high vacuum applications achieving an ultimate pressure of $2 \cdot 10^{-9}$ mbar.

In addition, the design and implementation of the static magnetic field using a set of Helmholtz coils has been presented. Simulation studies for several coil and shielding geometries have been conducted, leading to the determination of the optimum coil geometry for a double pair of Helmholtz coils as well as for a single pair. Measurement results of the field homogeneity of the implemented single coil pair have been presented and evaluated proving that the implemented configuration has an inhomogeneity of less than 7% and thus is suitable for the measurements of the σ_1 transition of antihydrogen.

The cavity has been integrated into the ASACUSA beam line, ready for first measurements of antihydrogen. However, no beam of antihydrogen has been delivered by the cusp trap so far and hence spectroscopic measurements could not be conducted.

The next step is the measurement of the σ_1 transition with the present setup. However, first detailed measurements of antihydrogen are expected only in two years from now — due to the long shut down of the CERN accelerator chain in 2013. Future steps include the implementation of a second pair of Helmholtz coils to the cavity setup, enabling the measurement of both, the σ_1 and the π_1, transition as well as the installation of a setup using a second cavity, similar to the one designed and constructed for this thesis. Such a configuration (Ramsey setup) provides a much better resolution. In addition, measuring the field homogeneity for the single coil geometry inside the spectrometer line as well as initial measurements for the double coil pair

setup is required.

For further testing the spin-flip cavity, a beam line with atomic hydrogen will be implemented next year which is currently developed in the framework on another thesis. This setup will provide a benchmark independent of the availability of ground-state antihydrogen.

Appendix A

Discovery of Antimatter

A.1 Discovery of the Positron

During his studies of cosmic ray signatures in cloud cambers, Carl D. Anderson discovered an interesting track that seemed to be caused by a positively charged particle much lighter than the proton (Fig. A.1). Anderson
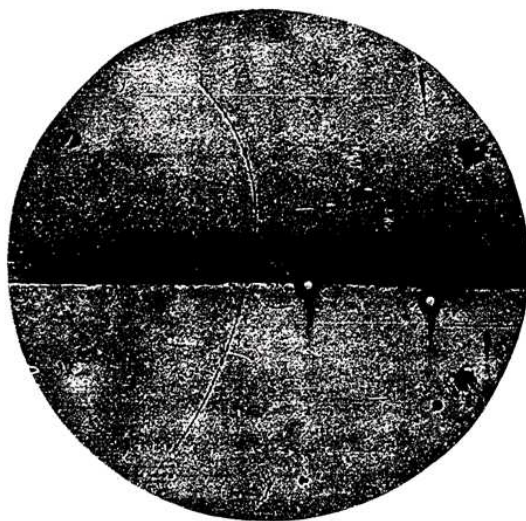
Figure A.1: *Track signature Anderson obtained using a cloud chamber to measure cosmic rays. (Picture taken from [12])*

was aware of Dirac's theory, predicting a particle of the same mass as the electron but with opposite charge. He understood that the observed particle might be exactly said antiparticle. But such a thing is not postulated lightly. So Anderson thought of several interpretations of the observed phenomenon which will be quickly summarized here. For more detailed information, the reader is referred to the original publication [12]. The possible interpretations of the particle track(s) shown in Fig. A.1 given by Anderson were:

- The track corresponds to a positively charged particle with mass much less than the proton mass. This particle entered the lead plate from below, traversed the lead loosing energy and exited it via the above track.

- The track is caused by a proton entering from below, traversing the lead and exiting the plate above having lost energy. The corresponding energy of a proton having a curvature like the upper trace would be 300 kV. A proton of this energy however has a mean free path length of 5 mm. The found track is more like 5 cm without any noticeable change in curvature.

- The track is caused by two electrons created at the same time. One entering the lead from above, one from below. Such an event has a probability of occurrence of 1:500. The probability of the two created tracks being aligned in such a way as to appear as one is infinitely small.

- The trace is caused by an electron entering the lead plate from above, traversing it while gaining in energy and exiting it below.

- The tracks are caused by two particles emitted from the lead after the plate was hit by a photon. One particle exiting the plate above, one exiting below. Just like the first interpretation, this one also leads to the existence of a positively charged light particle.

As can be seen the most likely interpretations of this track were implying the existence of a new particle which Anderson called the positron.

A.2   Discovery of the Antiproton

In 1955, Chamberlain and Segrè found experimental proof for the existence of the antiproton [13]. They produced the first antiprotons by extracting a proton beam out of the Bevatron synchrotron onto a copper target (Fig. A.2). The difficulty of this measurement was the distinction of an antiproton signature from the heavy background of π mesons since for one generated antiproton at the target 62 000 mesons are produced. Due to coincidence pulses in scintillation detectors and velocity selective Cherenkov counters, the particles could be distinguished due to their different time of flight inside the experimental beam line (Fig. A.3). Furthermore the same experiments were conducted for mass measurements of protons in order to determine the accuracy for mass measurements of the antiproton. It was shown that the obtained accuracy of values for the proton mass were within 10% of the known standard. The system was then adjusted for different masses around the expected proton and antiproton mass to determine whether the detected

Figure A.2: *Experimental setup used by Chamberlain et al. to discover the antiproton. (Picture adapted from [13])*
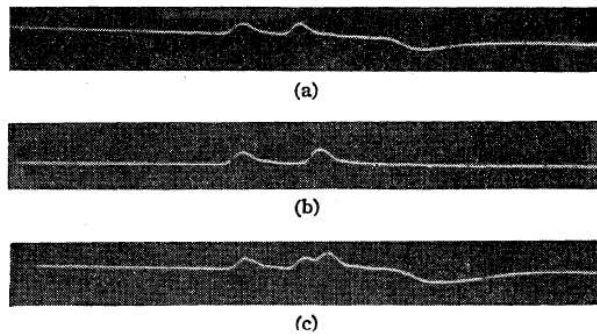
Figure A.3: *Signature seen on the Oscilloscope for a mesonic event, an antiproton and an accidental event (from top to bottom). (Picture taken from [13])*

particles are really protons/antiprotons or yet unknown particles of different mass. These experiments resulted for both negatively and positively charged particles[1] in a peak at the proton mass leaving the mass of the antiproton to be within 5% of the proton mass.

A.3   Antihydrogen — the Production of the First Antiatom

It was in 1995 when the first antihydrogen atoms have been produced at CERN. Inside the Low Energy Antimatter Ring (LEAR) a beam of antiprotons with a momentum of $2\,\mathrm{GeV/c}$ was circulated. At one point inside LEAR a jet of xenon gas was injected with the gas flow perpendicular to the beam axis (Fig. A.4) thus forming a target for the moving antiprotons. Every once in a while the antiprotons passing through the gas would create

---

[1]The charge of a particle is determined by its curvature when traversing a bending magnet.

a positron/electron pair. If such a positron would then happen to propagate in beam direction with the same velocity as an antiproton, both could combine to an antihydrogen atom. Since no longer subject to the bending force of the magnet, the neutral antihydrogen left the ring. It was detected by reionization (Fig. A.4): Passing through a silicon detector where only the positron would annihilate leaving a trace of γ rays detectable with scintillation counters encircling the silicon detector. The momentum and the time of flight (TOF) of the remaining antiproton was measured with a subsequent mass spectrometer.
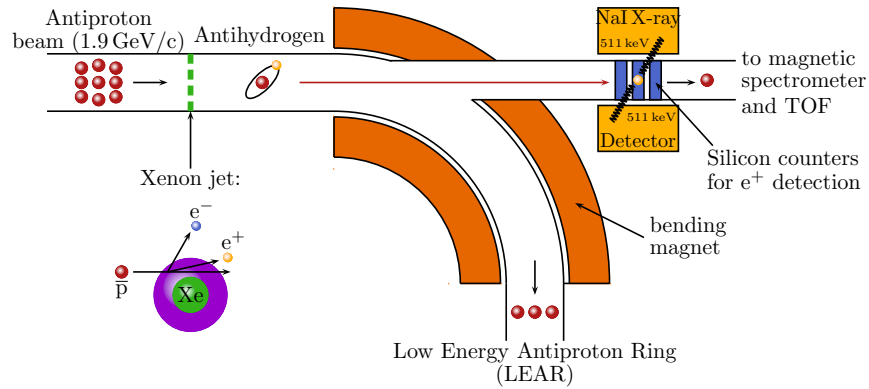
Figure A.4: *Overview of the experimental setup that led to a successful production of the first antihydrogen atoms. (Picture adapted from [47])*

With this method the first 9 antihydrogen atoms were produced. This caused a sensation and a huge resonance not only within the scientific community but also with the broad public and led to the continuation of the antimatter physics program at CERN which was about to being shut down in favor of the high energy physics program around the construction of the large hadron collider (LHC).

Appendix B

Antiproton Beam Production

This appendix is dedicated to the presentation of the antiproton facility at CERN. Special emphasis is put on the antiproton decelerator (AD) which collects the antiprotons and decelerates them to an energy level feasible for the experiments hosted inside it. Subsequently, a brief description of these experiments is given.

B.1 Generating Antiprotons

When smashed onto a solid target, highly energetic protons produce — among many other things — proton/antiproton pairs. At CERN, the proton synchrotron (PS) produces an adequate beam for such a task consisting of protons with a momentum of $26\,\mathrm{GeV/c}$. A schematic view of the accelerator complex[1] at CERN with special emphasis on the antiproton production routine is given in Fig. B.1.

For antiproton production the proton beam extracted from the PS is shot onto a metal (iridium) target. However, this process is very inefficient: Only once in every million collisions a proton/antiproton pair is produced. So with an incident beam of roughly 10^{13} protons, the antiproton yield per shot amounts to $5 \cdot 10^7$ particles.

The produced antiprotons are then collected by a magnetic horn (Fig. B.2). The horn is an aluminum tube with a wall thickness of 1mm carrying a pulsed current of $400\,\mathrm{kA}$ [82]. It creates an azimuthal magnetic field on the outside with a field free region on its inside. Such a field configuration allows the antiprotons to exit in a nearly parallel beam.

---

[1] A more detailed description of the accelerator chain can be found in [80].
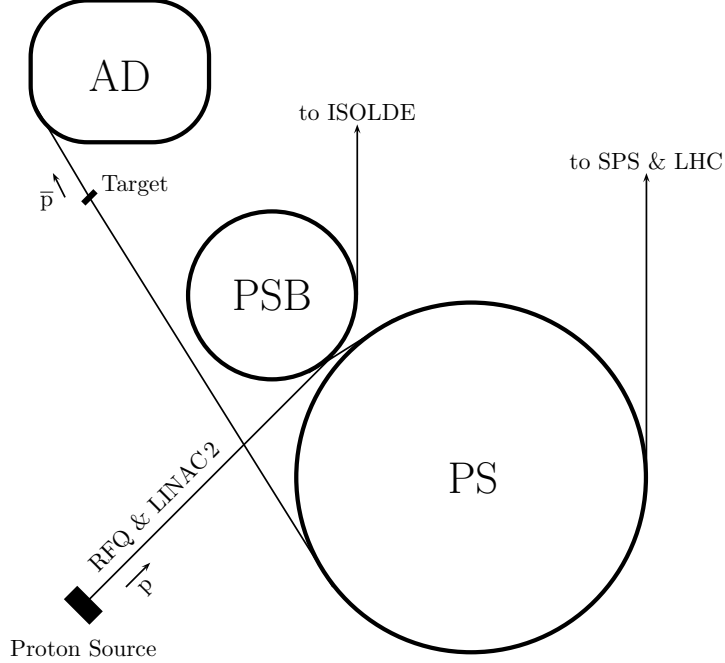
Figure B.1: *Schematic drawing of the CERN accelerator chain. Protons coming form the source are accelerated by a combination of linear and circular accelerators. The beam extracted from the Proton Synchrotron (PS) is shot onto a metal target creating proton/antiproton pairs. The collected antiprotons ($\bar{p}$) are finally injected into the AD where they are decelerated to an energy of roughly 5 MeV.*

B.2   The Antimatter Decelerator

The antiprotons leaving the horn are injected into the AD ring [83, 84]. The ring itself consist of a series of bending and focusing magnets (Fig. B.3) — similar to a common accelerator — distributed over a circumference of 182 m. It has been a unique facility for the production of ultra low energy antiprotons since it became operational in 2000. It replaced the complex formerly used for antiproton production consisting of the Antiproton collector (AC), antiproton accumulator (AA) and low energy antiproton ring (LEAR).

At their injection, the antiprotons have an initial momentum of 3.57 GeV/c with a momentum spread of $\pm 3\%$. Two cooling systems are used to compensate this spread as well as the energy spread caused by the subsequent deceleration steps. Since the process of beam cooling is crucial for the antiproton deceleration, the two processes implemented in the AD are briefly discussed here. For a more detailed introduction to the subject, the

Figure B.2: *Picture of a magnetic horn as used at CERN. It collects the produced antiprotons from the target and converts them into a parallel beam. (Picture taken from [81])*
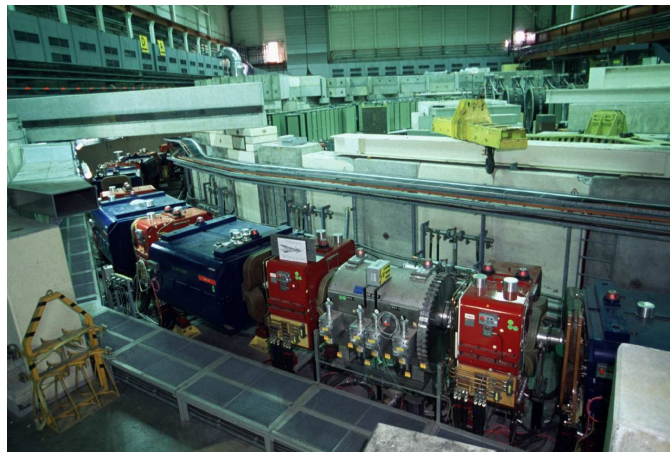
Figure B.3: *Partial view of the antiproton decelerator at CERN. This picture was taken after installation of all components and before finishing the concrete shielding protecting the surrounding area from the rings radiation. The blue dipole magnets as well as the red quadrupole magnets are clearly visible. (Picture taken from [85])*

reader is referred to [86, 87, 88] and especially to [89, 90] as well as references therein.

B.2.1   Cooling

The term of beam cooling[2] always refers to a reduction of the beam size and energy spread. It was believed for a very long time that the phase space density of a beam has to stay constant when influenced by external electromagnetic fields. This is known as Liouville's theorem and holds true for Hamiltonian systems. Nevertheless, this is strictly valid only for continuous systems. So for a beam consisting of individual particles appearing as discrete points in phase space with empty space in between, this theorem can be circumvented. It is possible, to a certain extend, to transfer empty phase space inside the beam center to the outside, formally not changing the volume the beam occupies.

Inside the AD ring two cooling systems are installed:

- stochastic cooling and

- electron cooling.

Both will be shortly presented below.

Stochastic Cooling

The process of stochastic cooling is based on the observation and corrections of discrete sets of particles within the circulating beam. It can be applied to all three dimensions, nevertheless, for reasons of simplicity only the longitudinal cooling is discussed here. Consider a single particle circulating at a certain velocity inside the accelerator ring. Its velocity might deviate from the desired design velocity and hence it either needs to be accelerated or decelerated. Thus, measuring the velocity of the particle would allow the correction of its orbit by applying an appropriate kick into the right direction. If this could be done for each particle, the beam would be on its ideal orbit in no time. However, for an amount of 10^7 particles per filling, this is not possible. Fortunately, one can do the next best thing – one can split the beam into samples, measure their mean velocity and correct for this. Essentially, this procedure is stochastic cooling. The passing particles induce a voltage in pickup electrodes (Fig. B.4) installed on both sides of the beam pipe. The passing beam induces a voltage in both and the difference of these readings is a measure of the beam displacement form the ideal orbit. For each sample, this information is fed to a strong kicker magnet which applies a corresponding correction, leading to an average increase of beam density.

---

[2]The term has its origin in the kinetic gas theory which can be used to describe the beam.

Applying this technique over many turns (e.g. 10^7 turns), this leads to a significant cooling effect.
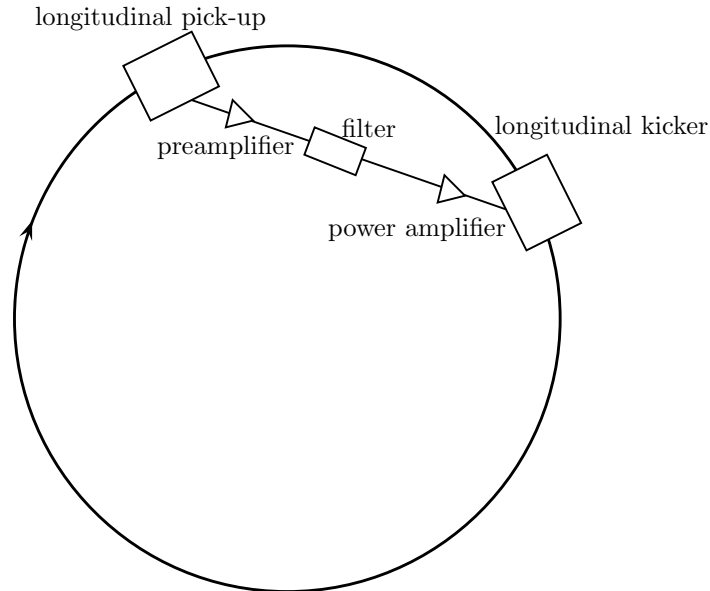
Figure B.4: *Schematic drawing of a longitudinal stochastic cooling system. (Picture adapted from [87])*

Electron Cooling

Electron cooling operates in the same way as a heat exchanger. The heavier antiprotons, which are to be cooled, pass through a cloud of electrons distributed over a section of the accelerator ring. The electrons move with the average velocity of the beam, absorbing higher momentum of faster particles and accelerating slower ones. Overall, this causes a momentum spread reduction and hence the beam is cooled. Since fresh electrons are provided for each turn, considerable cooling of the beam is achieved. Electron cooling is applicable only at low energies, since the Dc voltage driving the electrons through the cooling section of the ring limits the electron velocity.

B.2.2 Vacuum Aspects

For every accelerating or decelerating machine, a good vacuum is necessary to avoid increase of emittance and beam loss. However, especially when dealing with slow antimatter, it is crucial to have an excellent vacuum since the antimatter beam will not only blow up, but antiparticles will annihilate immediately when encountering a matter particle. Therefore, the vacuum inside the Ad ring is kept at $5 \cdot 10^{-10}$ mbar.

B.2.3 The AD Cycle

To conclude the section on the antiproton decelerator, a full deceleration cycle will be presented in the following.

At injection of the beam into the AD, the first step (precooling) is to reduce the momentum spread in the antiproton beam coming from the magnetic horn. This is done using a bunch rotation routine [91], transforming a short bunch with large transverse dimensions into a long bunch with small transverse dimension (Fig. B.5) by changing the RF voltage. After this
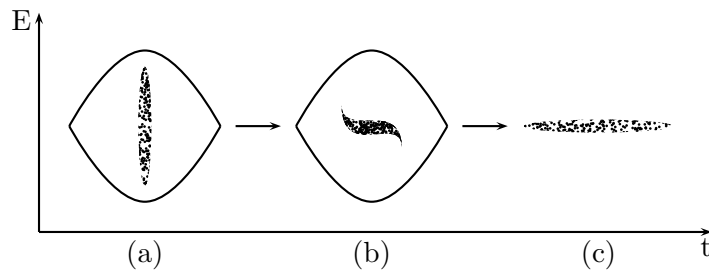
Figure B.5: *Initial short bunch with a large momentum spread (a) is transformed to a long bunch with smaller momentum spread (b). Quick adjustment of the voltage creating the bucket leads to a coasting beam, keeping the small momentum spread (c). (Picture adapted from [91])*

procedure, the beam is now prepared for the stochastic cooling process. Initially stochastic cooling is applied directly after the bunch rotation at an energy of 3.5 GeV/c to further increase the beam density. Afterwards, the beam is decelerated to 2 GeV/c via an RF system. The deceleration causes a blow up of the beam which is counteracted by a second stochastic cooling step. The deceleration and cooling cycle is done again two times using electron cooling instead of stochastic cooling. This leaves the antiproton beam at a momentum of 300 MeV/c after the first cycle and at 100 MeV/c after the second one. In this condition, the beam is finally ready for extraction towards the experiments. It takes 100 s (60 s according to design) for the injected antiprotons to complete the cycle. An illustration of it is given in Fig. B.6.

B.3 The Experiments

Due to a respectable amount of concrete shielding (Fig. B.3) around the decelerator, it is possible for physicists to work in the area enclosed by the AD even during its operation. Currently, there are five experiment hosted inside the ring:

- ACE

- AEGIS
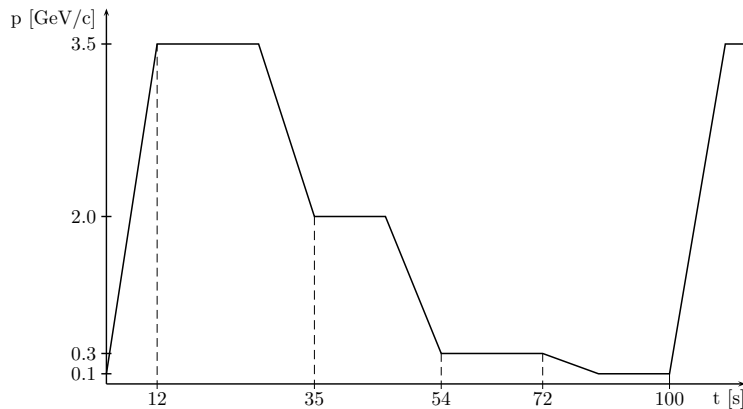
Figure B.6: *One deceleration cycle of the AD machine. Antiprotons enter with a momentum of 3.5 GeV/c and are provided to the experiments at a momentum of 100 MeV/c. (Picture adapted from [83])*

- ALPHA

- ASACUSA and

- ATRAP

ACE is a collaboration of physicist, biologists and medical scientists. They investigate the suitability of antiprotons for cancer therapy. This is done by bombarding living hamster cells with antiprotons and monitoring the inflicted damage. This strategy has already delivered promising results. For more information on this experiment or subject, the interested reader is referred to [92, 93].

AEGIS is a novel experiment at the AD that has started its operation only in 2011. This experiment aims to investigate the behavior of antihydrogen under the force of gravity. They will literally drop antihydrogen in a vacuum chamber, measuring its fall with a Moiré interferometer to determine the gravitational effect of matter on antimatter. More information on AEGIS can be found at [94].

ALPHA, ATRAP and a part of the ASACUSA collaboration all aim at the spectroscopy of antihydrogen. For information on the first two collaborations the reader is referred to [95] for the ALPHA and to [96] for the ATRAP collaboration.

Within the ASACUSA collaboration, several different experiments are conducted [97]:

- laser spectroscopy of anitprotonic helium

- microwave spectroscopy of anitprotonic helium

- atomic and nuclear colission experiments

- microwave spectroscopy of the ground-state hyperfine splitting of antihydrogen

This thesis is a contribution to the latter experiment. For more information on the other experiments, the reader is referred to [97] as well as to references therein.

B.4   The ASACUSA RFQ

The 100 MeV/c antiproton beam[3] provided by the AD is extracted towards the ASACUSA beam line. Since the highest acceptable energy of antiprotons to be caught in an electromagnetic trap is in the keV range, [48] the energy of the antiprotons provided by the AD is still too high for capturing. Hence, an additional deceleration of the antiproton beam is necessary. This can be achieved by passing the beam either through thin foils, so called degrader foils or, as is done in ASACUSA, through another decelerator, a radio frequency quadrupole (RFQ). The advantage of an RFQ with respect to degrader foils is its higher transmission efficiency. Comparing the efficiency of a degrader foil of e. g. 70 mg/cm^2 as is used in other AD collaborations to the RFQ, the numbers of antiprotons available for experiment are increased by a factor 50 in the latter case [48] – $2.5 \cdot 10^4$ with the degrader foil compared to $1.2 \cdot 10^6$ in case of the RFQ. Nevertheless this corresponds to a total efficiency of only 4% of the number of antiproton initially provided by the AD.

The RFQ in use for the ASACUSA experiments is capable of delivering antiprotons in an energy range between 10 to 120 keV using a DC bias between the RF structure and the tank. It consists of four rods parallel to the beam axis, creating a quadrupole field. The rods are modulated along the beam line (Fig. B.7 (a)) with decreasing modulation factor to efficiently decelerate the antiprotons and are mounted on a ladder structure along with 34 RF cells (Fig. B.7 (b)). The total length of the RFQ is 3.55 m and its operating frequency is 202.56 MHz.

A more detailed study of the RFQ and the ASACUSA beam line in general can be found in [98, 100, 101].

---

[3]The momentum of 100 MeV/c corresponds to $\beta \approx 0.1$ and to a kinetic energy of about 5.3 MeV.
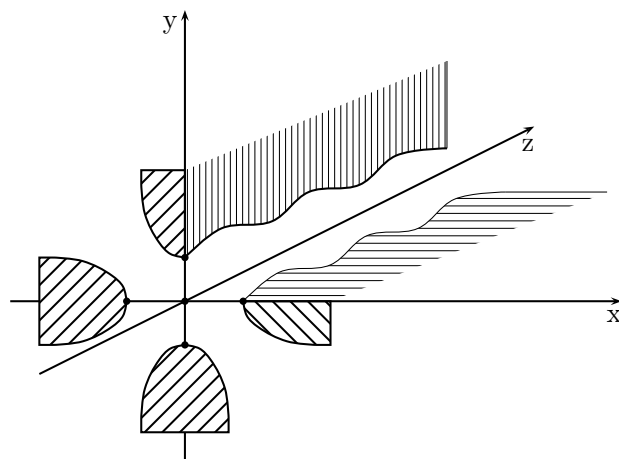
(a)
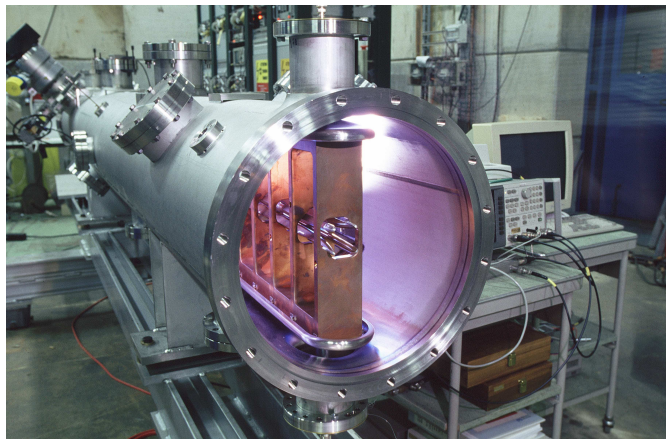
(b)

Figure B.7: *(a) Schematic view of the four RFQ electrodes. The modulation along their lengths that ensures efficient deceleration is illustrated.(Picture adapted from [98]) (b) The radio frequency quadrupole (RFQ) used for the ASACUSA experiments. The ladder structure supporting the 4 electrodes as well as the RF cells can be seen nicely. (Picture taken from [99])*

Appendix C

S-Parameters

When measuring electromagnetic properties of microwave elements and networks, it is common practice to apply the concept of waves instead of currents and voltages used at Dc or low frequency[1]. To describe a network within this approach, a reference plane must be defined (in case of the cavity, the reference plane is defined by the feedthroughs of the cavity input) to define the phase. The incoming and outgoing waves with respect to this plane can then be considered (Fig. C.1). The incoming wave a_1 is de-
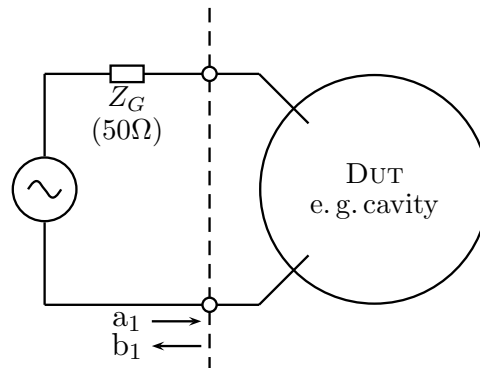
Figure C.1: *Example for a one port network consisting of a generator and a device under test (DUT). The reference plane (dashed line), the wave traveling towards the reference plane a_1 and the wave traveling away from it b_1 are indicated.*

scribed as the ratio of the incident voltage U_{inc} over the square-root of a reference impedance (Z_0) whereas the outgoing wave b_1 is the ratio of the reflected voltage wave U_{refl} with respect to the square-root of the reference

---

[1] The quasi static approach is no longer valid if the linear dimensions of the device under test (DUT) exceed $\lambda/10$. Thus, this criterion marks the transition between the two concepts.

impedance[2]:

$$a_1 = \frac{U_{\mathrm{inc}}}{\sqrt{Z_0}} \qquad \text{and} \qquad b_1 = \frac{U_{\mathrm{refl}}}{\sqrt{Z_0}} \tag{C.1}$$

This approach allows the definition of the S-parameters [102]. For the considered case of a one port, only S_{11} is defined as the ratio between the reflected over the incident wave:

$$S_{11} = \frac{b_1}{a_1} \tag{C.2}$$

In this case, S_{11} is equal to the reflection coefficient Γ.

For a higher number of ports, further S-parameters can be defined, since for each port n (where n is the number of ports) incoming and outgoing waves can be defined. Thus for an n-port, the S-parameters would be defined as:

$$b_1 = S_{11}a_1 + S_{12}a_2 + \cdots + S_{1n}a_n$$
$$b_2 = S_{21}a_1 + S_{22}a_2 + \cdots + S_{2n}a_n$$
$$\vdots \qquad\qquad\qquad\qquad \vdots$$
$$b_n = S_{n1}a_1 + S_{n2}a_2 + \cdots + S_{nn}a_n$$

---

[2]This notation is the European definition. In the 'US' definition, effective values are used and hence they differ by a factor two. For the concept of the S-parameters, this is not important, since only ratios of waves are considered.

Appendix D

Shielding Simulation Results

D.1 Cusp Trap

In the context of this thesis a shielding for the cusp trap has been designed. Its purpose is to reduce the stray field from the trap magnet at the location of the cavity. This field was determined to be roughly $30\,\mathrm{G}$ at the center of the cavity.

The requirements for the shielding are adverse: It should provide a considerable shielding effect on the cavity side while not disturbing the cusp field in the trap center too much. Different shielding geometries have been considered to fulfill these conditions (all shielding layers are located at the cusp trap end close to the cavity unless stated otherwise):

- a full shielding (Fig. D.1 (a))

- a full shielding at both ends of the cusp trap (Fig. D.1 (b))

- a quadratic shielding (Fig. D.1 (c))

- a quadratic shielding extended to the side (Fig. D.1 (d))

- a circular shielding (Fig. D.1 (e))

- a circular shielding with an additional cylinder in the center (Fig. D.1 (f))

- a circular shielding with an additional cone at in the center (Fig. D.2)

All of them were investigated by simulation studies. The cusp trap was simulated using four coils powered by opposite currents to model a $3\,\mathrm{T}$ cusp field. Each shielding was made of soft iron, since its effect on the field lines of the cusp trap are considerably smaller than for mu-metal which is usually used as a shielding material. The lower effect is due to the lower magnetic permeability μ of soft iron, which is between two and three whereas for mu-metal the magnetic permeability starts at 50000.

(a)   (b)

(c)   (d)

(e)   (f)
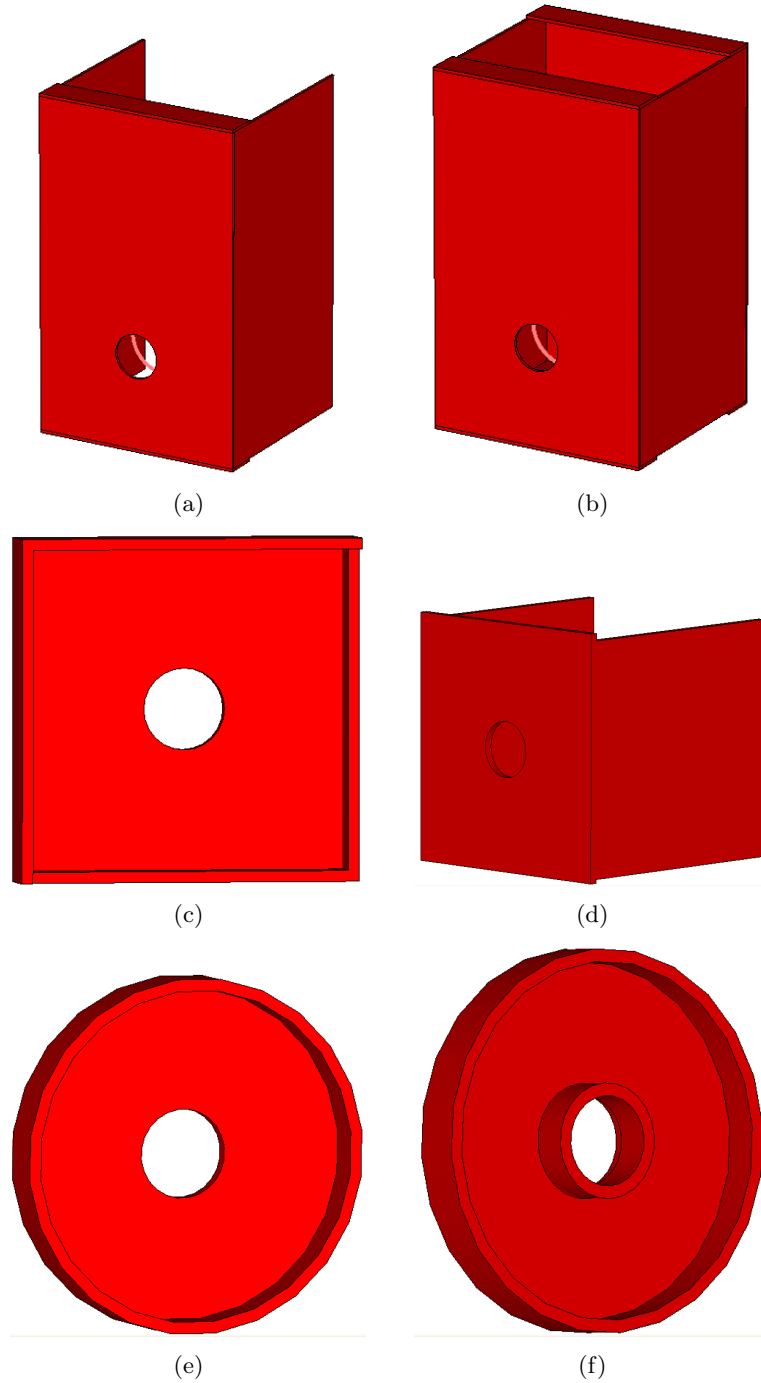
Figure D.1: *(Color) The different shielding types for the cusp trap as used for simulation studies.*
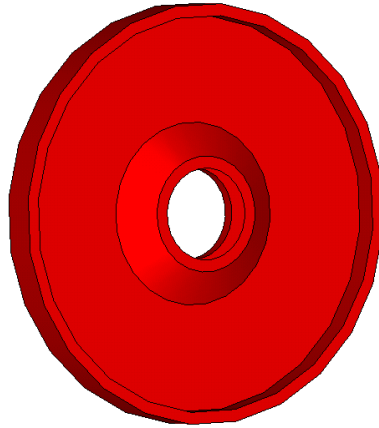
Figure D.2: *(Color) The shielding geometry chosen as final design. It proved to have the best shielding effect on the side of the cusp trap closer to the cavity.*
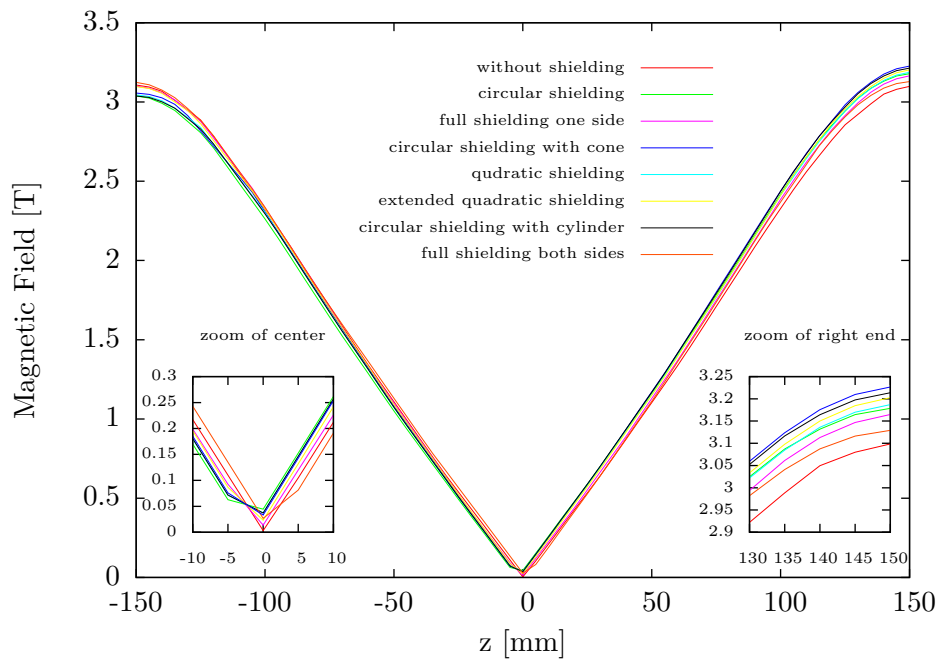
Figure D.3: *(Color) Simulation results of the field (absolute value) in the cusp trap center for the considered geometries. It can be seen that each shielding has no large effect on the field in the cusp trap center. The circular shield with the additional cone in the center provides the best shielding of the field on the trap exit. Consequently, it was chosen as the final design. Note that an increase of the field in the presence of the shielding is due to the distortion of the field lines caused by the shielding material. The bigger the distortion, the more the field lines are bent and hence the more effective is the shielding.*

The simulation results for the considered geometries are summarized in
Fig. D.3. As can be seen, the effect of all considered shielding layers on
the magnetic field in the trap center is quite small. The circular shielding
with the additional nose cone proved to have the best shielding effect on the
cavity side. Consequently, it was chosen for mechanical implementation.

D.2   Static Magnetic Field

The simulation results for the static field generated by round and rectangular
coils are summarized in Table D.1.

Table D.1: *Field homogeneity as a function of distance for a double round and
a double rectangular coil pair. The minimum for each case is highlighted.*

		Inhomogeneity [%]	
d_Y	d_Z	round	rectangular
200	90	7.2	4.6
	100	3.1	2.1
	110	5.6	3.8
	120	4.8	3.3
	130	1.7	3.0
	140	3.2	3.4
	150	2.5	1.2
	160	2.1	1.8
	170	1.7	3.0
	180	1.2	0.7
	190	1.2	1.5
	200	1.6	1.5
205	90	7.2	5.1
	100	2.6	3.7
	110	5.6	3.7
	120	4.8	1.7
	130	4.0	2.9
	140	3.2	3.3
	150	2.4	2.2
	160	2.0	2.0
	170	0.5	1.7
	180	1.1	1.4
	190	1.1	1.1
	200	1.6	1.8
210	90	7.2	8.1
	100	6.4	3.7
	110	5.6	3.9

Continued on next page

Table D.1 – continued from previous page

d_Y	d_Z	round	rectangular
		Inhomogeneity [%]	
	120	4.8	3.3
	130	3.9	3.1
	140	3.1	1.3
	150	2.4	2.8
	160	1.9	2.3
	170	1.5	1.6
	180	1.0	1.3
	190	1.1	1.2
	200	1.6	0.7
215	90	6.9	5.1
	100	6.4	4.5
	110	5.6	5.1
	120	2.0	3.5
	130	4.0	3.1
	140	3.1	2.2
	150	2.3	2.8
	160	1.8	3.2
	170	1.4	1.4
	180	0.9	1.3
	190	1.2	0.9
	200	1.6	0.4
220	90	7.2	4.5
	100	6.4	4.5
	110	5.6	5.1
	120	2.0	5.5
	130	3.9	4.0
	140	2.8	2.6
	150	2.3	2.8
	160	1.7	2.3
	170	1.3	1.5
	180	0.8	1.1
	190	1.2	0.9
	200	1.6	0.6
225	90	7.2	4.5
	100	1.2	4.5
	110	5.6	3.6
	120	4.8	3.5
	130	3.9	2.8
	140	0.6	2.4
	150	2.3	2.1

Table D.1 – continued from previous page

		Inhomogeneity [%]	
d_Y	d_Z	round	rectangular
	160	1.6	1.5
	170	1.2	1.3
	180	0.7	1.1
	190	1.2	0.7
	200	1.6	0.5
230	90	7.2	4.5
	100	6.4	5.7
	110	5.0	4.3
	120	4.8	3.2
	130	3.9	2.8
	140	3.1	2.6
	150	2.5	2.1
	160	1.5	1.7
	170	1.1	1.3
	180	0.6	1.0
	190	1.2	0.7
	200	1.7	0.5
235	90	3.5	2.4
	100	6.4	6.8
	110	5.6	4.0
	120	1.0	3.5
	130	3.9	1.5
	140	3.1	2.3
	150	2.3	2.1
	160	1.5	1.6
	170	1.0	1.5
	180	0.7	1.0
	190	1.2	0.6
	200	1.7	0.4
240	90	7.3	4.4
	100	6.4	4.0
	110	5.6	3.6
	120	4.8	3.2
	130	3.9	2.7
	140	3.1	2.6
	150	2.2	1.0
	160	1.3	1.7
	170	*0.3*	1.2
	180	0.7	0.4
	190	1.2	0.6

Table D.1 – continued from previous page

Inhomogeneity [%]

d_Y	d_Z	round	rectangular
	200	1.7	*0.1*
245	90	7.3	6.6
	100	6.5	2.2
	110	5.6	3.6
	120	4.8	5.3
	130	3.9	2.7
	140	3.1	2.3
	150	2.2	1.8
	160	1.4	1.5
	170	0.8	1.0
	180	0.7	0.8
	190	1.2	1.1
	200	1.7	0.4

The field homogeneity of the static field for round double and single coil pairs including different shielding geometries are summarized in Table D.2.

Table D.2: *Simulation results for round double Helmholtz coils including either one or three layers of shielding. Various shielding geometries have been considered for each case: Three different cubic shielding with side lengths 55 cm, 63 cm and 66 cm and one cuboid shielding with 55 × 63 cm.*

Inhomogeneity [%]

		one layer				three layers			
d_Y	d_Z	55 cm	55 × 63 cm	63 cm	66 cm	55 cm	55 × 63 cm	63 cm	66 cm
200	90	1.91	2.07	8.08	8.52	1.82	1.96	7.84	8.31
	100	1.71	1.85	7.20	7.59	1.62	1.75	6.95	7.39
	110	1.50	1.63	6.29	6.64	1.42	1.53	6.06	6.45
	120	1.28	1.40	5.35	5.66	1.20	1.30	5.15	5.49
	130	1.05	1.17	4.49	4.75	0.98	1.08	4.30	4.61
	140	0.83	0.96	3.83	4.06	0.75	0.87	3.64	3.93
	150	0.61	0.75	3.15	3.36	0.53	0.66	2.96	3.23
	160	0.42	0.54	2.46	2.67	0.34	0.45	2.29	2.52
	170	0.25	0.34	1.77	1.96	0.18	0.26	1.60	1.83
	180	0.13	0.18	1.46	1.59	0.11	0.11	1.37	1.51
	190	0.22	0.18	1.71	1.85	0.30	0.25	1.63	1.77
	200	0.40	0.37	2.06	2.18	0.47	0.45	1.97	2.11

Table D.2 – continued from previous page
Inhomogeneity [%]

d_Y	d_Z	one layer				three layers			
		55 cm	55 × 63 cm	63 cm	66 cm	55 cm	55 × 63 cm	63 cm	66 cm
205	90	1.89	2.03	7.98	8.41	1.80	1.92	7.71	8.18
	100	1.68	1.82	7.09	7.47	1.60	1.71	6.84	7.26
	110	1.47	1.60	6.16	6.51	1.39	1.50	5.94	6.32
	120	1.26	1.37	5.24	5.54	1.18	1.27	5.02	5.35
	130	1.03	1.14	4.32	4.59	0.94	1.04	4.14	4.44
	140	0.81	0.92	3.67	3.91	0.72	0.83	3.49	3.76
	150	0.59	0.71	3.00	3.21	0.51	0.63	2.81	3.05
	160	0.39	0.50	2.31	2.51	0.31	0.42	2.13	2.37
	170	0.21	0.30	1.62	1.79	0.13	0.22	1.44	1.65
	180	0.08	0.13	1.36	1.48	0.15	0.11	1.25	1.40
	190	0.24	0.21	1.58	1.69	0.32	0.29	1.49	1.62
	200	0.43	0.40	1.91	2.04	0.50	0.49	1.85	1.96
210	90	1.86	2.00	7.86	8.30	1.77	1.88	7.60	8.08
	100	1.66	1.78	6.97	7.36	1.57	1.67	6.72	7.15
	110	1.46	1.57	6.04	6.40	1.37	1.45	5.81	6.20
	120	1.23	1.33	5.11	5.42	1.14	1.23	4.89	5.23
	130	1.01	1.10	4.17	4.44	0.92	1.00	3.98	4.29
	140	0.78	0.88	3.51	3.75	0.69	0.79	3.31	3.58
	150	0.56	0.68	2.85	3.06	0.48	0.58	2.64	2.90
	160	0.36	0.47	2.14	2.33	0.27	0.37	1.96	2.20
	170	0.17	0.26	1.47	1.64	0.09	0.18	1.30	1.49
	180	0.08	0.10	1.26	1.38	0.17	0.12	1.14	1.29
	190	0.27	0.24	1.43	1.55	0.36	0.32	1.34	1.46
	200	0.45	0.44	1.85	1.90	0.52	0.52	1.89	1.93
215	90	1.84	1.96	7.76	8.19	1.74	1.84	7.50	7.96
	100	1.64	1.75	6.86	7.24	1.55	1.64	6.61	7.03
	110	1.43	1.54	5.94	6.28	1.34	1.43	5.69	6.08
	120	1.21	1.30	4.99	5.29	1.12	1.19	4.77	5.11
	130	0.99	1.07	4.05	4.30	0.89	0.97	3.84	4.13
	140	0.76	0.84	3.36	3.59	0.67	0.75	3.15	3.43
	150	0.54	0.63	2.69	2.88	0.45	0.54	2.49	2.73
	160	0.33	0.42	1.99	2.18	0.25	0.33	1.81	2.06
	170	0.15	0.23	1.39	1.61	*0.08*	0.13	1.31	1.55
	180	0.11	0.10	1.15	1.26	0.22	0.16	1.04	1.18
	190	0.29	0.28	1.30	1.39	0.39	0.37	1.29	1.32
	200	0.48	0.47	1.90	1.96	0.56	0.56	1.96	1.99
220	90	1.82	1.93	7.66	8.08	1.72	1.81	7.39	7.86
	100	1.62	1.72	6.74	7.13	1.52	1.60	6.49	6.91

Table D.2 – continued from previous page

Inhomogeneity [%]

d_Y	d_Z	one layer				three layers			
		55 cm	55 × 63 cm	63 cm	66 cm	55 cm	55 × 63 cm	63 cm	66 cm
	110	1.40	1.50	5.82	6.16	1.31	1.38	5.57	5.96
	120	1.18	1.28	4.87	5.17	1.09	1.15	4.65	4.98
	130	0.96	1.04	3.94	4.18	0.87	0.93	3.72	4.01
	140	0.74	0.81	3.21	3.42	0.65	0.71	3.01	3.28
	150	0.51	0.60	2.53	2.72	0.43	0.50	2.35	2.58
	160	0.30	0.39	1.90	2.15	0.22	0.29	1.80	2.07
	170	0.11	0.19	1.39	1.59	0.10	0.09	1.30	1.56
	180	0.15	0.11	1.05	1.16	0.25	0.20	0.93	1.08
	190	0.32	0.31	1.29	1.32	0.42	0.40	1.33	1.35
	200	0.50	0.50	1.93	2.00	0.59	0.59	2.00	2.04
225	90	1.80	1.90	7.55	7.98	1.70	1.78	7.28	7.75
	100	1.60	1.68	6.64	7.03	1.50	1.57	6.39	6.81
	110	1.38	1.46	5.71	6.05	1.29	1.33	5.46	5.85
	120	1.16	1.24	4.76	5.06	1.07	1.13	4.54	4.87
	130	0.94	1.00	3.80	4.06	0.85	0.90	3.58	3.88
	140	0.72	0.77	3.05	3.28	0.62	0.66	2.85	3.11
	150	0.49	0.56	2.39	2.67	0.40	0.46	2.30	2.56
	160	0.28	0.35	1.90	2.14	0.17	0.25	1.80	2.07
	170	0.09	0.15	1.38	1.62	0.14	*0.07*	1.29	1.53
	180	0.19	0.14	0.94	1.11	0.29	0.24	*0.85*	1.03
	190	0.35	0.35	1.33	1.38	0.45	0.44	1.43	1.42
	200	0.53	0.54	2.00	2.07	0.62	0.63	2.10	2.11
230	90	1.77	1.87	7.46	7.89	1.67	1.74	7.20	7.65
	100	1.57	1.65	6.55	6.94	1.48	1.53	6.31	6.70
	110	1.36	1.44	5.61	5.95	1.26	1.31	5.39	5.74
	120	1.14	1.21	4.66	4.96	1.05	1.08	4.47	4.76
	130	0.92	0.98	3.70	3.95	0.82	0.86	3.54	3.79
	140	0.68	0.75	2.91	3.14	0.60	0.63	2.78	3.00
	150	0.47	0.53	2.39	2.63	0.37	0.41	2.29	2.57
	160	0.25	0.32	1.89	2.15	0.16	0.21	1.79	2.06
	170	0.08	0.12	1.39	1.63	0.18	0.11	1.29	1.56
	180	0.22	0.17	*0.89*	*1.11*	0.32	0.28	0.86	*1.02*
	190	0.39	0.37	1.44	1.45	0.49	0.48	1.58	1.54
	200	0.56	0.57	2.09	2.13	0.65	0.67	2.24	2.22
235	90	1.76	1.83	7.39	7.80	1.65	1.71	7.17	7.61
	100	1.55	1.62	6.49	6.85	1.45	1.50	6.28	6.67
	110	1.34	1.40	5.56	5.87	1.23	1.28	5.36	5.70
	120	1.12	1.18	4.61	4.88	1.01	1.05	4.43	4.73

Table D.2 – **continued from previous page**

Inhomogeneity [%]

d_Y	d_Z	one layer				three layers			
		55 cm	55 × 63 cm	63 cm	66 cm	55 cm	55 × 63 cm	63 cm	66 cm
	130	0.90	0.94	3.66	3.88	0.79	0.83	3.53	3.82
	140	0.68	0.71	2.87	3.16	0.57	0.60	2.81	3.08
	150	0.45	0.49	2.38	2.65	0.34	0.37	2.28	2.57
	160	0.22	0.28	1.88	2.12	0.14	0.17	1.77	2.07
	170	0.11	0.08	1.38	1.62	0.23	0.15	1.28	1.55
	180	0.26	*0.21*	0.87	1.12	0.37	0.32	1.02	1.08
	190	0.42	0.41	1.58	1.60	0.52	0.51	1.73	1.70
	200	0.58	0.61	2.26	2.30	0.69	0.70	2.41	2.40
240	90	1.73	1.80	7.36	7.78	1.61	1.67	7.15	7.59
	100	1.53	1.59	6.46	6.82	1.42	1.46	6.26	6.64
	110	1.32	1.38	5.53	5.84	1.21	1.24	5.33	5.68
	120	1.10	1.14	4.58	4.85	0.99	1.02	4.39	4.69
	130	0.88	0.91	3.69	3.99	0.77	0.78	3.64	3.91
	140	0.66	0.68	2.94	3.20	0.54	0.56	2.91	3.15
	150	0.43	0.46	2.37	2.66	0.32	0.33	2.28	2.58
	160	0.21	0.25	1.87	2.14	0.16	0.13	1.77	2.02
	170	*0.15*	0.07	1.37	1.62	0.28	0.18	1.28	1.55
	180	0.29	0.25	1.00	1.16	0.42	0.35	1.17	1.23
	190	0.44	0.44	1.71	1.75	0.55	0.55	1.89	1.86
	200	0.61	0.64	2.41	2.45	0.72	0.75	2.55	2.55
240	90	1.71	1.77	7.33	7.75	1.59	1.63	7.11	7.55
	100	1.51	1.56	6.43	6.79	1.40	1.43	6.23	6.61
	110	1.30	1.34	5.49	5.82	1.19	1.21	5.30	5.65
	120	1.08	1.11	4.56	4.88	0.97	0.99	4.49	4.79
	130	0.86	0.88	3.79	4.07	0.75	0.76	3.75	4.04
	140	0.63	0.65	3.03	3.29	0.52	0.53	3.01	3.18
	150	0.41	0.42	2.37	2.59	0.30	0.30	2.28	2.53
	160	0.19	0.21	1.87	2.09	0.19	0.11	1.76	2.07
	170	0.19	0.11	1.36	1.60	0.33	0.23	1.27	1.53
	180	0.32	0.28	1.14	1.31	0.46	0.39	1.29	1.39
	190	0.48	0.47	1.86	1.89	0.59	0.58	2.03	2.01
	200	0.65	0.67	2.55	2.60	0.76	0.77	2.70	2.70

Bibliography

[1] R. W. Wilson. *The Cosmic Microwave Background Radiation.* Nobel Foundation − (1978) −. Nobel Lecture.

[2] R. Cahn and G. Goldhaber. *The experimental foundations of particle physics.* Cambridge University Press (2009). ISBN 9780521521475.

[3] W. K. Röntgen. *Eine Neue Art von Strahlen.* Aus den 'Sitzungsberichten der Würzburger physikalisch-medicinischen Gesellschaft' − (1895) −.

[4] J. J. Thomson. *Cathode Rays.* The Electrician **39** (1897) 104.

[5] W. Prout. *On the Relation between the Specific Gravities of Bodies in their Gaseous State and the Weights of their Atoms.* Annals of Philosophy **6** (1825) 321 − 330.

[6] W. Prout. *Correction of a Mistake in the Essay on the Relation between the Specific Gravities of Bodies in theirGaseous State and the Weights of their Atoms.* Annals of Philosophy **7** (1816) 111 − 113.

[7] H. Geiger and E. Marsden. *On a Diffuse Reflection of the α-Particles.* Proceedings of the Royal Society, Series A **82** (1909) 495 − 500.

[8] E. Rutherford. *The Scattering of α and β Particles by Matter and the Structure of the Atom.* Philosophical Magazine **21** (1911) 669 − 688.

[9] N. Bohr. *On the Constitution of Atoms and Molecules.* Philosophical Magazine **26** (1913) 1 − 24.

[10] P. A. M. Dirac. *The Quantum Theory of the Electron.* Proceedings of the Royal Society of London. Series A **117** (1928) 610 − 624.

[11] P. A. M. Dirac. *The Quantum Theory of the Electron. Part II.* Proceedings of the Royal Society of London. Series A **118** (1928) 351 − 361.

[12] C. D. Anderson. *The Positive Electron.* Physical Review **43** (1933) 491 − 494.

[13] O. Chamberlain et al. *Observation of Antiprotons*. Physical Review **100** (1955) 947 − 950.

[14] G. Baur et al. *Production of antihydrogen*. Physics Letters B **368** (1996) 251 − 258.

[15] M. Amoretti et al. *Production and detection of cold antihydrogen atoms*. Nature **419** (2002) 456 − 459.

[16] G. Gabrielse et al. *Driven Production of Cold Antihydrogen and the First Measured Distribution of Antihydrogen States*. Physical Review Letters **89** (2002) 233401.

[17] G. Gabrielse et al. *Background-Free Observation of Cold Antihydrogen with Field-Ionization Analysis of Its States*. Physical Review Letters **89** (2002) 213401.

[18] G. B. Andresen et al. *Trapped antihydrogen*. Nature **468** (2010) 673–676.

[19] Y. Enomoto et al. *Synthesis of Cold Antihydrogen in a Cusp Trap*. Physical Review Letters **105** (2010) 243401.

[20] R. G. Sachs. *The Physics of Time Reversal*. University of Chicago Press (1987).

[21] T. D. Lee and C. N. Yang. *Question of Parity Conservation in Weak Interactions*. Physical Review **104** (1956) 254 − 258.

[22] C. S. Wu et al. *Experimental Test of Parity Conservation in Beta Decay*. Physical Review **105** (1957) 1413 − 1415.

[23] J. H. Christenson et al. *Evidence for the 2π Decay of the K_2^0 Meson*. Physical Review Letters **13** (1964) 138 − 140.

[24] V. L. Fitch. *The Discovery of Charge-conjugation Parity Asymmetry*. Nobel Foundation − (1980) −. Nobel lecture.

[25] J. W. Cronin. *CP Symmetry Violation — the Search for its Origin*. Nobel Foundation − (1980) −. Nobel lecture.

[26] A. D. Sakharov. *Violation of CP Invariance, C Asymmetry, and Baryon Asymmetry of the Universe*. Pis'ma v Zhurnal eksperimentalnoi i teoreticheskoi fiziki **5** (1967) 32 − 35.

[27] A. D. Dolgov. *Baryogenesis and Cosmological Antimatter*. AIP Conference Proceedings **1116** (2009) 155 − 170.

[28] C. Bambi and A. Dolgov. *Antimatter in the Milky Way*. Nuclear Physics B **784** (2007) 132 − 150.

[29] O. Bertolami et al. *CPT violation and baryogenesis.* Physics Letters B **395** (1997) 178 – 183.

[30] G. Barenboim and N. E. Mavromatos. *Decoherent neutrino mixing, dark energy, and matter-antimatter asymmetry.* Physical Review D **70** (2004) 093015.

[31] D. Colladay and V. A. Kostelecký. CPT *violation and the standard model.* Physical Review D **55** (1997) 6760 – 6774.

[32] R. Bluhm, V. A. Kostelecký, and N. Russell. *CPT and Lorentz Tests in Hydrogen and Antihydrogen.* Physical Review Letters **82** (1999) 2254 – 2257.

[33] R. Bluhm, V. A. Kostelecký, and N. Russell. *Hydrogen and antihydrogen spectroscopy for studies of CPT and Lorentz symmetry.* AIP Conference Proceedings **457** (1999) 70 – 79.

[34] H. M. Goldenberg, D. Kleppner, and N. F. Ramsey. *Atomic Hydrogen Maser.* Physical Review Letters **5** (1960) 361 – 362.

[35] N. F. Ramsey. *Experiments with trapped hydrogen atoms and neutrons.* Physica Scripta **1995** (1995) 323.

[36] E. Abouzaid et al. *Precise measurements of direct CP violation, CPT symmetry, and other parameters in the neutral kaon system.* Physical Review D **83** (2011) 092001.

[37] T. Komatsubara. *Experiments with -meson decays.* Progress in Particle and Nuclear Physics **-** (2012) –.

[38] B. Juhász et al. *Measurement of the ground-state hyperfine structure of antihydrogen.* AIP Conference Proceedings **796** (2005) 243 – 246.

[39] B. Juhász. *Measurement of the ground-state hyperfine splitting of antihydrogen.* talk LEAP 08 (2008).

[40] C. G. Parthey et al. *Improved Measurement of the Hydrogen $1S - 2S$ Transition Frequency.* Physical Review Letters **107** (2011) 203001.

[41] B. Juhász and E. Widmann. *Proposed measurement of the ground-state hyperfine structure of antihydrogen.* Hyperfine Interactions **172** (2006) 107 – 110.

[42] I. I. Rabi et al. *A New Method of Measuring Nuclear Magnetic Moment.* Physical Review **53** (1938) 318 – 318.

[43] I. I. Rabi et al. *The Molecular Beam Resonance Method for Measuring Nuclear Magnetic Moments. The Magnetic Moments of $_3\mathrm{Li}^6$, $_3\mathrm{Li}^7$ and $_9\mathrm{F}^{19}$.* Physical Review **55** (1939) 526 – 535.

[44] W. Gerlach and O. Stern. *Der experimentelle Nachweis der Richtungsquantelung im Magnetfeld.* Zeitschrift für Physik A Hadrons and Nuclei **9** (1922) 349 – 352.

[45] N. F. Ramsey. *Experiments with separated oscillatory fields and hydrogen masers.* Reviews of Modern Physics **62** (1990) 541 – 552.

[46] *Encyclopedia of Physics Atoms III – Molecules I*, volume XXXVII/1. Springer-Verlag Berlin Göttingen Heidelberg (1959).

[47] Y. Enomoto. *Antihydrogen production in cusp trap.* Ph.D. thesis, RIKEN Advanced Science Institute, Hirosawa, Wako, Saitama 351-0198, Japan (2011).

[48] N. Kuroda et al. *Confinement of a Large Number of Antiprotons and Production of an Ultraslow Antiproton Beam.* Physical Review Letters **94** (2005) 023401.

[49] N. Kuroda et al. *Radial Compression of an Antiproton Cloud for Production of Intense Antiproton Beams.* Physical Review Letters **100** (2008) 203402.

[50] H. Imao et al. *ASACUSA MUSASHI: New progress with intense ultra slow antiproton beam.* Hyperfine Interactions **194** (2009) 71 – 76.

[51] H. Imao et al. *Positron accumulation and manipulation for antihydrogen synthesis.* Journal of Physics: Conference Series **225** (2010) 012018.

[52] H. Saitoh et al. *Radial compression of a non-neutral plasma in a cusp trap for antihydrogen synthesis.* Physical Review A **77** (2008) 051403.

[53] A. Mohri and Y. Yamazaki. *A possible new scheme to synthesize antihydrogen and to prepare a polarised antihydrogen beam.* Europhys. Lett. **63** (2003) 207 – 213.

[54] F. Robicheaux. *Atomic processes in antihydrogen experiments: a theoretical and computational perspective.* Journal of Physics B: Atomic, Molecular and Optical Physics **41** (2008) 192001.

[55] G. Gabrielse. *Atoms made entirely of antimatter: Two methods produce slow antihydrogen.* Advances In Atomic, Molecular, and Optical Physics **50** (2005) 155 – 217.

[56] A. Müller and A. Wolf. *Production of antihydrogen by recombination of $\bar{p}$ with e^+: What can we learn from electron–ion collision studies?* Hyperfine Interactions **109** (1997) 233 – 267.

[57] J. L. Wiza. *Microchannel plate detectors.* Nuclear Instruments and Methods **162** (1979) 587 – 601.

[58] E. Segre. *Antinucleons.* Annual Review of Nuclear Science **8** (1958) 127 – 162.

[59] B. Juhasz. *private communication.*

[60] F. Bloch and A. Siegert. *Magnetic Resonance for Nonrotating Fields.* Phys. Rev. **57** (1940) 522 – 527.

[61] T. Kroyer. *Design of a spin-flip cavity for the measurement of the antihydrogen hyperfine structure.* Technical Report CERN-AB-Note-2008-016, CERN, Geneva (2008).

[62] P.-S. Kildal. *Artificially soft and hard surfaces in electromagnetics.* Antennas and Propagation, IEEE Transactions on **38** (1990) 1537 – 1544.

[63] E. Yablonovitch. *Photonic band-gap structures.* Journal of the Optical Society of America B **10** (1993) 283 – 295.

[64] F. Caspers. *More Compact Cavities, Double Ridge Structures.* CARE-HHH Mini workshop - LHC Crab Cavity Validation (2008).

[65] J. R. Delayen and H. Wang. *New compact TEM-type deflecting and crabbing rf structure.* Physical Review Special Topics - Accelerators and Beams **12** (2009) 062002.

[66] G. Montenero. *private communication.*

[67] URL `http://www.feuerherdt.de/`.

[68] S. Calatroni et al. *Design Aspects of the RF Contacts for the LHC Beam Vacuum Interconnects.* $- -$ (2001) 4 p.

[69] *Elektromagnetische Verträglichkeit.* B. G. Teubner Stuttgart (1992).

[70] URL `http://pmb-alcen.com/en`.

[71] URL `http://www.pulsarmicrowave.com/`.

[72] E. Majorana. *Atomi orientati in campo magnetico variabile.* Nuovo Cimento **9** (1932) 43.

[73] B. Juhász, E. Widmann, and S. Federmann. *Measurement of the ground-state hyperfine splitting of antihydrogen.* Journal of Physics: Conference Series **335** (2011) 012059.

[74] B. Juhász. *Radiofrequency cavity for the measurement of the ground-state hyperfine splitting of antihydrogen - Version 1.0.* Technical report, CERN (2009).

[75] W. Franzen. *Generation of Uniform Magnetic Fields by Means of Air-Core Coils.* Review of Scientific Instruments **33** (1962) 933 – 938.

[76] F. Caspers. *private communication.*

[77] URL `www.magneticshields.co.uk`.

[78] URL `http://www.ohtama.co.jp/english/`.

[79] J. R. Taylor. *An Introduction to Error Analysis — the Study of Uncertainties in Physical Measurements.* University Science Books, second edition edition (1997).

[80] *LHC Design Report.* URL `http://lhc.web.cern.ch/lhc/LHC-DesignReport.html`.

[81] URL `http://cdsweb.cern.ch/record/615875`.

[82] D. Möhl. *Production of Low-Energy Antiprotons.* International Workshop on Antimatter Gravity and Antihydrogen Spectroscopy − (1996) −.

[83] B. Autin et al. *The antiproton decelerator (AD), a simplified antiproton source (feasibility study). oai:cds.cern.ch:293071.* Technical Report CERN-PS-95-36 AR, CERN, Geneva (1995).

[84] T. Eriksson. *AD: low-energy antiproton production at CERN.* Hyperfine Interactions **194** (2009) 123 – 128.

[85] URL `http://cdsweb.cern.ch/record/39385`.

[86] S. van der Meer. *Stochastic cooling and the accumulation of antiprotons.* Reviews of Modern Physics **57** (1985) 689 – 697.

[87] D. Möhl et al. *Physics and technique of stochastic cooling.* Physics Reports **58** (1980) 73 – 102.

[88] J. Eades and F. J. Hartmann. *Forty years of antiprotons.* Reviews of Modern Physics **71** (1999) 373 – 419.

[89] J. Marriner and D. McGinnis. *An introduction to stochastic cooling.* AIP Conference Proceedings **249** (1992) 693 – 761.

[90] F. Caspers and D. Möhl. *History of stochastic beam cooling and its application in many different projects.* European Physical Jounal − (2012) −. To be published.

[91] M. D. Church and J. P. Marriner. *The Antiproton Sources: Design and Operation.* Annual Review of Nuclear and Particle Science **43** (1993) 253 – 295.

[92] URL `http://public.web.cern.ch/public/en/research/ACE-en.html`.

[93] URL `http://enlight.web.cern.ch/enlight/cms/?file=home`.

[94] *The AEgIS collaboration.* http://aegis.web.cern.ch/aegis/home.html. URL `http://aegis.web.cern.ch/aegis/home.html`.

[95] J. Hengst et al. *The ALPHA collaboration.* URL `http://alpha.web.cern.ch/alpha/`.

[96] G. Gabrielse et al. *ATRAP collaboration.* URL `http://hussle.harvard.edu/~gabrielse/gabrielse/overviews/Antihydrogen/Antihydrogen.html`.

[97] ASACUSA collaboration. *Atomic Spectroscopy And Collisions Using Slow Antiprotons (ASACUSA).* Proposal CERN-SPSC-2010-005 ; SPSC-SR-056, CERN, Geneva, Switzerland (2010).

[98] J. Bosser et al. *Feasibility study of a decelerating radio frequency quadrupole system for the antiproton decelerator AD. oai:cds.cern.ch:558230.* Technical Report CERN-OPEN-2002-040. CERN-PS-HP-NOTE-97-36, CERN, Geneva (1998).

[99] URL `http://cdsweb.cern.ch/record/40852`.

[100] P. A. Posocco et al. *ASACUSA Beam Line Commissioning.* CERN ATS Note 2011-007 MD − (2010) −.

[101] Y. Bylinsky, A. M. Lombardi, and W. Pirkl. *RFQD: a decelerating radio frequency quadrupole for the CERN antiproton facility. oai:cds.cern.ch:455803.* 20th International Linear Accelerator Conference − (2000) 4 p.

[102] K. Kurokawa. *Power Waves and the Scattering Matrix.* Microwave Theory and Techniques, IEEE Transactions on **13** (1965) 194 – 202.

Acknowledgements

When starting this project I had no clue that I would be granted the chance to work with so many brilliant people. Not only did I broaden my professional horizon by participating in many discussion where all my questions (be it bright or not so bright ones) were answered benevolently and patiently, but I also developed as a person. I indeed lack the words to describe how much I gained by working in such a nourishing environment as CERN is. Along my journey, I met several people that I am greatly indebted to, so I would like to seize my chance when writing this thesis to say 'Thank you' to all of them.

First of all, I have to thank my supervisor Fritz Caspers for his constant support, his patience and his way of always having a helping hand when needed and knowing when to extend it. I cannot say in how many ways, be it personal or professional, he has helped me to become the person I am today — Vielen Dank Fritz! And if I am now not 'zu blöd einen Pudding an die Wand zu nageln', then he has to be credited for it.

My thanks also go to my university supervisor Eberhard Widmann. He taught me much about the principles of high precision physics and always provided constant support during this project.

I would also like to thank Edgar Mahner for so many questions answered — even the ones I could not think of posing. He was an immense help — not only when thinking about vacuum aspects of the cavity. I am also happy to know that in him I have not only found a terrific colleague but also a great personal friend.

A big 'thank you' is also due for my fellow colleagues Michael Betz and Thomas Kaltenbacher. Talking to people who suffer the same as oneself proved to very beneficial - especially with huge amounts of coffee involved. It would have been -3 dB of fun without you guys!!

A big thank you is also due to my office mate Benoit Salvant, who always had an open ear for my problems with the simulation code — even if his time did actually not allow it.

Thanks also to Bertalan Juhasz, who guided me around many rough edges in the context of the project, as well as Susanne Friedreich and Oswald Massiczek for being terrific colleagues. You guys rock!

Furthermore, I would like to thank Alexandre Sinturel as well as Nico-

las Zelko and his colleagues for their enormous engagement every time we needed to bake our setup and test it for vacuum tightness — even if it was a very short notice call.

I am also deeply indebted to Edmund Ciapala, Erk Jensen and Elena Chapochnikova as well as all my colleagues from BE-RF for their constant support. The very helpful work of Marina Malabaila and her colleagues, Marco Buzio, Giuseppe Montenero, Dominique Bodart, Rui De Oliveira and his team as well as the CERN main and RF workshop is highly appreciated.

This work was carried out in the framework of the Austrian Doctoral Student Program. The support of the Austrian ministry of science is acknowledged.

Finally, for Christopher: 'Ich habe die Farbe des Weizens gewonnen. '[1]

Last but absolutely not least, I would like to thank my family for granting me the greatest gift possible a beloved person can receive: letting me go.

---

[1]Zitat aus: Der kleine Prinz, Antoine de Saint-Exupéry

List of Own Publications

Articles published in the framework of this thesis.

[1] *Demonstration of 10^{-22} W Signal Detection Methods in the Microwave Range at Ambient Temperature.*
F. Caspers, S. Federmann, and D. Seebacher.
CERN BE Note − (2009) −.
URL `http://cdsweb.cern.ch/record/1195741/files/CERN-BE-TE-Note-2009-026-01.pdf`.

[2] *Ringing in the Pulse Response of Long and Wideband Coaxial Transmission Lines due to Group Delay Dispersion.*
G. Kotzian, F. Caspers, S. Federmann, W. Höfle, and R. de Maria.
PAC proceedings − (2009) −.
URL `http://cdsweb.cern.ch/record/1212915/files/th5rfp033.pdf`.

[3] *Design of a 1.42 GHZ spin-flip cavity for antihydrogen atoms.*
S. Federmann, F. Caspers, B. Juhasz, E. Mahner, and E. Widmann.
IPAC proceedings − (2010) −.
URL `http://accelconf.web.cern.ch/AccelConf/IPAC10/papers/MOPE054.pdf`.

[4] *Electron Cloud Measurements of Coated and Uncoated Vacuum Chambers in the CERN SPS by Means of the Microwave Transmission Method.*
S. Federmann, F. Caspers, E. Mahner, P. Costa Pinto, M. Taborelli, B. Salvant, D. Seebacher, and C. Yin Vallgren.
IPAC proceedings − (2010) −.
URL `http://accelconf.web.cern.ch/AccelConf/IPAC10/papers/TUPEA076.pdf`.

[5] *High Temperature Radio Frequency Loads.*
S. Federmann, F. Caspers, A. Grudiev, E. Montesinos, and I. Syratchev.
IPAC proceedings − (2011) −.
URL `http://accelconf.web.cern.ch/AccelConf/IPAC2011/papers/TUPS103.pdf`.

[6] *Measurements of electron cloud density in the CERN Super Proton Synchrotron with the microwave transmission method.*
S. Federmann, F. Caspers, and E. Mahner.
Phys. Rev. ST Accel. Beams **14** (2011) 012802.
URL `http://dx.doi.org/10.1103/PhysRevSTAB.14.012802`.

[7] *Measurement of the ground-state hyperfine splitting of antihydrogen.*
B. Juhász, E. Widmann, and S. Federmann.
Journal of Physics: Conference Series **335** (2011) 012059.
URL `http://dx.doi.org/10.1088/1742-6596/335/1/012059`.

[8] *Frequency Fine-tuning of a Spin-flip Cavity for Antihydrogen Atoms.*
S. Federmann, F. Caspers, E. Mahner, B. Juhasz, and E. Widmann.
IPAC proceedings − (2012) –.
URL `http://accelconf.web.cern.ch/AccelConf/IPAC2012/papers/weppd072.pdf`.

[9] *RF Loads for Energy Recovery.*
S. Federmann, M. Betz, and F. Caspers.
IPAC proceedings − (2012) –.
URL `http://accelconf.web.cern.ch/AccelConf/IPAC2012/papers/thppc023.pdf`.

Silke Federmann

curriculum vitae

Personal details

Date of Birth	12 January 1979
Place of Birth	Mödling, Austria
Sex	Female
Nationality	Austrian

Education

1985 – 1989	**Primary School**, *Volksschule, Enzesfeld-Lindabrunn*, Austria
1989 – 1997	**Secondary School**, *Bundesgymnasium und Bundesrealgymnasium Biondekgasse, Baden*, Austria, Final Examination: Matura
1997 – 2004	**Studies of Chemistry and Psychology/Philosophy/Pedagogics**, *Universität Wien*, Austria
2004 – 2009	**Studies of Physics**, *Universität Wien*, Austria, Degree obtained: Magistra rer. nat.
since 2009	**PhD student of Physics**, *Universität Wien*, Austria, European Nuclear Research Center CERN, Switzerland

Diploma thesis

Title	*Optimization of the Multi Vertex Fitter for CMS Inner Tracker*
Supervisor	Univ. Doz. DI Dr. R. Frühwirth
Key Work	Optimization of a complex algorithm used for parallel vertex reconstruction of events in the CMS detector using data generated by Monte Carlo simulations.

Further education

September 2009	**School**, *CERN Accelerator School — CAS, Accelerator Physics (Intermediate level)*, Darmstadt, Germany
February 2010	**School**, *Joint Universities Accelerator School — JUAS, Radio-Frequency engineering and Vacuum systems*, Archamps, France
June 2010	**School**, *CERN Accelerator School — CAS, RF for Accelerators*, Ebeltoft, Denmark

Experience

July – September 2007	**Internship as a summer student**, *European Nuclear Research Center CERN*, Geneva, Switzerland
October 2009	**Invited Talk**, *Anti e-Cloud Coatings — ACE'09* Diagnostic of coating results — microwave measurements
February 2011	**Teaching Assistant**, *Joint Universities Accelerator School — JUAS, Radio-Frequency engineering*, Archamps, France
March 2011	**Invited Talk**, *CERN-GSI Electron Cloud Workshop* Microwave Diagnostics in the SPS
May 2010	**Poster Presentations**, *International Particle Accelerator Conference*, Kyoto, Japan
May 2012	**Poster Presentations**, *International Particle Accelerator Conference*, New Orleans, USA, Awardee of a Student Grant